THE UNIVERSITY OF CHICAGO

APPLICATIONS OF GOLD NANOPARTICLES TO IMPROVE AND REDESIGN NUCLEIC ACID AMPLIFICATIONS AND NANOMACHINERY

A DISSERTATION SUBMITTED TO
THE FACULTY OF THE DIVISION OF THE PHYSICAL SCIENCES
IN CANDIDACY FOR THE DEGREE OF
DOCTOR OF PHILOSOPHY

DEPARTMENT OF CHEMISTRY

BY
TIMOTHY MICHAEL CRONIN

CHICAGO, ILLINOIS
JUNE 2018

This thesis is dedicated to my family.

TABLE OF CONTENTS

List of Figures

Acknowledgements

I would like to thank my advisor, Prof. Yossi Weizmann, for his support and guidance throughout my graduate studies. I remember meeting with Yossi his first week in Chicago when I was an undergraduate student asking for a chance to study and begin research in his new group. His continued generosity has allowed me to stay here throughout my research career and grow in parallel with the expansion and diversity of research within the lab. He also afforded me tremendous opportunities to teach and explore other facets of academic research. He is directly responsible for my growth professionally, scientifically, and academically, and I am truly grateful.

I would like to express my gratitude to Prof. Joseph Piccirilli and Prof. Bozhi Tian for serving on my thesis committee. Their thoughtful suggestions and critical review of my research was constructive and appreciated. I would be remiss if I did not also thank Prof. Sergey Kozmin, Prof. Yamuna Krishnan, and Prof. Bryan Dickinson for serving on my candidacy committee. Their encouragement and discussions have helped direct and frame my research goals in the broader scientific landscape. I would like to give a special thank you to Prof. Greg Hillhouse, who served as an undergraduate mentor and friend and convinced me to pursue research in chemistry.

The culmination of a thesis is not the accomplishment of an individual, but a tremendous achievement for the group. None of this work would have been possible without the help from all the Weizmann group members, collaborators, and staff members. I would like to especially thank, Dr. Leilei Tian, Dr. Jung-Hoon Lee, Dr. Zoya Cheglakov, Dr. Gang Chen, Dr. Di Liu, Kyle Gibson, Huw Rees, Usman Ahkter, Ted Gannett, Margaret Lee, and Adam Coleman.

Chemistry research requires guidance, support, and understanding from many sources and in many forms. Each of these people helped me continue and succeed, and I am very grateful to all of them.

I could never delineate the innumerable contributions and support given to me over the course of my graduate studies by the other students in the Department of Chemistry. Beyond their scientific expertise and insights, the commiseration, motivation, and necessary distractions has made my time here both productive and enjoyable.

Most importantly, I want to thank my family. My parents, David and Catherine, thank you for their unconditional love and support through all the years of school. You instilled a thirst for knowledge and the value of asking questions. This work, more than anything, has been the culmination of your lifelong teaching. My siblings, David, Andrew, and Ciara, for the communal growth and discussions we had at the dinner table trying to better understand the world. Fiona, as a constant source of inspiration, I cannot imagine going through this without you and I am thankful every day for your support.

Abstract

Through the integration of metallic nanoparticles with various nucleic acid amplification systems and other bioanalytical techniques we focused on interfacing biology, chemistry, nanotechnology, and materials sciences to address both fundamental and application-driven challenges in the multidisciplinary research space. These exciting frontiers offer unparalleled opportunities for designing groundbreaking advances in medical diagnostics, optically responsive materials, and complex self-assemblies. Using nucleic acids as the backbone for our research allows the exploitation of their well-defined and highly programmable structure to achieve organization with nanoscale precision. By manipulating these biopolymers, we are looking for a deeper understanding of the relationship between structure and function and new avenues to use these processes for the controllable self-assembly of biological components and other nanomaterials. The combination of these research interests has led to exciting themes which encompass the broad nature of our research and promote multifaceted expansion and many opportunities for future interdisciplinary projects.

Capitalizing on the unique properties of colloidal gold nanoparticles, we have developed creative solutions which employ these to improve existing nucleic acid amplifications. Beginning with the simple involvement of the particles as directing and concentrating agents to bring the reaction components of isothermal nucleic acid amplification together to increase their dynamical interactions, we dramatically improved the specificity and sensitivity of this assay. Looking deeper into the properties of the particles, we demonstrated that the photothermal capabilities were tunable and could be optimized to provide an alternative way to heat reaction mixtures rapidly, accurately, and without compromising the integrity of the reactions. Finally, by relying on the plasmonic response particles incur when they are brought within close proximity

to each other, we developed an actuator which uses this plasmonic response as the reporter for the structural change that results from different environmental conditions. Our studies, which have direct applications, deepen our fundamental understanding of the optical properties of various metallic particles and address current opportunities to ultimately improve bioanalytical techniques.

Chapter 1 - Introduction

The desire to monitor the world at the molecular level has driven the development of countless methods of analysis, signal amplification, and creative research protocols. X-ray crystallography, NMR, and PCR, among many others have been created to help researchers visualize and understand the relationship between structure and function of a variety of materials. One of the most influential of the resulting discoveries was the formalization of the double helix structure of DNA[1]. This unlocked a deeper understanding of the biological world and was the foundation for our conception of molecular biology. During the recent three decades, DNA has found its function as the building material for the construction of nanostructures in the field of structural DNA nanotechnology, especially on the higher-order structural features of DNA such as knots, nanoparticle assemblies, and protein-nucleic acid scaffoldings. It is from this basis set of knowledge that the nucleic acid amplification methods were designed and the field of DNA nanotechnology grew, as they rely on the precise hybridization and, in the case of the plasmonic actuator, the 3-D conformation to achieve the predicted results. The combination of the structural understanding of DNA and the methods related to nucleic acid amplification with the field of metallic nanoparticles represents the focus of my graduate research

1.1 Nucleic Acid Amplifications

The field of nucleic acid amplifications (NAAs) needs little introduction, as it has continually proven to be the standard for detection and analysis across many research disciplines and offers tremendous power for studying molecular interactions in real time. Briefly, however, nucleic acid amplification techniques are basic tools in molecular biology with widespread applications in biology and medical research[2]. Beginning with the discovery of the polymerase chain reaction in 1987, they

have featured unprecedented sensitivity. These amplification techniques generally employ repeated enzymatic reactions to make numerous copies of a sequence initially present at a low concentration[3].

The most widely used NAA technique is the Polymerase Chain Reaction (PCR), which uses a thermophilic polymerase to make multiple copies of a target sequence through repeated steps of annealing, polymerizing, and denaturing. This yields exponential amplification and represents the benchmark for all NAAs. However, this method, though powerful, is not without limitations, specifically relating to the long assay duration and expensive instrumentation[4-5]. Some isothermal NAA methods with higher flexibility for bio-diagnostics using strategies distinct from PCR have been developed[6]. These methods can reach specificity and sensitivity equivalent to PCR and have no need for the thermal-cycling protocol. Thus, they simplify some special requirements allowing for a wider range of applications, such as point-of-care diagnosis[7], *in situ* detection[8], on-chip detection,[9] and naked-eye detection[10]. Also, some of the isothermal methods are more adaptable to specific biomolecular targets for which PCR would have to use very sophisticated protocols. For example, short-length micro-RNA sequences could be directly amplified and detected by the isothermal exponential amplification reaction (EXPAR) method[11], obviating the reverse transcription step required by PCR. The isothermal NAA methods show attractive potentials and act as the perfect complement to the PCR technique; however, they suffer the problems common in enzymatic reactions,[12] such as being sensitive to contaminations and intolerance to the inhibitory components from crude samples, which limit their reliability in clinical applications. In particular, the knowledge of these isothermal NAA methods, especially in regards to specificity, is still not as comprehensive as that of PCR, which further impedes their applications for diagnostic clinical practices. Therefore it is important to continue to deepen our understanding in both classes of these NAAs to strengthen our arsenal of tools for biological, chemical, and medical analysis.

1.2 Metallic Nanoparticles

Beginning with the Lycurgus Cup from the 4th century, we can trace the history of metallic and colloidal nanoparticles as they evolved from purely decorative and artistic materials to a mainstay in academic and medical research[13-14]. This bridge to understanding these materials on a chemical and physical level was first reported by Richard Adolf Zsigmondy which began the process of deriving the differences in the bulk properties of these materials and their behaviors as colloidal nanoparticles.

Gold nanoparticles (AuNPs) have several unique physical properties which make them attractive for a variety of applications. Furthermore, the particles have additional properties when in the colloidal solutions or arrays versus as individual particles. Particularly interesting about the gold nanoparticles we have used through this research is that different shapes, such as spheres, rods, or bipyramids, can express the different properties to various extents. It should be noted that throughout this work I will be referring to various shapes of these nanoparticles such as spheres, rods, and bipyramids, and that the general term nanoparticle will most often refer to nanospheres, unless otherwise specified. In recent years, researchers have enthusiastically applied AuNPs of many shapes and their remarkable properties to achieve drastic far-reaching results[15-25]. Many interesting phenomena, such as surface-plasmon coupling, exciton coupling, and magnetic coupling, originate from the directed assembly of these particles to promote these specific interactions[26-28]. Unfortunately, the synthesis of discrete nanoparticle self-assemblies has challenged the nanotechnology field for decades and has limited the study of nanoparticle interactions and the advance of nanomachinery. The use of various partial polymer encapsulation techniques has opened the door to eccentrically labeling particles for these purposes[29]. With this

framework, which will be discussed in more depth in chapter 4, we have applied our own method to specifically label gold nanospheres and nanorods to begin probing some of these properties.

1.3 Scope of Thesis

My graduate studies have focused mainly on the application of gold nanoparticles to bioanalytical techniques to provide alternative strategies for improved signal detection amplification and to eliminate current limitations found in traditional lab protocols. Using gold nanospheres, nanorods, and nanobipyramids, we have shown several advances in isothermal and thermocycling protocols. The varying shape of these metallic nanoparticles allowed us to exploit both their physical properties and optical properties to achieve our research goals, as will be discussed in the following chapters.

Chapter 2 presents the use simple gold-nanoparticles to improve the sensitivity and specificity of an isothermal nucleic acid amplification protocol. This addition showed drastic improvement in the detection of telomerase, especially when using crude cell lysates. We further investigated the mechanism by which these processes occurred and the overall dynamic arrangement of the reaction components.

Chapter 3 describes our application of the photothermal properties of gold nanobipyramids to the polymerase chain reaction as an alternative heating source. This method was able to achieve rapid and real-time analysis and showed great flexibility in accommodating other techniques relevant to biology and chemistry.

In Chapter 4, gold nanoparticles, which were labeled with short oligonucleotides, are employed to detect macroscopic environmental changes, such as pH, through their coupled plasmonic response. This responsive action was programmed using non-canonical DNA

hybridizations, the formations of which are dependent on the stimuli. Furthermore, this study probed the varying levels of plasmonic coupling as a direct comparison of different nanoparticle dimers was achieved.

The thesis concludes with Chapter 5, which will discuss these results and the fields of nucleic acid amplification and metallic nanoparticles in a broader context. Future research directions and my hopes for this science are also humbly provided.

1.4 References

1. Watson, J. D.; Crick, F. H., Molecular structure of nucleic acids; a structure for deoxyribose nucleic acid. *Nature* **1953,** *171* (4356), 737-8.

2. Liu, J.; Cao, Z.; Lu, Y., Functional nucleic acid sensors. *Chem Rev* **2009,** *109* (5), 1948-98.

3. Mullis, K. B.; Faloona, F. A., [21] Specific synthesis of DNA in vitro via a polymerase-catalyzed chain reaction. In *Methods in Enzymology*, Academic Press: 1987; Vol. Volume 155, pp 335-350.

4. Valasek, M. A.; Repa, J. J., The power of real-time PCR. *Adv Physiol Educ* **2005,** *29* (3), 151-9.

5. Bustin, S. A.; Benes, V.; Nolan, T.; Pfaffl, M. W., Quantitative real-time RT-PCR--a perspective. *J Mol Endocrinol* **2005,** *34* (3), 597-601.

6. Kim, J.; Easley, C. J., Isothermal DNA amplification in bioanalysis: strategies and applications. *Bioanalysis* **2011,** *3* (2), 227-39.

7. Craw, P.; Balachandran, W., Isothermal nucleic acid amplification technologies for point-of-care diagnostics: a critical review. *Lab Chip* **2012,** *12* (14), 2469-86.

8. Maruyama, F.; Kenzaka, T.; Yamaguchi, N.; Tani, K.; Nasu, M., Detection of bacteria carrying the stx2 gene by in situ loop-mediated isothermal amplification. *Appl Environ Microbiol* **2003,** *69* (8), 5023-8.

9. Ahmad, F.; Hashsham, S. A., Miniaturized nucleic acid amplification systems for rapid and point-of-care diagnostics: a review. *Anal Chim Acta* **2012,** *733*, 1-15.

10. Gill, P.; Alvandi, A. H.; Abdul-Tehrani, H.; Sadeghizadeh, M., Colorimetric detection of Helicobacter pylori DNA using isothermal helicase-dependent amplification and gold nanoparticle probes. *Diagn Microbiol Infect Dis* **2008,** *62* (2), 119-24.

11. Jia, H.; Li, Z.; Liu, C.; Cheng, Y., Ultrasensitive detection of microRNAs by exponential isothermal amplification. *Angew Chem Int Ed Engl* **2010,** *49* (32), 5498-501.

12. Wilson, I. G., Inhibition and facilitation of nucleic acid amplification. *Appl Environ Microbiol* **1997,** *63* (10), 3741-51.

13. Summers, H. D., *Nanomedicine*. Elsevier Science: 2013.

14. Catherine, L.; Olivier, P., *Gold Nanoparticles For Physics, Chemistry And Biology (Second Edition)*. World Scientific Publishing Company: 2017.

15. Xia, Y.; Xiong, Y.; Lim, B.; Skrabalak, S. E., Shape-Controlled Synthesis of Metal Nanocrystals: Simple Chemistry Meets Complex Physics? *Angewandte Chemie-International Edition* **2009,** *48* (1), 60-103.

16. Huang, X.; Neretina, S.; El-Sayed, M. A., Gold Nanorods: From Synthesis and Properties to Biological and Biomedical Applications. *Advanced Materials* **2009,** *21* (48), 4880-4910.

17. Prodan, E.; Radloff, C.; Halas, N. J.; Nordlander, P., A hybridization model for the plasmon response of complex nanostructures. *Science* **2003,** *302* (5644), 419-422.

18. Sun, Y. G.; Xia, Y. N., Shape-controlled synthesis of gold and silver nanoparticles. *Science* **2002,** *298* (5601), 2176-2179.

19. Xia, Y. N.; Yang, P. D.; Sun, Y. G.; Wu, Y. Y.; Mayers, B.; Gates, B.; Yin, Y. D.; Kim, F.; Yan, Y. Q., One-dimensional nanostructures: Synthesis, characterization, and applications. *Advanced Materials* **2003,** *15* (5), 353-389.

20. Langille, M. R.; Zhang, J.; Personick, M. L.; Li, S.; Mirkin, C. A., Stepwise Evolution of Spherical Seeds into 20-Fold Twinned Icosahedra. *Science* **2012,** *337* (6097), 954-957.

21. Jin, R. C.; Cao, Y. C.; Hao, E. C.; Metraux, G. S.; Schatz, G. C.; Mirkin, C. A., Controlling anisotropic nanoparticle growth through plasmon excitation. *Nature* **2003,** *425* (6957), 487-490.

22. Zhu, M.; Aikens, C. M.; Hollander, F. J.; Schatz, G. C.; Jin, R., Correlating the crystal structure of A thiol-protected Au-25 cluster and optical properties. *Journal of the American Chemical Society* **2008,** *130* (18), 5883-5884.

23. Alivisatos, A. P., Semiconductor clusters, nanocrystals, and quantum dots. *Science* **1996,** *271* (5251), 933-937.

24. Sun, S. H.; Zeng, H., Size-controlled synthesis of magnetite nanoparticles. *Journal of the American Chemical Society* **2002,** *124* (28), 8204-8205.

25. Lee, J.-H.; Gibson, K. J.; Chen, G.; Weizmann, Y., Bipyramid-templated synthesis of monodisperse anisotropic gold nanocrystals. *Nature Communications* **2015,** *6*.

26. Nie, Z.; Petukhova, A.; Kumacheva, E., Properties and emerging applications of self-assembled structures made from inorganic nanoparticles. *Nature Nanotechnology* **2010,** *5* (1), 15-25.

27. Li, F.; Josephson, D. P.; Stein, A., Colloidal Assembly: The Road from Particles to Colloidal Molecules and Crystals. *Angewandte Chemie-International Edition* **2011,** *50* (2), 360-388.

28. Kuzyk, A.; Schreiber, R.; Fan, Z.; Pardatscher, G.; Roller, E.-M.; Hoegele, A.; Simmel, F. C.; Govorov, A. O.; Liedl, T., DNA-based self-assembly of chiral plasmonic nanostructures with tailored optical response. *Nature* **2012,** *483* (7389), 311-314.

29. Tan, L. H.; Xing, S.; Chen, T.; Chen, G.; Huang, X.; Zhang, H.; Chen, H., Fabrication of Polymer Nanocavities with Tailored Openings. *ACS Nano* **2009,** *3* (11), 3469-3474.

Chapter 2 – Enhancing effect of gold-nanoparticles

2.1 Introduction

The isothermal nicking enzyme-mediated strand displacement amplification (NE-SDA) uses a restriction enzyme to nick at a specific site and a polymerase to initiate a new cycle of replication from the 3′-OH end of the nick, which can exponentially amplify the target sequence at a fixed temperature[1-5]. Recently, a real-time in vitro detection method of telomerase activity, exponential isothermal amplification of telomere repeat (EXPIATR),[6] was developed based upon a programmed path of NE-SDA reactions (Figure 2.1). Although EXPIATR and some other NAA methods for telomerase detection, like the PCR-based telomeric repeat amplification protocol (TRAP), can reach the excellent sensitivity of a single cancer cell, their reliability in clinical diagnosis is still questioned[7-13]. One potential problem is the risk of generating false-negative results due to the presence of inhibitors of the amplification reactions in the analysis of total protein cell extracts[14]. As telomerase activity appears early in pathogenesis of many cancers, telomerase is especially important for the early detection of cancer[15]. The newly developed methods prefer using some minimally-invasive or non-invasive samples, like biopsy specimens and body-fluid samples for early detections, which could require the assay to be applied to samples with a minute amount of cancer cells in a background of hundreds or even thousands of normal cells[16-17]. This reveals more challenges for telomerase detection; besides the high sensitivity, a good specificity is required to minimize the influences from the background. The TRAP assay, which has been evaluated in clinical studies, attempted to overcome the false-negative problem by removing the inhibitors from samples prior to the amplification process via phenol/chloroform extraction,[18] biotin affinity labeling and extraction,[19] or by using an “internal standard” DNA strand as a reference to monitor the efficiency of the specific

amplification[20]. However, these methods complicate the simplicity of the assay and increase the risk of introducing carry-over contaminations.

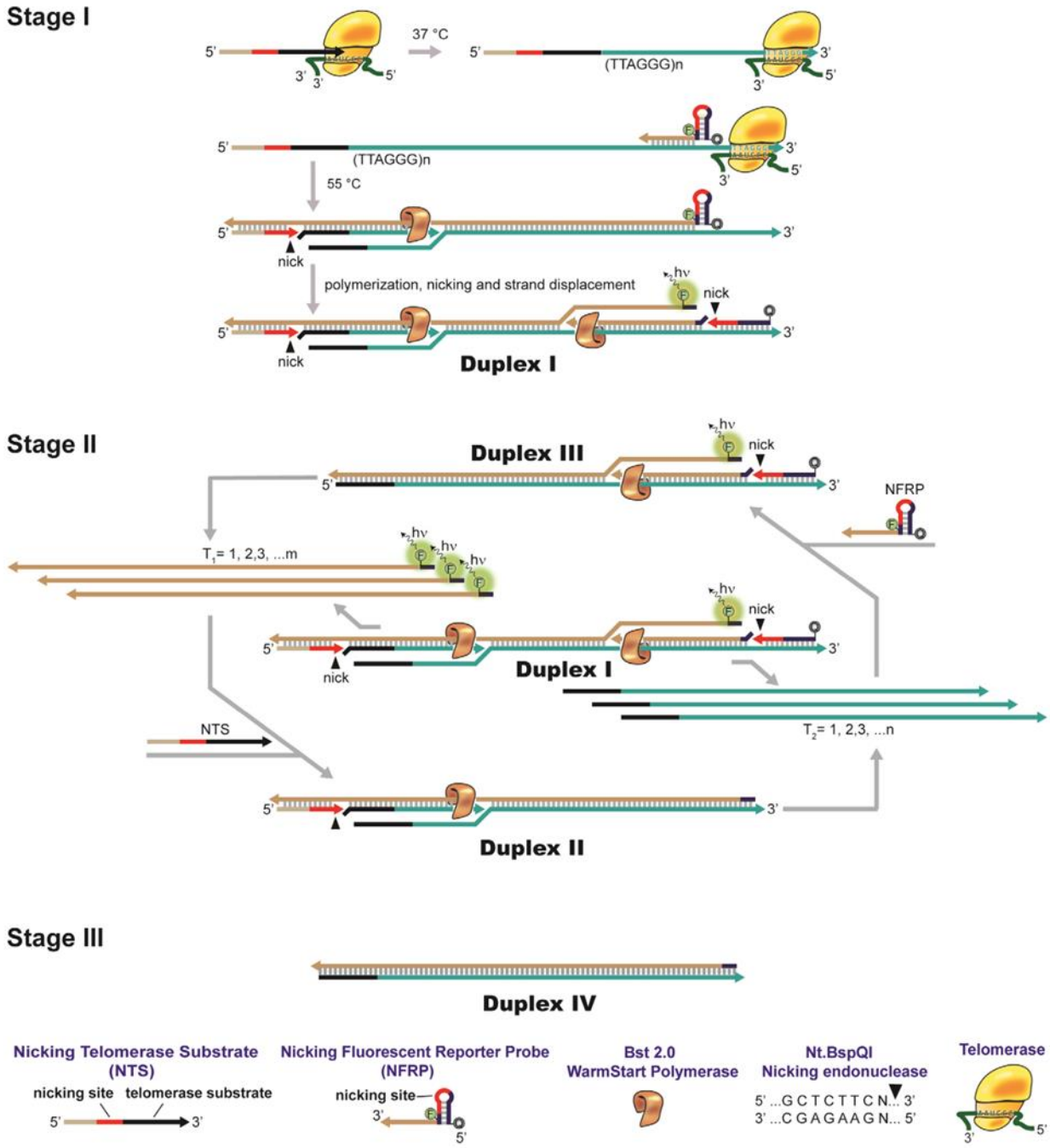

Figure 2.1 Schematic representation of EXPIATR Assay

Some pioneering work has been done using gold nanoparticles (AuNPs) to improve the PCR performance in different error-prone systems[21-26]. For example, it was found that AuNPs could enhance the specificity of the allele-specific PCR for single nucleotide polymorphism (SNP) genotyping and haplotyping[26]. Primer-modified AuNPs have also been used to perform the TRAP assay and observed that such a modification could significantly improve the selectivity and sensitivity of telomerase activity detection on complex samples[9]. In this chapter we report the effect of AuNPs on improving the specificity of isothermal NE-SDA reactions and resolving the issues of the EXPIATR assay when performed on complex, protein-rich samples. In addition, this chapter will provide more evidences to validate the role of AuNPs in enhancing the reactions of nucleic acids, as according to our knowledge, the AuNP effect has not previously been studied in an isothermal amplification system.

The isothermal NE-SDA reactions under different situations of low-specificity, either caused by the external interference of cell lysates or caused by the polymerase, were investigated through the addition of AuNPs. The power of AuNPs in enhancing and reforming the NE-SDA reactions has been well demonstrated; furthermore, it was revealed that the addition of AuNPs could also inhibit the non-specific reactions, especially for the restriction-endonuclease-DNA-polymerase (RE-pol) DNA synthesis. As a ubiquitous non-specific reaction for NE-SDAs, the RE-pol DNA synthesis is the DNA-independent synthesis which produces new DNA strands from dNTPs using only enzymes without any templating or priming DNA strands. This kind of non-specific reaction has not been well understood and lacks efficient suppressing methods, resulting in a major impediment to the practical applications of the NE-SDA methods[3]. A report found that the single-stranded DNA binding protein T4 bacteriophage gene 32 (T4gp32) could inhibit the RE-pol DNA synthesis;[27] our observation suggests that AuNPs might also be inhibitors to this poorly understood non-specific reaction. Also,

thanks to the sensitive response of the surface plasmon of AuNPs to the environment, the interaction between AuNPs and the reaction components was monitored by UV-Vis spectroscopy, which aided in further understanding the way AuNPs influence the amplification reactions and in tuning the concentration of AuNPs. Taking advantage of such AuNP effects, the EXPIATR assay could overcome the inhibitory effect induced by concentrated cellular proteins and, as a result, maintain its sensitivity on complex, protein-rich samples. For example, for complex samples of various cancer cells in the presence of 100-fold foreign normal cells, the detection sensitivity achieved by the AuNP-based assay was significantly improved, an increase by as much as five-fold, as compared with the traditional assay. Moreover, besides making the EXPIATR assay applicable for complex clinical samples, this study shows broad significance in understanding the essential role of AuNPs in enhancing the isothermal nucleic acid amplifications and promoting their clinical applications (the contents of this chapter are adapted from a published paper[28]).

2.2 Results and discussion

2.2.1 Capabilities of original EXPIATR assay with complex samples

The EXPIATR assay developed by our group is a sensitive assay for telomerase, and has been verified with tests on pure cancer cells from established cell lines (Figure 2.2)[6]. However, more challenges will be faced before advancing to further clinical practice, as clinical samples are more complex. The TRAP assay has encountered the problems of the complex matrix of clinical samples which include inhibitors of the amplification reactions and yield false-negative results[14]. The telomerase activity of a given sample was quantified based on a relative standard curve method referenced from the TRAP assay[29]. Generally, telomerase activity is expressed relative to a standard sample by this method. In our assay, the HeLa cancer cell (which shows medium to high telomerase activity) was chosen as a standard.

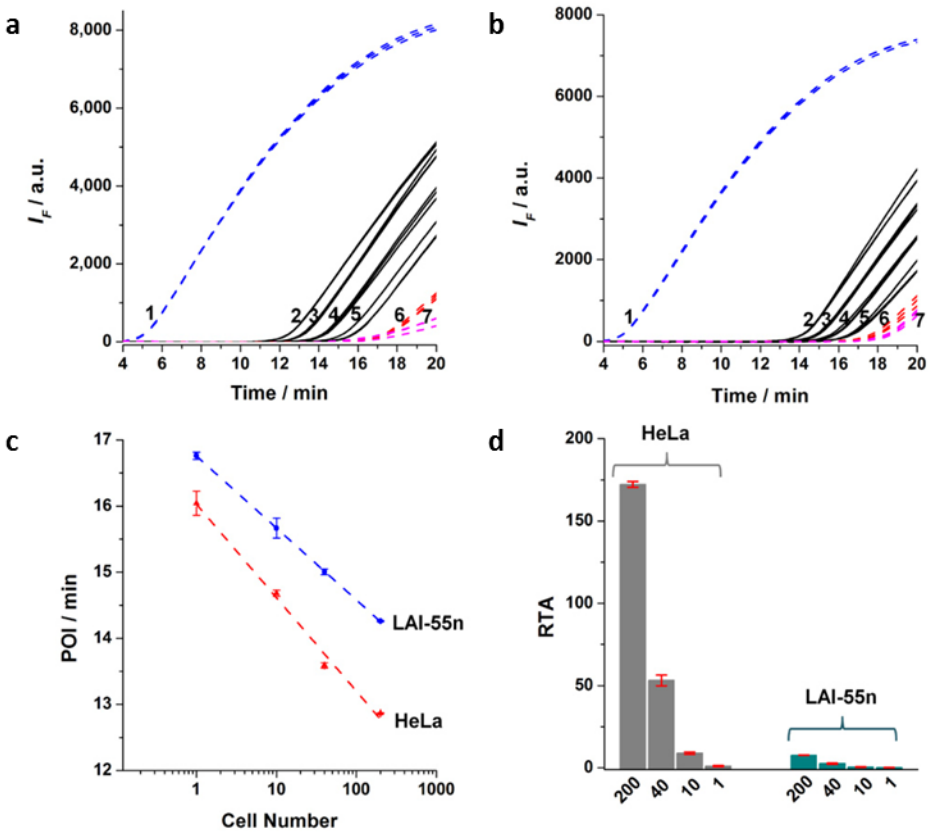

Figure 2.2 Detection of telomerase activities in human HeLa cancer cells and in human LAI-55 neuroblastoma cells by the EXPIATR assay (a) The assay tested on HeLa cell extracts and (b) the assay tested on LAI-55n cell extracts included: the amplification curves of TPC8 positive control (1×10^{-11} M) (1), 200 cells, 40 cells, 10 cells and 1 cell equivalent extracts (2-5), negative control in absence of cell extracts (6), and heat-inactivated extracts (1000 cells equivalence) (7); (c) Standard curves of the assay for HeLa cell extracts (1) and the assay for LAI-55n cell extracts; (d) The RTAs of HeLa cells and LAI-55n cells. Error bars indicate standard error of triplicate tests. The equation is: *RTA* = 10a RTA: the relative telomerase activity; Y-int: the Y-intercept of the standard curve of the standard assay based on HeLa cancer cell; Slope: the slope of the standard curve of the standard assay based on HeLa cancer cell; POI-sample: the POI value of the amplification curve of an unknown sample; POIIR-standard: the POI value of the amplification curve of TPC8 positive control in the standard assay; POIIR sample: the POI value of the amplification curve of TPC8 positive control in the assay of unknown sample.

The telomerase activity of an unknown sample was evaluated by comparison with the standard curve of the HeLa cell line and expressed by the number of HeLa cancer cells that can generate the same level of signal as the unknown sample. In addition, each test was normalized

by the positive control (10^{-11} M TPC8) performed in the same experiment. Different cell lines, cervical cancer (HeLa), breast cancer (MDA-MB-231 and HCC-38), bladder cancer (UM-UC-3), neuroblastoma (LAI-55n), and lung fibroblast normal cells (MRC-5) were tested and their telomerase activities were quantified. MRC-5 was found telomerase-negative; HeLa, MDA-MB-231, HCC-38 and UM-UC-3 displayed moderate to high telomerase activities, which is in accordance with the results of other telomerase detection methods[7]. The neuroblastoma cell line LAI-55n showed a relatively low RTA, i.e. the extract from 200 LAI-55n cells exhibited telomerase activity equivalent to the extract from ~ 8 HeLa cancer cells (Figure 2.2d). Although LAI-55n showed much lower telomerase activity than HeLa, the standard curves for both HeLa and LAI-55n are linear over the tested cell number range (from 200 to 1 cell), suggesting that EXPIATR is a specific and sensitive method for telomerase detection.

To further characterize the capability of the EXPIATR assay, it was tested on complex samples which were enriched with cell lysates of normal cells (Figure 2.3). For the complex samples containing a certain amount of cancer cell extracts (from HeLa cell line) and the extracts of 1000 foreign cells (from MRC-5 cell line), the real-time amplification curves showed obvious differences from that of the corresponding pure samples containing the same amount of cancer cell extracts (Figure 2.3a). When the interferants in the complex samples were further increased to a total protein extract from 4000 foreign cells, the detections of telomerase activity in such complex, protein-rich samples were significantly inhibited (Figure 2.3b). The transformation of the real-time results into the quantitative relative-telomerase-activity (RTA) values revealed that only 20% of the telomerase activity of the pure HeLa cancer cell extracts was detectable for the complex samples containing 1000 normal cells (Figure 2.3c) and less than 5% of the telomerase activity of cancer cells could be expressed in the complex samples containing 4000 normal cells. All of these results indicate that the

sensitivity of the EXPIATR assay was greatly affected by the presence of foreign cell lysates in a given sample; the more foreign cell lysates included, the more inhibited the assay would be, in comparison with the assay performed on pure cancer cells. A similar effect was observed with the TRAP assay in which the addition of 5000 normal cells would almost completely inhibit the amplification of the elongated telomerase products[9].

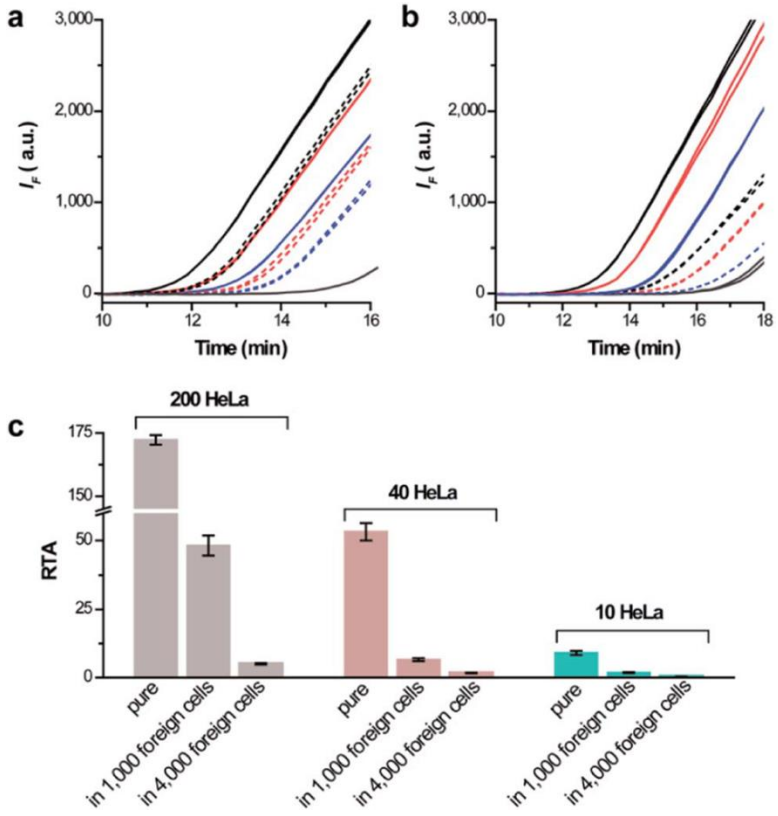

Figure 2.3 Real-time EXPIATR assay performed on the extracts of HeLa cancer cells Pure (solid) and in the presence of a high concentration of foreign normal cell lysates (dashed): 200 cancer cells (black), 40 cancer cells (red), 10 cancer cells (blue), in the presence of extracts of 1000 normal cells (a) and in the presence of extracts of 4000 normal cells (b), and the non-template controls were also present (solid grey) (duplicate measurements of each concentration); the real-time results are transformed to quantitative RTA values and summarized (c). Error bars indicate standard error of triplicate tests.

2.2.2 The enhancing-effect of AuNPs on the DNA strand displacement amplifications

As telomerase detection is carried out on cellular protein extracts, any purification strategy to diminish the inhibitory effect of interfering cell lysates has to be performed after the telomerization

step. A pre-amplification step would increase the operation complexity and reduce the reliability of the results. Alternatively, several studies have revealed that gold colloids improve the performance of PCR in a wide variety of error-prone systems[21-22, 26]; more importantly, several of these AuNP-based methods are ready-for-use with no need for making significant changes to the original protocols. Hence, we developed an AuNP-based assay with the addition of 0.4 nM citrate-capped AuNPs to the traditional EXPIATR assay (Figure 2.4). The optimal concentration of 10 nm citrate-capped AuNPs for the EXPIATR-AuNP assay was assessed by the amplifications of TPC8 template (1×10^{-13} M). As shown in Figure 2.4, the solid curves correspond to amplifications of TPC8 template in the presence (red) and absence of (black) concentrated cell lysates equivalent to 4000 normal cells; while the dashed curves correspond to non-template controls in the presence (red) and absence of (black) normal cells.

From top to bottom, different concentrations of citrate-capped AuNPs (from 0 to 0.5 nM) were mixed with the reactions to study the concentration effect of AuNPs. In the absence of AuNPs, the amplification curve of TPC8 template showed a delayed point of inflection (POI) value when cell lysates were presented in the reaction, implying the amplification reaction was inhibited by the cell lysates. Along with the addition of more AuNPs, the inhibitory effect of cell lysates on the amplification reactions was gradually reduced. Meanwhile, the amplifications of pure TPC8 template would not be significantly affected until the concentration of AuNPs reached 0.4 nM; however, the amplification rates (efficiency) started to decrease significantly when more than 0.4 nM AuNPs were used. This is in accordance with previous studies about PCR which report an appropriate concentration of nanomaterials may improve PCR, but an excessive concentration may inhibit the amplification process[21]. To make the method compatible

to the tests of complex samples but also pure samples, Figure 2.4 demonstrates that 0.4 nM AuNPs should be the optimal concentration for the EXPIATR-AuNP assay.

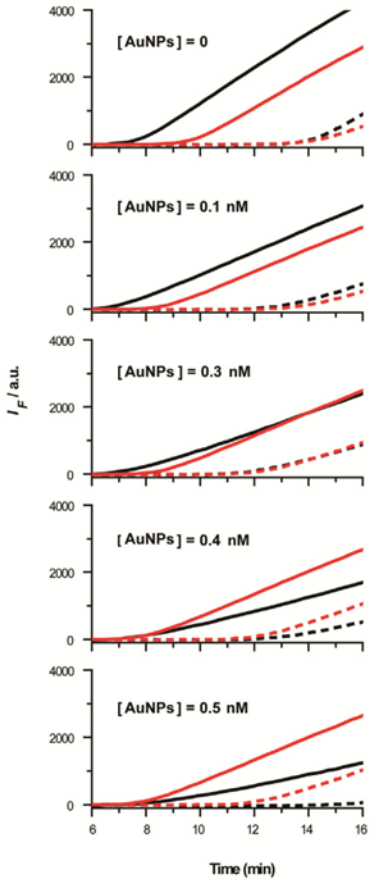

Figure 2.4 Concentration effect of 10 nm citrate-capped AuNPs on the assay The concentration effect was assessed by the amplification reaction of TPC8 template (1×10^{-13} M) (solid) and by the corresponding non-template controls (dashed), in the presence (red) and in the absence of (black) concentrated cell lysates equivalent to 4000 normal cells.

Figure 2.5 shows the real-time results of employing the AuNP-based assay to detect HeLa cancer cells alone and in presence of foreign matters. In the presence of extracts of 1000 foreign normal cells, the complex samples produced almost identical amplification signals to the corresponding pure samples (Figure 2.5a) indicating the inhibitory effect from 1000 foreign cells was almost completely eliminated by the addition of AuNPs. Even for the complex samples with the presence of 4000 foreign cells, the performance of the AuNP-based assay was significantly improved compared with that of the

traditional assay (Figure 2.5b), *i.e.* > 20% of the telomerase activity of cancer cells can be expressed in the complex samples (Figure 2.5c), in contrast to < 5% detectable by the traditional assay. As a further test, we checked different cancer cell lines in the presence of a 100-fold excess of foreign cell extracts (*i.e.* extracts from 40 cancer cells were doped in the extracts of 4000 normal cells) by the AuNP-based assays (Figure 2.5c). For all of the cancer cell lines, the addition of AuNPs significantly improved the sensitivity for telomerase detection in complex samples, over five-fold as compared with the traditional assays (Figure 2.6).

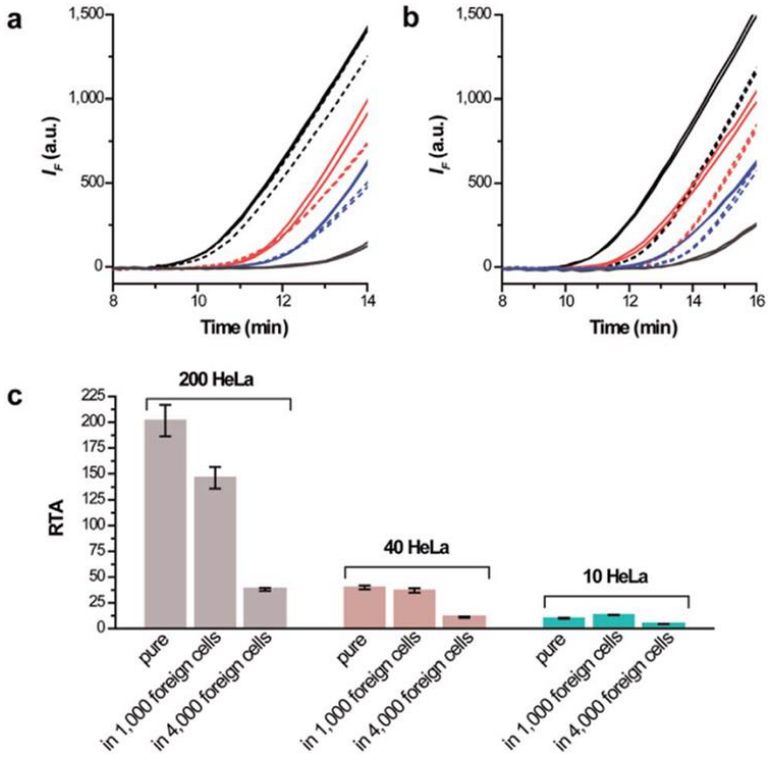

Figure 2.5 Real-time EXPIATR-AuNP assay performed on the extracts of HeLa cancer cells Pure (solid) and in the presence of a high concentration of foreign cell lysates (dashed): 200 cancer cells (black), 40 cancer cells (red), 10 cancer cells (blue), in the presence of extracts of 1000 normal cells (a) and in the presence of extracts of 4000 normal cells (b), and the non-template controls were also present (grey solid) (duplicate measurements of each concentration); the real-time results are transformed to quantitative RTA values and summarized (c). Error bars indicate standard error of triplicate tests.

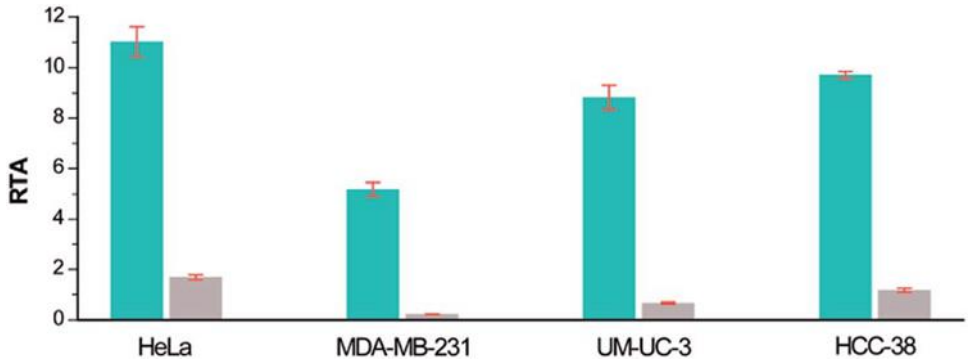

Figure 2.6 Comparison of the RTAs of different cell lines as measured by the EXPIATR-AuNP and EXPIATR assays The EXPIATR-AuNP assay (green) and the EXPIATR assay (grey) were performed respectively on cell extracts equivalent to 40 cancer cells of different cancer cell lines in the presence of a high concentration of foreign cell lysates (equivalent to 4000 normal cells), and the resulting RTAs were quantified. Error bars indicate standard error of triplicate tests.

As the citrate-capped AuNPs were suspended in a cocktail solution which may contain some impurities besides gold nanoparticles [22], it is necessary to further verify that the AuNPs are the essential component working for the EXPIATR-AuNP assay. We used the Nanosep centrifugal device with Omega membrane MWCO 3 kDa to replace the storing liquid of the gold colloid solution with pure water. The purchased gold colloid (Figure 2.7a), the purified gold colloid in water (Figure 2.7b), and the filtrate (storing liquid of the gold colloid) collected from the Nanosep device (Figure 2.7c) were used as additives to the EXPIATR assay and tested respectively. In Figure 2.7, the solid cyan curves are the amplifications of cell extracts of 200 HeLa cancer cells; the dashed curves are the amplifications of cell extracts of 200 HeLa cell cells doped in 4000 MRC-5 normal cells with the presence of the corresponding additives. We observed that the gold colloids both purchased and purified could suppress the inhibitory effect caused by the concentrated cell lysates on the amplification reactions, however, the filtrate collected from the centrifugal device (storing liquid of the gold colloid) could not decrease the inhibitory effect at all. It indicates that AuNPs are indeed the essential component working for the EXPIATR-AuNP assay.

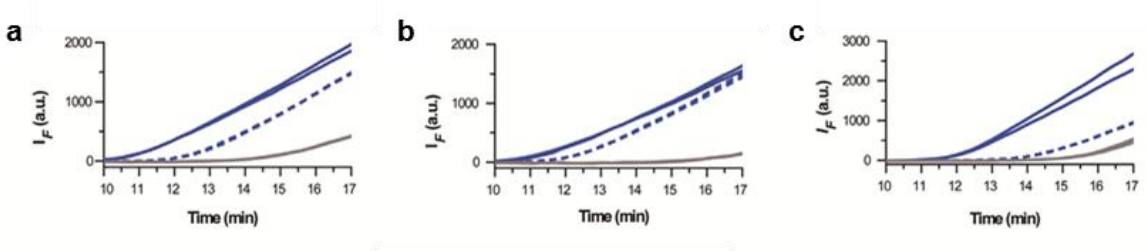

Figure 2.7 The amplifications of extracts of 200 HeLa cancer cells In the absence of (solid cyan) and in the presence of (dashed cyan) concentrated cell lysates, as well as the corresponding non-template controls (solid grey); For the detections on complex cell extracts (dashed cyan), different additive were present: a) the purchased gold colloid, b) the purified gold colloid, and c) the storing liquid of the purchased gold colloid collected from the centrifuge device.

To further study of the roles of cell lysates and AuNPs, the amplified products collected from different assays were visualized by polyacrylamide gel electrophoresis (PAGE) (Figure 2.8). The assays were monitored by real-time fluorescence, quenched shortly after the non-template controls started to generate signals, and applied to the PAGE analysis directly. According to the principle of EXPIATR (Figure 2.1), a ladder of products with 6 bp increments will be produced. Figure 2.8a shows the assays tested on complex samples containing 1000 normal cell lysates and Figure 2.8b shows the assays tested on complex samples containing 4000 normal cell lysates. The names of pure samples and complex samples are differentiated by suffix 'p' (for pure samples) and 'c' (for complex samples); the AuNP-based assays are differentiated from the traditional assays by adding primes (′) to the names. Using the gel analysis, two main findings were revealed in regards to the roles of the normal cell lysates and AuNPs.

First the gel image verified that the abundance of foreign cell lysates in the complex samples would inhibit the specific amplifications. In the presence of 1000 normal cell lysates, the traditional assays (Lane 1p *vs.* 1c and Lane 2p *vs.* 2c) show reduced intensities of the specific bands as compared with the product bands amplified from the pure samples; such inhibition effects were more significant when the interferant amount was increased to 4000 normal cells (Lane 3p *vs.* 3c, Lane 4p *vs.* Lane 4c,

and Lane 5p *vs.* 5c), *i.e.* the specific amplifications were significantly inhibited, while the non-specific products (based on the shift of the gel pattern of the negative control in Lane 6p) were increasingly amplified. This is especially true for the case in which a very small quantity of cancer cell extracts was present in the protein-rich background. For example in Lane 5c, the amplification products of the complex sample consisting of the extracts of 10 HeLa cancer cells and a 400-fold excess of foreign cell lysates were seriously predominated by the non-specific products, which produced much less of the specific products as compared with the assay directly performed on the same amount of pure cancer cell extracts (Lane 5p).

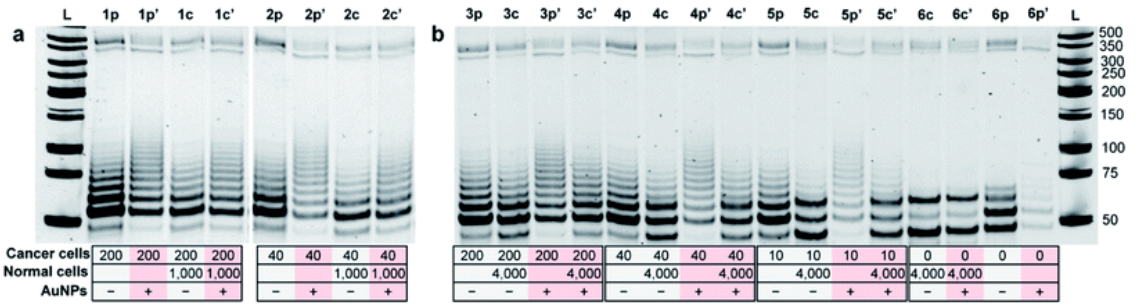

Figure 2.8 Native PAGE analysis of the traditional EXPIATR assay and the AuNP-based assay Tested on the extracts of HeLa cancer cells, pure and in the presence of a high concentration of foreign cell lysates: (a) the assays tested on complex samples containing 1000 normal cell lysates; (b) the assays tested on complex samples containing 4000 normal cell lysates.

Further we found that, whether performed on pure samples or complex samples, the AuNP-based assays showed improved specificity compared with the corresponding traditional assays[30]. For the detections of pure cancer cells, the traditional assays already showed good specificities without significant non-specific signals (Lanes 3p, 4p, and 5p), but the corresponding AuNP-based assays (Lanes 3p′, 4p′ and 5p′) showed even greater specificity, in which the bands amplified from the longer telomerase extension products become substantially more abundant and extended. For example, in the presence of AuNPs, the detection of as few as 10 HeLa cancer cells gave a very clean gel image showing a ladder of specific bands (Lane 5p′) longer than the products of the traditional assay (Lane

5p). Human telomerase is modestly processive *in vitro*, and with shorter telomerase products accumulating, the longer telomerase extension products generally are less in quantity than the shorter ones by gel analysis[31]. As the outcomes of the assay can be influenced by both of the two reaction stages (the telomerase extension at 30 °C and the nucleic acid amplifications at 55 °C), the enhanced amplifications of longer telomerase extension products may be the result of two possibilities: the AuNP-based assays become more sensitive for the detection of template in low quantities or the telomerase processivity is enhanced by the addition of AuNPs.

2.2.3 Two-Step EXPIATR-AuNP to determine efficacy of the AuNPs

EXPIATR is a one-pot assay that has two reaction stages: the telomerase extension at 30 °C and the nucleic acid amplifications at 55 °C, which can run sequentially in a closed-tube and not affect each other (the one-step protocol). As both stages would affect the final results of the assay, it is necessary to further study which stage of the assay is actually influenced by the cell lysates and AuNPs. For this purpose, an independent telomerization step was performed by incubating the cancer cell extracts with dNTPs and NTS primers at 30 °C, and then heat-inactivating telomerase from the cell extracts at 85 °C; subsequently the telomerase extension products were used as targets, directly or doped in a high concentration of foreign cell lysates (from 4000 normal cells), to run the amplification reactions (the two-step protocol). Figure 2.9b shows by the two-step protocol the detections on extracts of 200 HeLa cancer cells, pure and in the presence of concentrated cell lysates (equivalent to 4000 normal cells); although not associated with the telomerization process, the cell lysates still induced negative effects to the amplification process, which could also be improved by the addition of AuNPs. All were similar to the results of using the one-step protocol (Figure 2.9a). It proved that the inhibitory effect of

cell lysates and the enhancing-effect of AuNPs were more related to the enzymatic nucleic acid amplification process rather than the telomerization process.

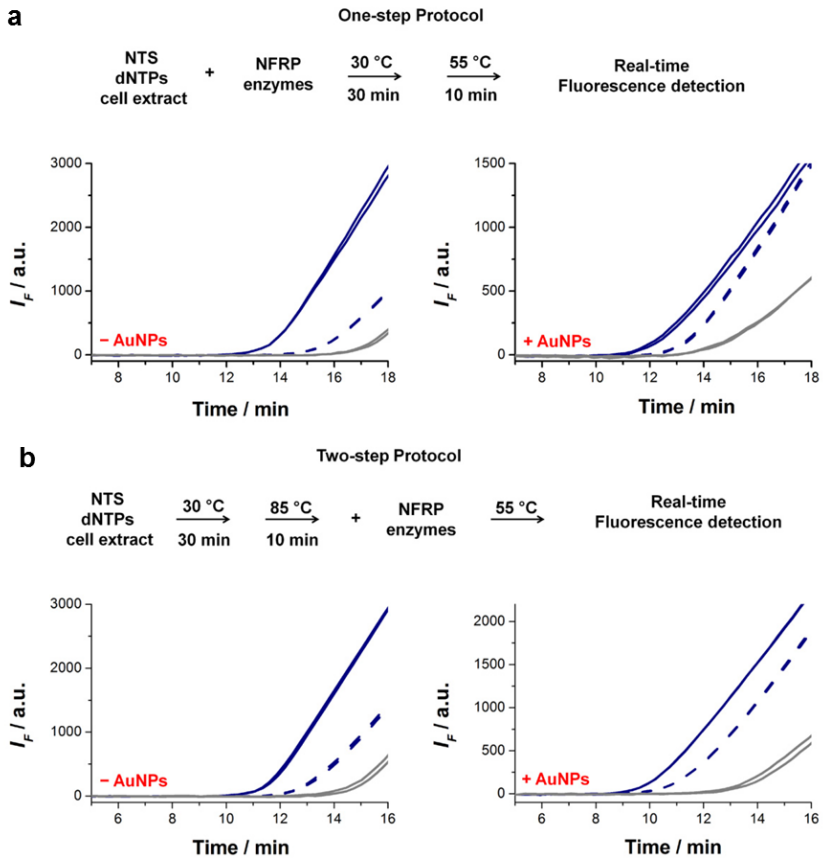

Figure 2.9 Comparison of the one-step and two-step protocols of EXPIATR and EXPIATR-AuNP assay The EXPIATR assay and the EXPIATR-AuNP assay tested on extracts of HeLa cancer cells (equivalent to 200 cells), pure (solid navy) and in presence of a high concentration of cell lysates (equivalent to 4000 normal cells) (dashed navy), were performed by the traditional one-step protocol (a) or modified two-step protocol (b) respectively; the corresponding non-template controls (grey) were also presented.

As a result, it was revealed that the addition of AuNPs could improve the sensitivity of the amplification reactions in the assay. From the detections of the complex samples containing 1000 normal cells, we found the inhibition effect of cell lysates was fully eliminated in the AuNP-based assays. In the presence of AuNPs, the amplified products of the complex samples containing 1000 foreign cells (Figure 2.8 Lanes 1c′ and 2c′) displayed almost identical gel patterns with those of the

pure cancer cells (Figure 2.8 Lanes 1p′ and 2p′), both of which showed enhanced amplifications of the longer telomerase extension products as compared with the traditional assays performed on the same amount of pure cancer cells (Figure 2.8 Lanes 1p and 2p). The combination of these two studies demonstrate that, more than simply overcoming the inhibition caused by the enriched cell lysates, the addition of AuNPs enhances the specificity of the assays to a new level. When the detections of complex samples containing 4000 normal cells were investigated, the EXPIATR-AuNP assays also showed improved specificity compared with the traditional assay (Figure 2.8 Lane 3c′ *vs.* 3c, 4c′ *vs.* 4c, and 5c′ *vs.* 5c), though the AuNP effects became less significant. This is accordant to the real-time results, *i.e.* with the addition of AuNPs the sensitivities of the assays performed on complex samples containing 4000 normal cells were improved but could not reach the same level as the detections on the pure cancer cells. These results are due to the poor specificity of the assays induced by concentrated lysates from 4000 normal cells. From the gel images of the negative controls, we learned that the non-specific reactions that occurred in the presence of and in the absence of 4000 foreign cells (Figure 2.8 Lane 6c and Lane 6p) produced different gel shift patterns, indicating that the outcome of the non-specific reaction would be affected by the enrichment of cell lysates. By the addition of AuNPs in the case absent of cell lysates, the non-specifically amplified products were significantly reduced (Figure 2.8 Lane 6p *vs.* 6p′), which is in agreement with the results of the detections on pure cancer cells and on the complex samples containing foreign normal cells at relatively low concentrations; while in the presence of a high concentration of normal cell lysates, the suppression effect of AuNPs against the non-specific reactions appeared less significant (Figure 2.8 Lane 6c *vs.* 6c′).

Finally for all the assays, we found several faint high molecular-weight bands generated at the same positions, which cannot be simply explained by the primer-based non-specific products due to

their high molecular weights. These faint bands were believed to come from the DNA-independent non-specific synthesis conducted by the polymerase and nicking enzyme, which will be discussed in detail later. Taken together, the gel analysis revealed that the presence of concentrated cell lysates in the complex samples inhibited the specific amplifications and caused more non-specific reactions; while the addition of AuNPs would improve the sensitivity and specificity of the amplification reactions. These results inspired us to investigate in depth the role of AuNPs in the general process of the isothermal enzymatic amplifications, rather than limit the study to the EXPIATR assay.

2.2.4 The role of AuNPs in suppressing the non-specific reactions

To study the role of AuNPs in the process of nucleic acid amplifications, their effect on the non-specific reactions was examined first. The isothermal enzymatic amplification reaction used in the EXPIATR assay is a typical NE-SDA reaction using two enzymes, the *Bst* 2.0 Warmstart polymerase and the Nt.BspQI nicking endonuclease (NEase). According to previous reports, NE-SDA reactions might be accompanied by non-specific reactions of both the primer artifacts and DNA-independent synthesis from the enzymes[3]. The primer artifacts are non-specifically synthesized from the primer mismatches, which generally exist both in PCR and other NAA methods. The other non-specific reaction is DNA-independent synthesis, which produces new DNA strands from dNTPs only by enzymes (the thermophilic polymerase and the NEase) without any templating or priming DNA strands, also called RE-pol DNA synthesis. Figure 2.10 shows the non-specific reactions occurred at two extreme conditions, *i.e.* Lanes 1a and 1b were performed in the NEB3 buffer (the recommended buffer for the Nt.BspQI NEase), and Lanes 2a–2c were run in the isothermal amplification buffer (IA buffer, the recommended buffer for the *Bst* 2.0 polymerase). To study the DNA-independent non-specific reactions from the enzymes: Lanes 1a and 2a were run only in the presence of two enzymes and dNTPs (without any DNAs) in respective buffers. From the gel, we observed that the quick DNA-

independent RE-pol synthesis occurred solely in the IA buffer (Lane 2a), and none was observed in the NEB3 buffer (Lane 1a). Second, in the presence of primers but no template, the non-template reactions were examined. Lane 1b with the NEB3 buffer showed the "primer-dimer" products only. Lane 2b with the IA buffer also showed the "primer-dimer" products, which had replaced the DNA-independent RE-pol synthesis, indicating the primer-related non-specific reactions are more favorable; however, certain faint bands were still produced at the position where the products of RE-pol synthesis would concentrate, indicating that a very small amount of RE-pol DNA synthesis still accompanied the primer-related reactions. Similar faint bands were also found in Figure 2.8, suggesting the ubiquitous presence of the RE-pol DNA synthesis in NE-SDA reactions. When a high concentration of cell lysates (equivalent to 4000 normal cells) was added to the non-template reaction in the IA buffer, Lane 2c showed that the RE-pol DNA synthesis became more significant (compared with the Lane 2b in absence of cell lysates). Finally, the influences of AuNPs on these non-specific reactions were explored. Lanes 2a′, 2b′, and 2c′ correspond to reactions of Lanes 2a, 2b, and 2c in the presence of AuNPs. In the absence of concentrated cell lysates, the addition of AuNPs reduced the non-specific reactions for both the amplified primer artifacts (Lane 2b′) and the RE-pol DNA synthesis (Lane 2a′); while for the condition enriched with cell lysates, AuNPs only marginally affected the primer-artifact amplifications but significantly reduced the RE-pol DNA synthesis (Lane 2c′). These observations were in accordance with the data presented in Figure 2.8, except that the RE-pol DNA synthesis became more significant in the IA buffer. Thus, the suppressing effect of AuNPs on the non-specific reactions, especially on RE-pol DNA synthesis, has been more elucidated.

Furthermore, we used the TPC8 template (the synthetic DNA target with eight telomere repeats which will produce six laddered main products by the NE-SDA reaction) to examine the influence of AuNPs on the specific amplification reactions. One reason for using the TPC8 template is to exclude

the telomerization step and study the AuNP effect on the NE-SDA reaction in a general way. Additionally, we can run the amplifications over a wider range of target concentrations to collect more information.

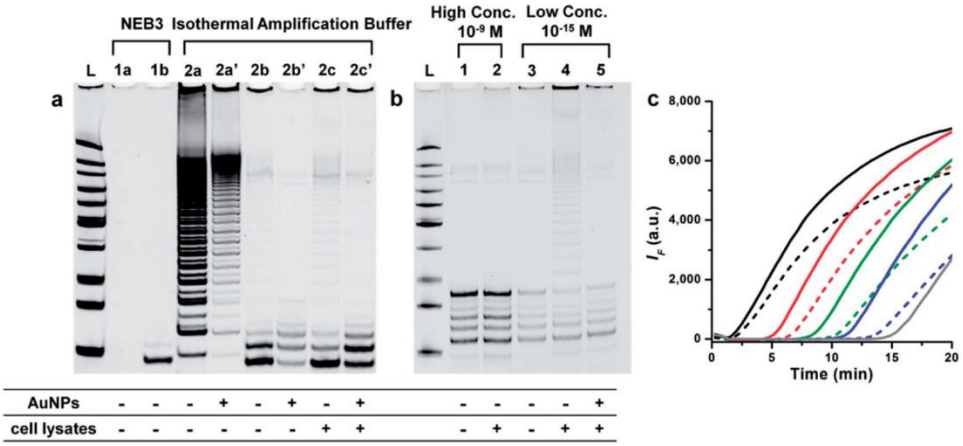

Figure 2.10 Analysis of the influence of AuNPs on the NE-SDA reactions (a) Native-PAGE analysis of the non-specific reactions happened in NEB3 buffer and in isothermal amplification buffer: Lane 1a, Lane 2a, and Lane 2a′ were DNA-independent synthesis; Lane 1b, Lane 2b, and Lane 2b′ were non-template reactions; Lane 2c and 2c′ were non-template reactions happened in the environment of a high concentration of cell lysates; (b) PAGE analysis of the specific reactions of the TPC8 template at different concentrations; (c) the real-time amplification curves corresponding to different concentrations of TPC8, pure (solid) and in the presence of a high concentration of cell lysates (dashed): 1×10^{-9} M (black), 1×10^{-11} M (red), 1×10^{-13} M (green), 1×10^{-15} M (blue), and negative control in the absence of TPC8 (grey).

Figure 2.10b shows PAGE analysis of the specific products amplified from the TPC8 template at two different concentrations (all run in the IA buffer), one high concentration of 10^{-9} M and one low concentration of 10^{-15} M. In the case that a massive amount of TPC8 template (1×10^{-9} M) was targeted, very specifically amplified products were observed regardless of whether it was in the presence of cell lysates (Lane 1 and Lane 2); on the contrary, when a low concentration of TPC8 template (1×10^{-15} M) was amplified, the reaction in the presence of cell lysates (Lane 4) produced very clear non-specific signals of RE-pol DNA synthesis while the corresponding reaction absent of cell lysates did not (Lane 3). With the addition of AuNPs, the non-specific bands induced by cell lysates could be efficiently diminished as shown in Lane 5. This experiment further demonstrated

AuNPs could improve the low-specificity of the nucleic-acid-amplification reactions caused by the presence of concentrated cell lysates.

As revealed by the studies on the real-time amplifications of TPC8, we observed the cell lysates caused the inhibition of the amplification reactions in a target-concentration-dependent manner. Figure 2.10c shows the amplifications with the concentrations of TPC8 ranging from 1×10^{-9} M to 1×10^{-15} M, in the absence of (solid lines) and in the presence of a high concentration of cell lysates (equivalent to 4000 cells in each test) (dashed lines). As the TPC8 template concentration decreased, the inhibitory effect of the cell lysates to the amplification reactions became more apparent. The presence of cell lysates hardly affected the amplification of TPC8 when a high concentration was present, which implies that the main inhibitors from the cell lysates affected the amplification reaction by impairing the templates more than the enzymes.

2.2.5 Mechanism of low-specificity due to cell lysate interference

As cellular proteins, which are prone to binding with DNA templates and making them unavailable for polymerases[32-33], are believed to be essential inhibitors to NAA methods, we treated the normal cell lysates with proteinase K prior to the amplification process. Tan et al. carefully studied the possible nonspecific reactions for the nicking-enzyme-mediated SDA (NE-SDA) reactions[3]. They found that the non-specific reactions included an "early phase" related to primer-dimer like artifacts and a "late phase" in general agreement with the literature reports of RE-pol (restriction-endonuclease-polymerase) DNA synthesis. The RE-pol DNA synthesis is a kind of DNA-independent synthesis, which would produce new DNA strands from dNTPs only by enzymes (both the thermophilic polymerase and the NEase) in the absence of any templating or priming DNA strands. The primer/template-independent RE-pol DNA synthesis has been observed in many isothermal amplifications working upon various combinations of polymerases and NEases.

To further understand the RE-pol DNA synthesis, we did several control experiments. Based on the findings presented in Figure 2.11a, the following conclusions were obtained: (1) In the absence of dNTPs, the *Bst* polymerase and the Nt.BspQI NEase with (lane 2) or without (lane 3) heating at 55 °C could not induce RE-pol DNA synthesis. The results are in accordance with the previous reports for RE-pol DNA synthesis in which the non-specific DNA sequences were synthesized from dNTPs by the enzymes. (2) Also in the absence of Nt.BspQI NEase (lane 4) or *Bst* polymerase (lane 5), no RE-pol DNA synthesis took place. (3) Furthermore, we checked that if the cell lysates could induce some additional RE-pol DNA synthesis. For itself (lane 6), combined with *Bst* polymerase (lane 7) or Nt.BspQI NEase (lane 8), cell lysates from 4000 normal cells could not synthesize DNA sequences from dNTPs, indicating the cell lysates could not induce more RE-pol DNA synthesis in the reaction system.

As a further study, we treated the cell lysates in different ways to reveal which component in the cell lysates would cause the RE-pol DNA synthesis (Figure 2.11b). The non-template reactions only in presence of primers but no template were run in the un-optimal IA buffer to emphasize the non-specific signals. In the presence of un-treated cell extracts equivalent to 4000 normal MRC-5 cells, both non-specific reactions of the primer-dimer like artifacts and the RE-pol DNA synthesis were observed on the gel (lane 2). Firstly, we pre-incubated the cell extracts with DNase I at 37 °C for 30 min, inactivated the DNase I at 75 °C for 10 min, and then added the treated cell extracts to the non-template amplification reaction (lane 6), at which condition the RE-pol DNA synthesis was still observed as part of the non-specific reactions. The same result was observed when the cell extracts were pre-incubated with RNase (lane 7). Further, the cell extracts were pretreated with proteinase K to degrade proteins by cleaving peptide bonds and catalyzing peptide amide hydrolysis, and then the proteinase K was heat-inactivated at 95 °C

prior to mixing the treated cell extracts with the non-template reaction. Interestingly, under this condition (lane 3), the RE-pol DNA synthesis was eliminated from the non-specific reactions, and only the primer-artifacts non-specific reactions remained. Lane 4 shows a control experiment in which the cell extracts underwent the same incubation process as lane 3 but without the addition of proteinase K. In this control condition without the addition of proteinase K, the RE-pol DNA synthesis occurred again, verifying the function of proteinase K but not the incubation process was essential to depress the RE-pol DNA synthesis. Due to the truth that proteinase K cannot be completely inactivated even at 95 °C, proteinase K might cause the inactivation of *Bst* polymerase and as a result depress the RE-pol DNA synthesis. Therefore, in another control experiment (lane 5), a new portion of untreated cell lysates was added to the reaction of lane 3. Under this condition, the RE-pol DNA synthesis occurred as part of the non-specific reactions, indicating that the *Bst* polymerase was not badly affected (not totally inactivated) by the presence of proteinase K.

As a result, we found that the elimination of cellular proteins from the cell lysates recovered the specificity of the amplification system. It demonstrated that the cellular proteins were essential for inhibiting the specific amplification and facilitating the RE-pol DNA synthesis. Waleed et al. reported that proteins, like on the basis of N-terminal amino acid sequences, were prone to bind with ssDNAs and acted as inhibitors to PCR by making the DNA templates unavailable for the polymerase[33]. Combined with our observations that the inhibition effect caused by cell lysates was more significant for the amplifications of low-abundant templates, we assumed that the cellular proteins might bind with ssDNAs and make the templates unavailable for polymerase. As a result, like a competition, the specific reaction was attenuated and the DNA-independent RE-pol DNA synthesis would be boosted at the same time.

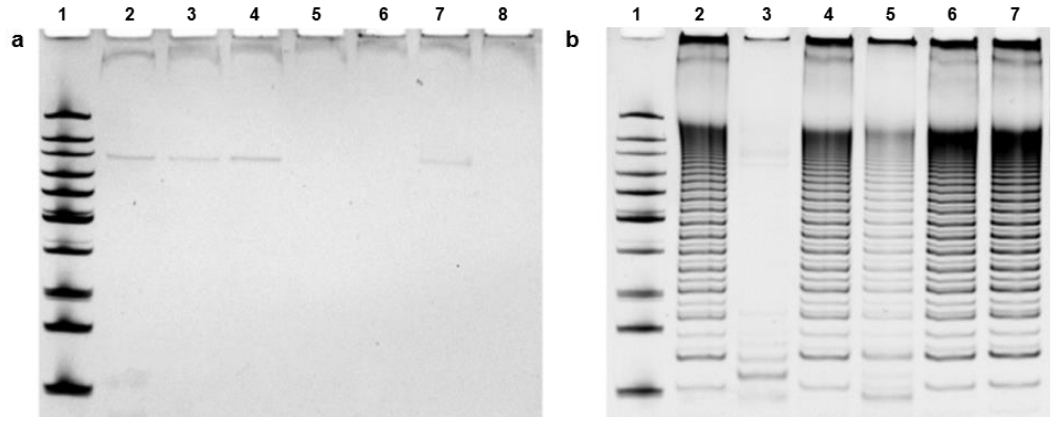

Figure 2.11 PAGE analysis to determine different sources of RE-pol synthesis and non-template reactions (a) The survey of the essentials for producing a RE-pol DNA synthesis: DNA ladder (lane 1), *Bst* polymerase + Nt.BspQI without heating (lane 2), *Bst* polymerase + Nt.BspQI (lane 3), *Bst* polymerase + dNTPs (lane 4), Nt.BspQI + dNTPs (lane 5), cell lysates + dNTPs (lane 6), cell lysates + *Bst* polymerase + dNTPs (lane 7), and cell lysates + Nt.BspQI + dNTPs (lane 8); the reactions in Lane 3 – Lane 8 were heated at 55 °C for 15 min prior to the gel characterizations; (b) The cell lysates with some pretreatments and their influences to the non-template reactions (in the IA buffer): DNA ladder (Lane 1), the non-template reactions in presence of: cell lysates without any treatment (lane 2), cell lysates with proteinase K treatment (lane 3) and its two control experiments (Lane 4 and Lane 5), cell lysates with DNase treatment (lane 6), and cell lysates with RNase treatment (lane 7).

As it has been proven that AuNPs could enhance the low-specificity caused by the cell lysates, we examined whether the AuNPs work by removing the interference of cell lysates and as a result improve the reaction specificity indirectly, or rather the AuNPs work by enhancing the specificity of the amplification reaction in a fundamental way. The amplification reactions run using the wild-type *Bst* polymerase showed worse specificity than that by *Bst* 2.0 Warmstart polymerase. As shown in Figure 2.12a, the amplification reactions using wild-type *Bst* polymerase intrinsically presented lower specificity. The amplification curves irregularly correlated with the starting concentrations of template (100-fold dilution series from 10^{-9} M to 10^{-15} M); also some of the reactions showed poor reproducibility, *i.e.* the amplifications of templates at low concentrations were partially or completely inhibited. Studied by gel electrophoresis, the amplifications of 10^{-9} M TPC8 (Lane 1), 10^{-13} M TPC8 (Lane 2) and non-template control (Lane 3) were visualized. The image indicated that the specific

amplifications were interfered by the non-specific reactions; the amplifications of 10^{-13} M TPC8 and non-template control were especially overwhelmed by the RE-pol DNA synthesis. The fluorescent probe used in this NE-SDA reaction is also acting as a primer, which is in a hairpin structure and modified with both a fluorophore and a quencher. This probe-primer would only release fluorescence signals in the specific reactions and the "primer-dimer" non-specific reactions, but not in the RE-pol DNA synthesis because it is a DNA-independent reaction. As a result, when the RE-pol DNA synthesis overwhelmed the specific amplification in the case of low specificity, the fluorescence signals were inhibited. Accordingly, if probed by the SYBR Green I dye (a non-specific probe that will bind to any random dsDNA sequences) instead, only the amplifications of 10^{-9} M and 10^{-11} M TPC8 could be distinguished from the non-template control, while the other amplification curves fell together (data not shown), since the products of RE-pol DNA synthesis could also probed by SYBR Green I dye. With the addition of AuNPs, the specificity of the amplification reactions conducted by the wild-type *Bst* polymerase could be significantly improved.

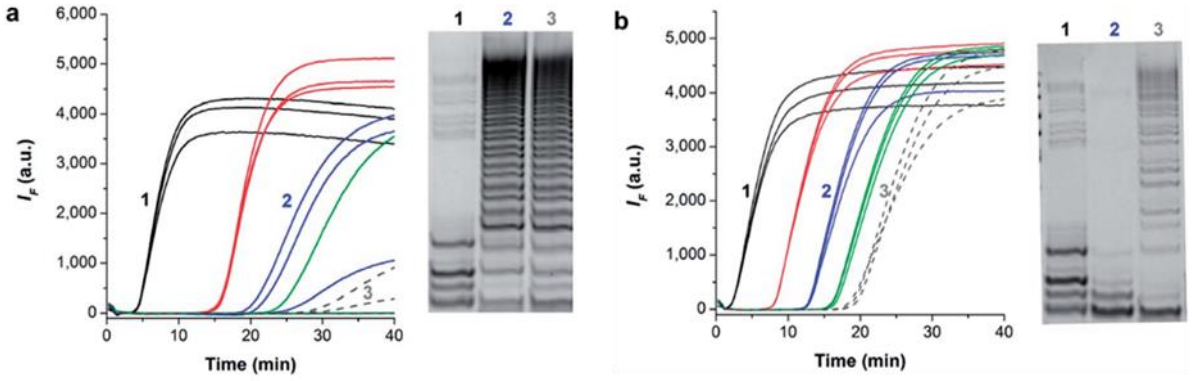

Figure 2.12 The amplifications run by using the wild type *Bst* polymerase Different concentrations of TPC8 in the absence (a) and in the presence (b) of AuNPs: 1×10^{-9} M (black), 1×10^{-11} M (red), 1×10^{-13} M (blue), 1×10^{-15} M (green), and non-template control (gray); the gel images on the right corresponding to the products of the amplifications that were labelled with the same number.

As shown in Figure 2.12b, the amplification curves evenly distribute along the concentrations of template (from 10^{-9} M to 10^{-15} M). Furthermore, by the gel characterizations, we could see the non-

specific RE-pol DNA synthesis had been greatly suppressed by the addition of AuNPs. In this example, even without cell lysates involved, the AuNPs could also suppress the non-specific reactions, and as a result, improve the specificity of the reactions, which indicated that the "AuNP effects" did not simply work only on cellular proteins but fundamentally on improving the amplification reactions. The NEase enzymes used in the isothermal NE-SDA reaction will accelerate and intensify the non-specific reaction of the polymerase. As a result, in addition to the enhancing-effect of AuNPs on the specific amplifications, we further observed the suppressing effect of AuNPs on the non-specific reactions. Also, by studying the AuNP effect on an intrinsically low-specificity system caused by the less specific polymerase, we believe that AuNPs have the power to enhance and reform the NE-SDA reactions in a very fundamental way.

2.2.6 The interactions between AuNPs and the reaction components

As 10nm AuNPs exhibit a characteristic surface plasmon band at ~520 nm, which is sensitive to the local environment of gold surface, UV-Vis spectroscopy is a powerful means to study the interaction between AuNPs and other biomolecules[34]. As seen in Figure 2.13a, the UV-Vis absorption spectrum of the AuNPs solution dispersed in water displayed the typical plasmon peak at 514 nm (curve 1). If diluted by the reaction buffer (curve 2), the AuNPs themselves showed a red-shifted absorption at 610 nm, indicating an aggregated state; while in the presence of DNA reactants (primers, templates and dNTPs), the AuNPs showed absorption back to 514 nm (curve 3), changing its status from aggregation to colloidal dispersion state. According to previous studies, citrate-capped AuNPs are stabilized by electrostatic repulsion. The high salt concentration in the amplification buffer will screen the repulsive interactions and cause colloid aggregation; while the ssDNAs will adsorb on the gold surface through favorable interactions between the bases and gold, making the AuNP surface

more negatively charged and resistant to the bulk ionic strength induced by the buffer, and as a result, stabilize the particles against aggregation[35].

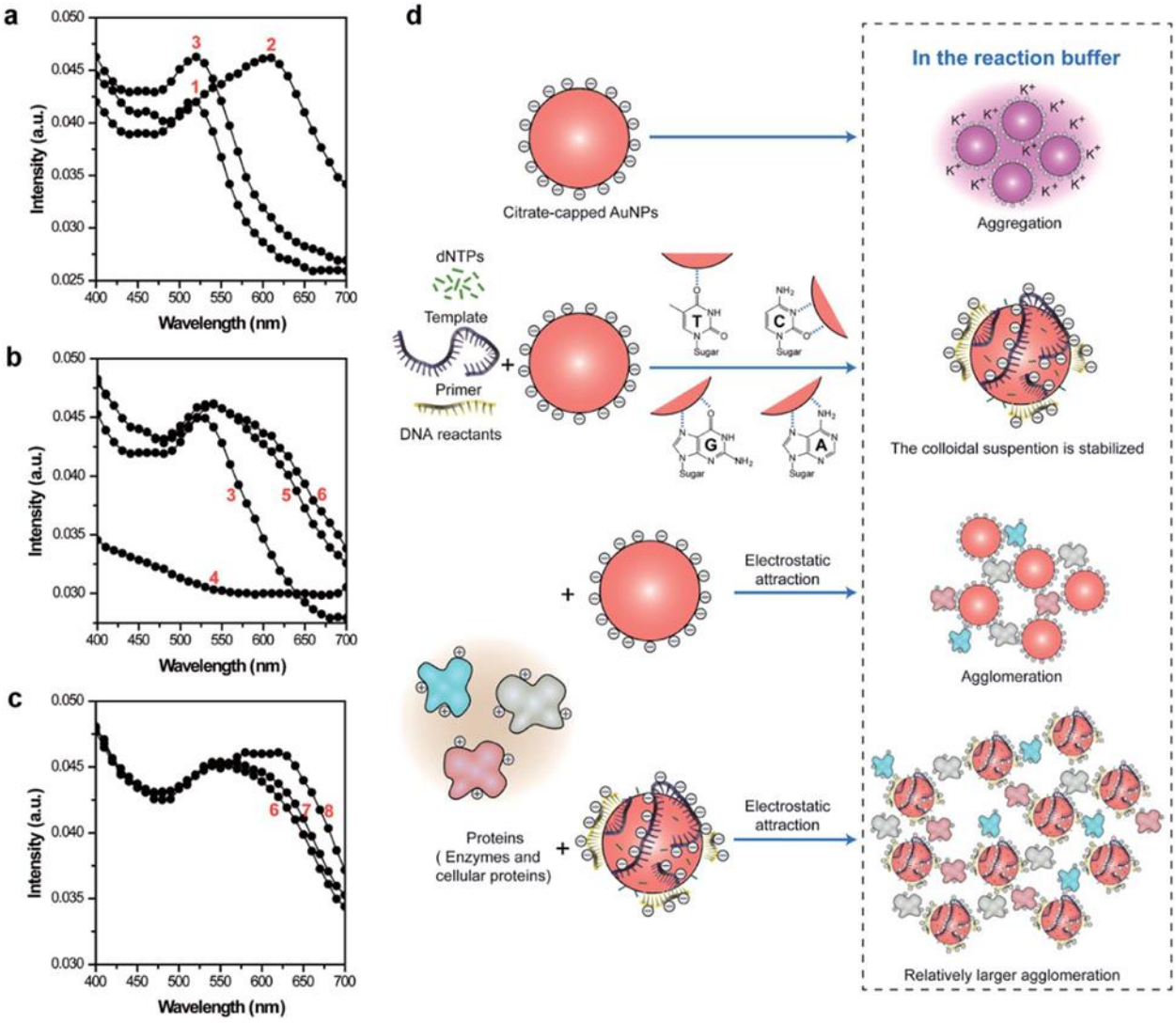

Figure 2.13 UV-Vis spectroscopic analysis of the interactions between AuNPs and the reaction components (a) Diluted water solution of AuNPs (curve 1), AuNPs in the reaction buffer (curve 2), and AuNPs in the reaction buffer mixed with DNA reactants (curve 3); (b) a reaction mixture without AuNPs (curve 4), a reaction mixture with AuNPs in the absence of enzymes (curve 3), a reaction mixture with AuNPs in the absence of DNA reactants (curve 5), and a full reaction mixture with AuNPs (curve 6); (c) a full reaction mixture with AuNPs (curve 6), a full reaction mixture with AuNPs in the presence a high concentration of cell lysates (curve 7), and a reaction mixture in the presence of AuNPs and with the enzymes replaced by a high concentration of cell lysates (curve 8); (d) schematics illustrating the interactions between AuNPs and the reaction components.

The interactions between AuNPs and the reaction components were further studied using the one-by-one method as shown in Figure 2.13b, *i.e.* the interactions of AuNPs with the components of the reaction mixture were studied gradually. (1) When AuNPs were absent in the reaction mixture (curve 4), no significant absorption could be observed. (2) When reactant enzymes (*Bst* 2.0 WarmStart polymerase and Nt.BspQI NEase) were eliminated from the reaction mixture (curve 3), as discussed above, the ssDNAs would stabilize the AuNPs from aggregation and result in a dispersion state. (3) Alternatively, when DNA reactants were eliminated from the reaction mixture (curve 5), the absorption band of AuNPs became broader and showed a peak at 530 nm. The red-shift of the absorption under this condition was not as pronounced as that corresponding to the aggregation state and parts of the absorption still came from the un-aggregated state, indicating that the enzymes probably induced agglomeration of the AuNPs rather than aggregation[36-38]. When all the reactants were involved (curve 6), a further red-shifted and broader absorption was observed compared with the agglomeration state induced by the enzymes alone. It indicated that the enzymes might not remove the citrate ligands from the gold surface but rather form self-assemblies with the particles through electrostatic interactions between the positively charged amino groups of proteins and the negatively charged citrate groups[37]. Therefore, in the presence of DNA reactants, a higher charge density would be generated on the AuNP surface and enhance the electrostatic attraction to the enzymes; thus a more red-shifted absorption was observed when the reactant DNAs and enzymes coexisted in the system. Subsequently, the influences of cell lysates on the reaction system were studied as shown in Figure 2.13c. The absorption spectrum of AuNPs in the reaction mixture with cell lysates (curve 7) was very similar to that without cell lysates, except being a little broader. When the two enzymes were eliminated from the reaction mixture and replaced by cell lysates (curve 8), the resultant spectrum also showed a broad absorption band with a red-shifted peak; this indicates that cell lysates had similar

interactions with AuNPs to the enzymes, which is expected given that both are protein molecules. However, the red-shift of the absorption that the cell lysates induced was significant compared to that of the enzymes, suggesting the cell lysates might induce a different agglomeration state of AuNPs. Furthermore, we found that the absorption band of the reaction mixture in the presence of both the enzymes and the cell lysates (curve 7) fell between the absorptions of reaction mixtures containing solely the enzymes or solely the cell lysates (curve 6 and curve 8), but was more similar to that of the enzymes-only mixture (curve 6). This suggests that when both the enzymes and the cell lysates were added to the reaction mixture, AuNPs would show a stronger affinity to the enzymes than the cellular proteins. The proposed interactions of AuNPs with the components of the assay were illustrated in Figure 2.13d.

According to the results of the UV-Vis spectroscopic studies, we can understand more about the AuNP effect. First, since AuNPs have a uniform surface and strongly interact with all the reaction components, the addition of AuNPs could significantly change the distribution of reaction components in the amplification system, which may help us to understand how such a small amount of AuNPs could affect the specificity and sensitivity of the amplification reactions. Also, the strong interactions between AuNPs and the reaction components reveal why the concentration of AuNPs to be very critical, since a certain amount of AuNPs ($\leq$ 0.4 nM for this case) can enhance the specificity of the amplification reactions by raising the probability of dynamical contacts between templates and enzymes, but too many AuNPs will inhibit the reactions since the excessive binding of the enzymes to AuNPs would contrarily decrease activities of the enzymes[21]. Meanwhile, we found that 0.4 nM AuNPs also showed negligible quenching effect of the fluorescence probe (Figure 2.14), further indicating that it is a good concentration for the NE-SDA reactions.

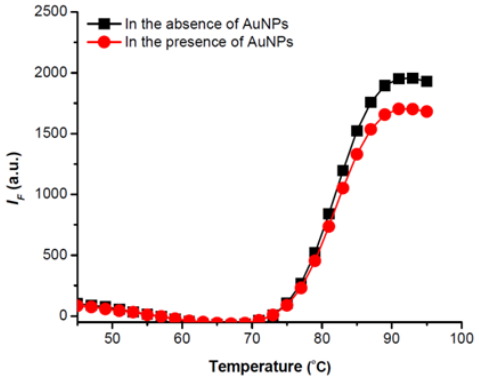

Figure 2.14 Effect of fluorescent-quenching by AuNPs Thermal denaturation profile of NFRP-primer fluorescence probe in the absence of AuNPs (black) and in the presence of AuNPs (red).

Last of all, the situation is more complicated for the EXPIATR assay performed on complex samples. The UV-Vis spectroscopic study revealed that the enzymes showed a stronger affinity to AuNPs compared with the cellular proteins of the cell lysates; however the presence of a high concentration of cellular proteins would still affect the effectiveness of AuNPs in enhancing the amplification reactions as they would occupy parts of the nanoparticle surfaces. Thus, on one hand, the cell lysates will counteract the effect of AuNPs, *i.e.* [AuNPs] $\leq$ 0.4 nM only marginally suppressed the primer-artifact amplification and showed noticeably less improvement in the specific amplification (as we discussed in Figure 2.8) in the assays performed on complex samples containing 4000 normal cells; on the other hand, the cell lysates will protect enzymes from excessive binding to AuNPs. As a result, the addition of more AuNPs (> 0.4 nM) would not immediately inhibit the specific reactions, but further diminish the influence from cell lysates of complex samples. Therefore, we examined when cell lysates were abundant in the reaction mixtures, and found that AuNPs only marginally suppressed the primer-artifact amplification and showed noticeably less improvements in the specific amplifications.

As shown in Figure 2.15, the non-template control in the absence of cell lysates was significantly inhibited when more than 0.4 nM AuNPs was added to the amplification system,

and the assay performed on the normal cell lysates (equivalent to 4000 MRC-5 cells), with a high abundance of cellular proteins, exhibited a higher amplification rate than the non-template control, resulting in the false-positive problem. The problem with the use of additional AuNPs is that the amplification in the presence of cell lysates would be benefited, because more AuNPs would overcome the influence of the cell lysates and maximize the effectiveness of the AuNPs to the amplification reactions. Meanwhile the cellular proteins would bind parts of the nanoparticle surfaces and protect the enzymes from excessive binding; while on the contrary, the amplification in the absence of cell lysates would be inhibited by the same amount of AuNPs as the excessive binding of the enzymes to AuNPs would contrarily decrease their activities[21].

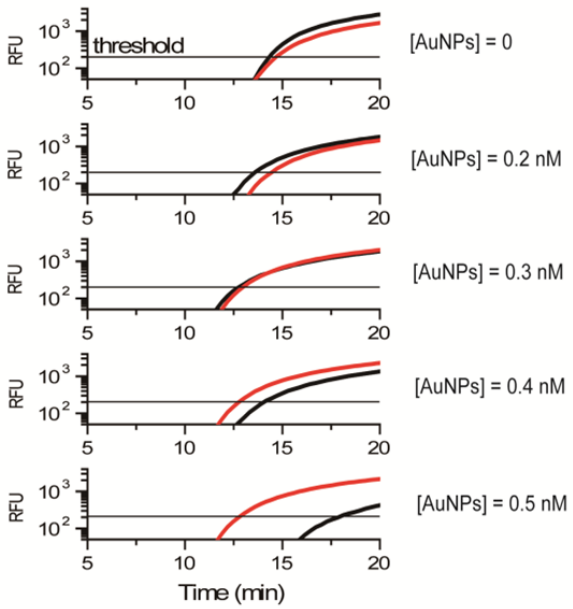

Figure 2.15 The concentration effect of 10 nm citrate-capped AuNPs for the EXPIATR-AuNP assay The non-template control in the absence of cell lysates (black) and the detection on normal cell lysates (equivalent to 4000 MRC-5 normal cells) (red).

Thus, considering removing the false-negative problem induced by cell lysates as much as possible and not inducing new false-positive problem, 0.4 nM AuNPs, a concentration showing negligible effect to the amplification in the absence of cell lysates, is optimized for the modified

EXPIATR-AuNP assay. Although the assay with 0.4 nM AuNPs could not achieve the maximum effect of AuNPs on eliminating the inhibition induced by 4000 foreign normal cells, the sensitivity of the detections of telomerase activity in complex samples was still significantly improved, over five-fold as compared with the traditional assay; at the same time, detections on normal cells could also accurately show negative telomerase activity.

2.2.7 Conclusion

We have concluded that that AuNPs are powerful additives to the isothermal NE-SDA reaction, which uses a strategy distinct from PCR. Also, regardless of the source of the low-specificity of the NE-SDA reaction, external (cell lysates in complex samples) or internal (low fidelity of the polymerase), AuNPs showed a similar power in improving the specificity of the reactions. These results imply that AuNPs improve the process of nucleic acid amplifications in a very fundamental way. It has been reported that nanomaterials (such as citrate-capped AuNPs, single-walled carbon nanotubes, and modified quantum dots) could enhance the structural stability and maintain the bioactivity of enzymes[39-42]. According to our observations, this is also the most likely mechanism of the AuNP effect in this study. There are some other possible mechanisms of the AuNP effects which may also explain some of our results. For example, it has been believed that the AuNPs may resemble the function of the single-strand-binding protein in the course of nucleic acid amplification[43], which selectively binds to ssDNA rather than dsDNA[44], and prevents the amplifications of primer mismatches. Moreover, by the UV-Vis spectroscopic study, we observed the "concentrating effect" of AuNPs[47], *i.e.* all the reaction components were attracted towards the charged nanoparticles. The aggregates of all the necessary components for the amplification reaction surround the AuNPs, resulting in many small reaction centers, raising the probability of dynamical contacts between

templates and enzymes, and thus, enhancing the sensitivity of the amplification of a low template quantity within a high concentration of background cell lysates.

In conclusion, our investigations demonstrated that AuNPs have powers in enhancing the specificity of isothermal nucleic acid amplification reactions. Such AuNP effects provide efficient ways to improve the detection sensitivity of the EXPIATR assay performed on complex samples containing enriched normal cell lysates; otherwise, enriched cell lysates would impair the specificity of nucleic acid reactions and cause troubles for the related assays in clinical applications. A proper concentration is important to appreciate the power of the AuNPs, which has to be carefully optimized to ensure the amount of AuNPs will not affect the amplification significantly in the absence of cell lysates. Given the importance of the strategy of using nicking enzymes and DNA polymerases to develop isothermal NAA methods, this study will be significant by providing an efficient method to enhance the reliability for related isothermal assays in clinical applications.

2.3 Experimental Section

2.3.1 Materials and instruments

All oligonucleotides were obtained from Integrated DNA Technologies. The deoxynucleotide solution mix, *Bst* 2.0 WarmStart DNA polymerase (8,000 units mL^{-1}), *Bst* polymerase large fragment (8,000 units mL^{-1}), nicking endonuclease Nt.BspQI (10,000 units mL^{-1}), deoxyribonuclease (DNase I) (RNase free, 2,000 units mL^{-1}), proteinase K (20 mg mL^{-1}), NEB3 buffer (10×), isothermal amplification buffer (10×), and quick-load low molecular weight DNA ladder were purchased from New England Biolabs Ltd.. SYBR Green I (10,000×) and SYBR Gold nucleic acid gel stain (10,000×) were obtained from Molecular Probes, Inc. Ribonuclease (RNase) (DNase-free) (0.5 μg μL^{-1}) was purchased from Roche Applied Science. Au colloids (10

nm) were purchased from Ted Pella, Inc. It should be noted that the unit activity of the Nt.BspQI NEase may vary between different lots; the specificity of the amplifications (especially the degree of RE-pol DNA synthesis) might vary from lot to lot. Therefore an optimization should be performed before using a new lot number and, in some bad conditions; an additional 20 mM NaCl will be required for the reaction buffer. Magnesium chloride ($MgCl_2$) solution (1 M), TWEEN 20, potassium chloride (KCl), ethylene glycol tetraacetic acid (EGTA), ethylenediaminetetraacetic acid (EDTA), trizma hydrochloride pH 7.5 and pH 8.3 were obtained from Sigma-Aldrich. TRAPeze® 1× CHAPS Lysis Buffer and TRAPeze® Telomerase Positive Control Cell Pellet (HeLa cancer cells) were purchased from Millipore. Cell pellets of MDA-MB-231, UM-UC-3, HCC-38, LAI-55n, and MRC-5 cell lines were kindly provided by Prof. Chuan He from The University of Chicago. 30% acrylamide and bis-acrylamide solution (19:1), ammonium persulfate (APS), tetramethylethylenediamine (TEMED), 5× nucleic acid sample loading buffer (premixed for non-denaturing TBE gels, pH 8.0) and 10× tris/boric acid/EDTA (TBE) buffer were purchased from Bio-Rad. Nanosep® centrifugal device with Omega membrane, MWCO 3kDa, was obtained from Pall Corporation. The water used in this paper was purified by BarnsteadTM Nanopure® Ultrapure Water Purification System.

All the assays were performed on the CFX96 touch real-time PCR detection system (Bio-Rad) using 0.2 mL low profile PCR tubes (white). Eppendorf centrifuge model 5430R and thermomixer® R dry block heating and cooling shaker were used. The polyacrylamide gel electrophoresis (PAGE) was run on a PROTEIN II xi cell system (Bio- Rad) using the PowerPac HV as power supply (Bio-Rad) and the gels were visualized using the Gel Doc XR+ imaging system (Bio-Rad). The UV-Vis spectra were monitored by using Synergy H4 Hybrid multi-well Plate Reader (BioTek).

2.3.2 The assay protocol

A traditional amplification reaction (20 μL) contains variable amounts of cell extract/TPC8 (the synthetic template with eight telomeric repeats used as a positive control), the nicking telomerase substrate (NTS) primer and the nicking fluorescent reporter probe (NFRP) primer (100 nM each), Tris-HCl (30 mM, pH 8.3), MgCl2 (1.5 mM), KCl (100 mM), EGTA (1 mM), Tween 20 (0.05%, vol/vol), dNTPs (200 μM each), *Bst* 2.0 WarmStart DNA polymerase (0.96 units) and Nt.BspQI NEase (5 units). Typically, the stock solution of NFRP primers (4 μM) in tris-HCl buffer (pH 7.5, 10 mM) was incubated at 90 °C for 2 min and then allowed to cool slowly to room temperature to form the hairpin structures. A master mix containing everything but cell extract/TPC8 template was assembled first on ice; Aliquoted 19 μL of the master mix into each PCR tube, added cell extract/TPC8 (1 μL) with different concentrations into corresponding tubes, and mixed well before the test. The assay was performed with incubations lasting 10-30 min at 30 °C (for telomerase extension) before initiating the DNA amplifications at 55 °C. The assays were monitored by real-time fluorescence at an interval of 10 s. Following the amplification reaction, each 20 μL reaction was mixed with 5 μL loading buffer on ice and 10 μL of the mixture was analyzed by electrophoresis in 0.5× TBE buffer on a 12% polyacrylamide native gel (1.5 h, 17 V cm^{-1}). After electrophoresis, the gel was stained in 1× SYBR Gold (in TE buffer) for 30 min, washed by pure water and visualized by the gel imager.

2.3.3 Preparation of cell extracts

All the cells were stored as pellets at -80 °C until extraction. Each cell pellet (containing one million cells) was suspended in 200 μL CHAPS lysis buffer, incubated on ice for 30 min and then centrifuged at 12,000 *g* for 20 min at 4 °C. After centrifugation, 160 μL of the supernatant was transferred into a fresh tube and a series of diluted solutions in CHAPS lysis buffer were

quickly prepared, flash-frozen, and stored at -80 °C before use. The complex, protein-rich samples comprise cancer cell extracts (various concentrations equivalent to 10 cells μL^{-1} – 200 cells μL^{-1}) and a high concentration of cell lysates of foreign normal cells (MRC-5, 4,000 cells μL^{-1} or 1,000 cells μL^{-1}), which were prepared by doping certain amounts of cancer cell extracts into normal cell extracts; the concentrations of cancer cell extracts in the complex sample and its corresponding pure sample were kept the same.

2.3.4 The traditional EXPIATR assay

The principle of the EXPIATR assay is illustrated in Figure 2.1. It is a method based on a system of two primers, the NTS primer and the NFRP primer, and three enzymes, *Bst* 2.0 WarmStart DNA polymerase, Nt.BspQI NEase, and telomerase extracted from crude cancer cells. The NTS primer contains a non-telomeric sequence (black color) which telomerase can recognize as a substrate, and the NFRP primer, in a hairpin structure, carries a single-stranded (ss) DNA tail (brown color) which can bind to the telomeric repeat sequence. Through incorporation of the Nt.BspQI recognition sequence (red color) in both primers, the DNA amplification can be performed at a fixed temperature via the activity of the Nt.BspQI NEase to cut one strand of a double-stranded (ds) DNA at the recognition site, and the ability of the *Bst* 2.0 polymerase to extend the 3’ end at the nick and displace the downstream strand. In the presence of telomerase, a minor number of NTS primers are converted to telomerase extension products (telomeric repeats are synthesized onto the 3’ ends of NTS primers), which will act as templates for the following DNA amplification process. The hybridization between the extended NTS telomeric template and the NFRP primer initiates polymerization, resulting in the formation of double-stranded recognition sites for Nt.BspQI NEase. After the NEase cleaves the primer strands, further polymerization proceeds continually from the nick and displaces the previously

copied strands. In the first stage, duplex I forms from the telomerase extension products, after which the DNA reaction is repeated in both directions, continuously releasing strands T1 and T2. In the next stage, as NTS and NFRP primers are present in excess, strands T1 and T2 can further hybridize with the free NTS and NFRP primers respectively, forming duplexes II and III which allow the DNA reactions to occur in a single direction. The cycling reaction between II and III finally results in the exponential amplification of telomerase products, in which strands displaced from duplex II (same as T1) serve as targets for the NTS primer (to form the new duplex III), while strands displaced from duplex III (same as T2) serve as targets for the NFRP primer (to form the new duplex II). As the NFRP primer can bind multiple positions along the templates, according to the number of the telomeric repeats extended on the NTS primers, the amplification reaction yields a series of lengths of duplex II and duplex III (which have the identical lengths). At the final stage, when the NTS and NFRP primers become limiting, the further nicked duplex IV (T1•T2) starts to accumulate in the reaction, which will be 18 bps shorter than duplex II and duplex III. The sequences of the oligomers are as follows:

NFRP: (/5IABkFQ/AGC AGG AAG CGC TCT TCC TGC /iFluorT/CC CTA ACC CTA ACC C) /5IABkFQ/ = 5' Iowa Black® FQ; /iFluorT/ = Int Fluorescein dT.

NTS: (GTG CGT GAG AGC TCT TCC AAT CCG TCG AGC AGA GTT)

TPC8: (GTG CGT GAG AGC TCT TCC AAT CCG TCG AGC AGA GTT AGG GTT AGG GTT AGG GTT AGG GTT AGG GTT AGG GTT AGG G)

2.4 References

1. Walker, G. T.; Fraiser, M. S.; Schram, J. L.; Little, M. C.; Nadeau, J. G.; Malinowski, D. P., Strand displacement amplification--an isothermal, in vitro DNA amplification technique. *Nucleic Acids Research* **1992,** *20* (7), 1691-1696.

2. Weizmann, Y.; Beissenhirtz, M. K.; Cheglakov, Z.; Nowarski, R.; Kotler, M.; Willner, I., A virus spotlighted by an autonomous DNA machine. *Angew Chem Int Ed Engl* **2006,** *45* (44), 7384-8.

3. Tan, E.; Erwin, B.; Dames, S.; Ferguson, T.; Buechel, M.; Irvine, B.; Voelkerding, K.; Niemz, A., Specific versus nonspecific isothermal DNA amplification through thermophilic polymerase and nicking enzyme activities. *Biochemistry* **2008,** *47* (38), 9987-99.

4. Connolly, A. R.; Trau, M., Isothermal detection of DNA by beacon-assisted detection amplification. *Angew Chem Int Ed Engl* **2010,** *49* (15), 2720-3.

5. Duan, R.; Zuo, X.; Wang, S.; Quan, X.; Chen, D.; Chen, Z.; Jiang, L.; Fan, C.; Xia, F., Quadratic isothermal amplification for the detection of microRNA. *Nat Protoc* **2014,** *9* (3), 597-607.

6. Tian, L.; Weizmann, Y., Real-time detection of telomerase activity using the exponential isothermal amplification of telomere repeat assay. *J Am Chem Soc* **2013,** *135* (5), 1661-4.

7. Kim, N. W.; Piatyszek, M. A.; Prowse, K. R.; Harley, C. B.; West, M. D.; Ho, P. L.; Coviello, G. M.; Wright, W. E.; Weinrich, S. L.; Shay, J. W., Specific association of human telomerase activity with immortal cells and cancer. *Science* **1994,** *266* (5193), 2011-5.

8. Zheng, G.; Patolsky, F.; Cui, Y.; Wang, W. U.; Lieber, C. M., Multiplexed electrical detection of cancer markers with nanowire sensor arrays. *Nat Biotechnol* **2005,** *23* (10), 1294-301.

9. Xiao, Y.; Dane, K. Y.; Uzawa, T.; Csordas, A.; Qian, J.; Soh, H. T.; Daugherty, P. S.; Lagally, E. T.; Heeger, A. J.; Plaxco, K. W., Detection of telomerase activity in high concentration of cell lysates using primer-modified gold nanoparticles. *J Am Chem Soc* **2010,** *132* (43), 15299-307.

10. Zheng, G.; Daniel, W. L.; Mirkin, C. A., A new approach to amplified telomerase detection with polyvalent oligonucleotide nanoparticle conjugates. *J Am Chem Soc* **2008,** *130* (30), 9644-5.

11. Kulla, E.; Katz, E., Biosensor Techniques Used for Determination of Telomerase Activity in Cancer Cells. *Sensors (Basel)* **2008,** *8* (1), 347-369.

12. Qian, R.; Ding, L.; Ju, H., Switchable fluorescent imaging of intracellular telomerase activity using telomerase-responsive mesoporous silica nanoparticle. *J Am Chem Soc* **2013,** *135* (36), 13282-5.

13. Wu, L.; Wang, J.; Feng, L.; Ren, J.; Wei, W.; Qu, X., Label-free ultrasensitive detection of human telomerase activity using porphyrin-functionalized graphene and electrochemiluminescence technique. *Adv Mater* **2012,** *24* (18), 2447-52.

14. Hiyama, E.; Hiyama, K., Telomerase detection in the diagnosis and prognosis of cancer. *Cytotechnology* **2004,** *45* (1-2), 61-74.

15. Shay, J. W.; Gazdar, A. F., Telomerase in the early detection of cancer. *J Clin Pathol* **1997,** *50* (2), 106-9.

16. Cunningham, V. J.; Markham, N.; Shroyer, A. L.; Shroyer, K. R., Detection of telomerase expression in fine-needle aspirations and fluids. *Diagn Cytopathol* **1998,** *18* (6), 431-6.

17. Hess, J. L.; Highsmith, W. E., Jr., Telomerase detection in body fluids. *Clin Chem* **2002,** *48* (1), 18-24.

18. Sugino, T.; Yoshida, K.; Bolodeoku, J.; Tarin, D.; Goodison, S., Telomerase activity and its inhibition in benign and malignant breast lesions. *J Pathol* **1997,** *183* (1), 57-61.

19. Yaku, H.; Murashima, T.; Miyoshi, D.; Sugimoto, N., A highly sensitive telomerase activity assay that eliminates false-negative results caused by PCR inhibitors. *Molecules* **2013,** *18* (10), 11751-67.

20. Wright, W. E.; Shay, J. W.; Piatyszek, M. A., Modifications of a telomeric repeat amplification protocol (TRAP) result in increased reliability, linearity and sensitivity. *Nucleic Acids Res* **1995,** *23* (18), 3794-5.

21. Li, H.; Huang, J.; Lv, J.; An, H.; Zhang, X.; Zhang, Z.; Fan, C.; Hu, J., Nanoparticle PCR: nanogold-assisted PCR with enhanced specificity. *Angew Chem Int Ed Engl* **2005,** *44* (32), 5100-3.

22. Li, M.; Lin, Y. C.; Wu, C. C.; Liu, H. S., Enhancing the efficiency of a PCR using gold nanoparticles. *Nucleic Acids Res* **2005,** *33* (21), e184.

23. Yang, X. H.; Wang, L.; Wang, K. M.; Tan, W. H.; Tang, H. X.; Meng, X. X.; Guo, Q. P., Novel protein detection method based on proximity-dependent polymerase reaction and aptamers. *Chinese Science Bulletin* **2008,** *53* (2), 204-208.

24. Mi, L.; Wen, Y.; Pan, D.; Wang, Y.; Fan, C.; Hu, J., Modulation of DNA polymerases with gold nanoparticles and their applications in hot-start PCR. *Small* **2009,** *5* (22), 2597-600.

25. Shen, C.; Yang, W.; Ji, Q.; Maki, H.; Dong, A.; Zhang, Z., NanoPCR observation: different levels of DNA replication fidelity in nanoparticle-enhanced polymerase chain reactions. *Nanotechnology* **2009,** *20* (45), 455103.

26. Chen, P.; Pan, D.; Fan, C.; Chen, J.; Huang, K.; Wang, D.; Zhang, H.; Li, Y.; Feng, G.; Liang, P.; He, L.; Shi, Y., Gold nanoparticles for high-throughput genotyping of long-range haplotypes. *Nat Nanotechnol* **2011,** *6* (10), 639-44.

27. Zyrina, N. V.; Artiukh, R. I.; Svad'bina, I. V.; Zheleznaia, L. A.; Matvienko, N. I., [Effect of single-stranded DNA binding proteins on template/primer-independent DNA synthesis in the presence of nicking endonuclease Nt.BspD6I]. *Bioorg Khim* **2012,** *38* (2), 199-205.

28. Tian, L. L.; Cronin, T. M.; Weizmann, Y., Enhancing-effect of gold nanoparticles on DNA strand displacement amplifications and their application to an isothermal telomerase assay. *Chemical Science* **2014,** *5* (11), 4153-4162.

29. Wege, H.; Chui, M. S.; Le, H. T.; Tran, J. M.; Zern, M. A., SYBR Green real-time telomeric repeat amplification protocol for the rapid quantification of telomerase activity. *Nucleic Acids Res* **2003,** *31* (2), E3-3.

30. Liu, J.; Cao, Z.; Lu, Y., Functional nucleic acid sensors. *Chem Rev* **2009,** *109* (5), 1948-98.

31. Sun, D.; Lopez-Guajardo, C. C.; Quada, J.; Hurley, L. H.; Von Hoff, D. D., Regulation of catalytic activity and processivity of human telomerase. *Biochemistry* **1999,** *38* (13), 4037-44.

32. Wilson, I. G., Inhibition and facilitation of nucleic acid amplification. *Appl Environ Microbiol* **1997,** *63* (10), 3741-51.

33. Al-Soud, W. A.; Jönsson, L. J.; Rådström, P., Identification and Characterization of Immunoglobulin G in Blood as a Major Inhibitor of Diagnostic PCR. *Journal of Clinical Microbiology* **2000,** *38* (1), 345-350.

34. Rosi, N. L.; Mirkin, C. A., Nanostructures in biodiagnostics. *Chem Rev* **2005,** *105* (4), 1547-62.

35. Zhang, X.; Servos, M. R.; Liu, J., Surface science of DNA adsorption onto citrate-capped gold nanoparticles. *Langmuir* **2012,** *28* (8), 3896-902.

36. Deka, J.; Paul, A.; Chattopadhyay, A., Sensitive Protein Assay with Distinction of Conformations Based on Visible Absorption Changes of Citrate-Stabilized Gold Nanoparticles. *J Phys Chem C* **2009,** *113* (17), 6936-6947.

37. Zhang, D.; Neumann, O.; Wang, H.; Yuwono, V. M.; Barhoumi, A.; Perham, M.; Hartgerink, J. D.; Wittung-Stafshede, P.; Halas, N. J., Gold nanoparticles can induce the formation of protein-based aggregates at physiological pH. *Nano Lett* **2009,** *9* (2), 666-71.

38. Lacerda, S. H.; Park, J. J.; Meuse, C.; Pristinski, D.; Becker, M. L.; Karim, A.; Douglas, J. F., Interaction of gold nanoparticles with common human blood proteins. *ACS Nano* **2010,** *4* (1), 365-79.

39. Deka, J.; Paul, A.; Chattopadhyay, A., Modulating enzymatic activity in the presence of gold nanoparticles. *Rsc Advances* **2012,** *2* (11), 4736-4745.

40. Mi, L.; Zhang, X.; Yang, W.; Wang, L.; Huang, Q.; Fan, C.; Hu, J., Artificial nano-bio-complexes: effects of nanomaterials on biomolecular reactions and applications in biosensing and detection. *J Nanosci Nanotechnol* **2009,** *9* (4), 2247-55.

41. Daxiang, C.; Furong, T.; Yong, K.; Igor, T.; Huajian, G., Effects of single-walled carbon nanotubes on the polymerase chain reaction. *Nanotechnology* **2004,** *15* (1), 154.

42. Cui, D.; Li, Q.; Huang, P.; Wang, K.; Kong, Y.; Zhang, H.; You, X.; He, R.; Song, H.; Wang, J., Real time PCR based on fluorescent quenching of mercaptoacetic acid-modified CdTe quantum dots for ultrasensitive specific detection of nucleic acids. *Nano Biomed Eng* **2010,** *2* (1), 45-55.

43. Olszewski, M.; Rebala, K.; Szczerkowska, Z.; Kur, J., Application of SSB-like protein from Thermus aquaticus in multiplex PCR of human Y-STR markers identification. *Mol Cell Probes* **2005,** *19* (3), 203-5.

44. Li, G.; Cui, Q., Analysis of functional motions in Brownian molecular machines with an efficient block normal mode approach: myosin-II and Ca2+ -ATPase. *Biophys J* **2004,** *86* (2), 743-63.

Chapter 3 – Plasmonic photothermal gold bipyramid nano-reactors for ultrafast real-time bioassays

3.1 Introduction

Nucleic acid amplifications (NAAs) have shown significant potential as sensitive and reliable tools for biological and medical research of nucleic acids and other bioanalytes[1-5]. As seen in the previous chapter these NAAs use enzymatic machinery to drive polymerization, cleavage, and other operations on the nucleic acids to create detectable signals. Two classes of methods have emerged as specific enzymes and amplification schemes require different temperature conditions for optimal performance: thermocycling and isothermal[6-8]. Thermocycling protocols, such as the polymerase chain reaction (PCR), control the majority of the applications, but some isothermal methods have shown superior performance and levels of detection[9-11]. Several of these isothermal methods have achieved clinical relevance and have earned FDA approval[8, 11]. Despite the successful application in many fields, one limitation persists: the sophisticated, but expensive, time-consuming, heavy, and energetically draining instrumentation (Peltier-devices) required to achieve the necessary temperatures or thermocycling[12-14]. In this chapter, we introduce a plasmonic photothermal method for quantitative real-time PCR, using gold bipyramids and light to achieve ultrafast thermocycling. Moreover, we successfully extend our photothermal system to other biological assays, such as isothermal nucleic acid amplification and restriction enzyme digestion.

Many strategies have sought to decrease the overall assay time by replacing this instrumentation with other devices focused on more rapid heating and cooling. Several methods using microfluidics, nanodroplets, and mechanical manipulation with water baths have impressive thermocycling rates and offer rapid analysis[15-16]. Despite a large number of

advancements in these research directions, there are still several key limitations concerning sample preparation and device construction, limiting these methods as potential alternatives to the current PCR approach[12, 17]. Recently, several groups have combined the field of metallic nanoparticles and films with NAAs to achieve photothermal-based thermocycling[18-21]. These methods offer low-energy, light-based platforms for precise temperature control and show great potential for rapid analysis and point-of-care analytics. However, the particles and films currently used for these systems preclude the possibility of real-time analysis, due to the overlap of the absorption spectra of these nanostructures with those of widely used fluorescent dyes[20, 22]. Real-time analysis is integral to the development of mobile, point-of-care, and high-throughput analytics because it eliminates the need for gel electrophoresis or other post-amplification processess[3]. Therefore, there is a critical need to provide new nanotechnologies to address these clear limitations in the current methodologies and to improve detection time, system mobility, and the cost- and energy-efficiency of these important biochemical and medical assays while retaining real-time capabilities. This chapter will summarize our findings of a simple and universal plasmonic photothermal (PPT) temperature control system using monodisperse gold bipyramid nanostructures (AuBPs) as individual, IR-light-absorbing, precision-heating nano-reactors for ultrafast, quantitative, and real-time PCR amplification assays (the contents of this chapter are reproduced in part with permission from a published paper[23]).

3.2 Results and Discussion

3.2.1 Plasmonic photothermal thermocycling

Our PPT-NAAs are based on the light-driven photothermal heating of the AuBPs, which are evenly dispersed in the reaction mixture in a typical PCR tube (Figure 3.1). The device also uses two light-emitting diodes (LEDs) as light sources: an IR-LED (850 nm peak wavelength) for

excitation of the localized surface plasmon and a blue-LED (480 nm peak wavelength) to allow real-time measurements (Figure 3.1B and Figure 3.2)

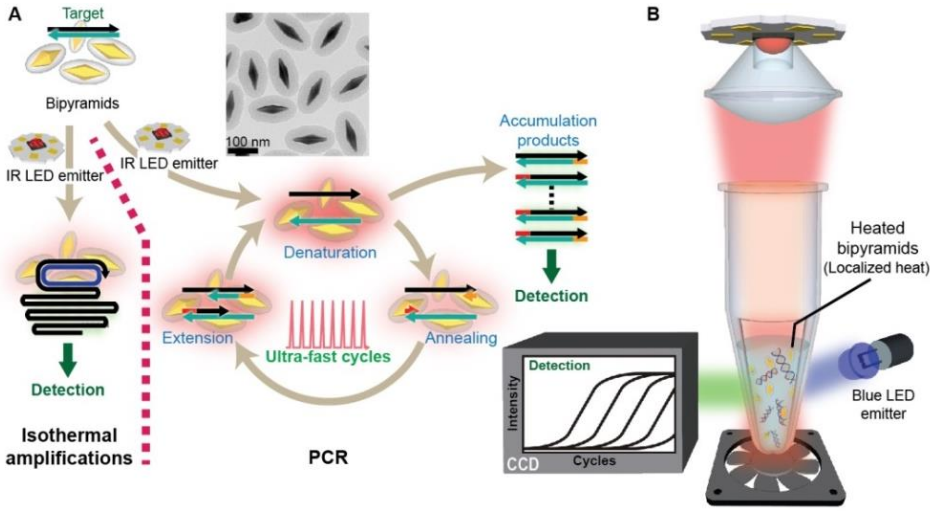

Figure 3.1 Schematic representation of the PPT-qPCR system A) PPT-based NAAs schemes and transmission electron microscopy (TEM) image of the synthesized PEG-Si-AuBPs. B) Scheme of the LED-assisted photothermal device using PEG-Si-AuBPs for thermocycling and real-time detection.

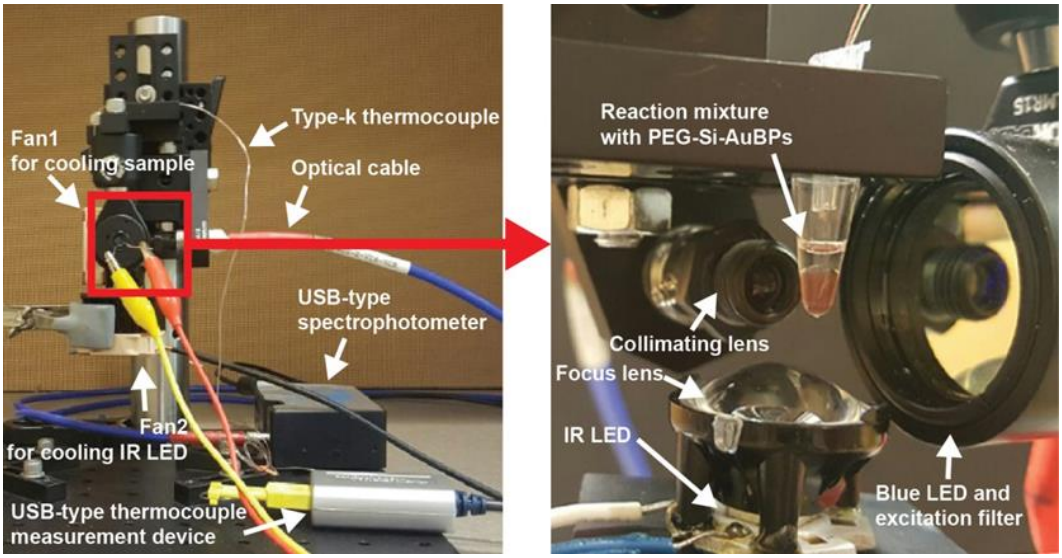

Figure 3.2 Plasmonic photothermal device setup Left: Homebuilt device used for all the LED-assisted plasmonic photothermal temperature control and real-time detection for PPT-qPCR, PPT-qRCA, and PPT-multi-enzyme restriction digestion. Right: Inside look of the reaction setup for a typical 200 µL PCR tube.

When the reaction solution containing the DNA target and AuBPs is exposed to the IR-LED, the AuBPs act as nano-reactors to absorb the photonic energy and convert it to heat energy, rapidly increasing the temperature of the solution[22, 24]. In addition, constant and discrete temperatures for isothermal or thermocycling amplification can be achieved by pulsation of the IR-LED. During the annealing or extension phase, the accumulated products were measured as a function of the fluorescence emitted from intercalating dyes commonly used for PCR, which were excited by the blue LED and detected via a spectrophotometer. Upon absorbance of a photon, there are no significant energy-loss pathways other than the photothermal heat dissipation for gold nanoparticles[25].

Even and uniform heating throughout the solution is necessary to achieve homogeneity of the reaction, therefore, nanoparticles with a low polydispersity in size and shape, narrow absorbance line width, and a high extinction coefficient would provide optimal photothermal response. AuBPs, having a highly tunable longitudinal surface plasmon resonance (LSPR) and a polydispersity of < 2% in both size and shape, correlating to a similarly narrow linewidth, allow specific photo-excitation and thermal-release and ensure precise and uniform heating[22, 24, 26]. To our knowledge, AuBPs are the most uniform and monodisperse nanoparticles reported and have a higher absorbance coefficient than nanorods or nanospheres[27], further demonstrating their advantages over other well-studied gold nanoparticles. Furthermore, the resonant wavelength of the AuBPs (LSPR = 846 nm) for photothermal heat conversion is in the near-IR (NIR) spectrum and far from the excitation wavelengths of the fluorescent dyes routinely used in NAAs, such as SYBR® Green I dye (SG1, excitation = 497 nm and emission = 520 nm). This eliminates photo-bleaching of the dyes and makes the AuBPs ideal for real-time assays[20]. To increase the stability of the AuBPs and maintain their uniformity in harsh conditions, such as the high temperatures

and relatively high divalent cation concentrations typical for PCR reactions, the AuBPs were coated with a silica shell[28-29]. It is worth noting that stirring is important for uniform coating of the silica shell. Faster stirring could result in irregular shape of the shell and tip-exposed structures (Figure 3.3). After the deposition of the silica shell, the particles were modified by silanization with methoxy-poly(ethylene glycol)-silane (PEG, MW = 5000) to prevent non-specific binding of DNA or other bio-reagents (Figure 3.3 and Figure 3.4)[30].

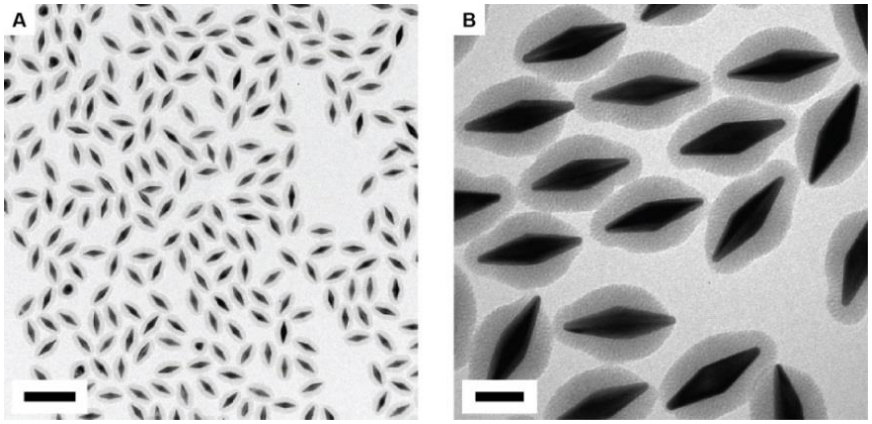

Figure 3.3 Effect of different stirring speeds on the synthesis of PEG-Si-AuBPs A) Wide-field TEM image of the synthesized PEG-Si-AuBPs (5K PEG) in Figure 1A, stirred at 50 rpm. Scale bar is 400 nm. B) TEM image of the synthesized PEG-Si-AuBPs (5K PEG) at higher speed stirring (> 50 rpm). Scale bar is 50 nm.

Silica coating of AuBPs offers thermal stability against the reshaping of the nanoparticles by oxidative etching (Figure 3.4)[26, 29], and also helps improve heat dissipation into the medium surrounding the nanoparticle surface, resulting in rapid heating of the solution[31]. In addition, the silica shell acts as a spacer to prevent quenching of the fluorescent dyes, which occurs when plasmonic nanoparticles are in close proximity[32-33].

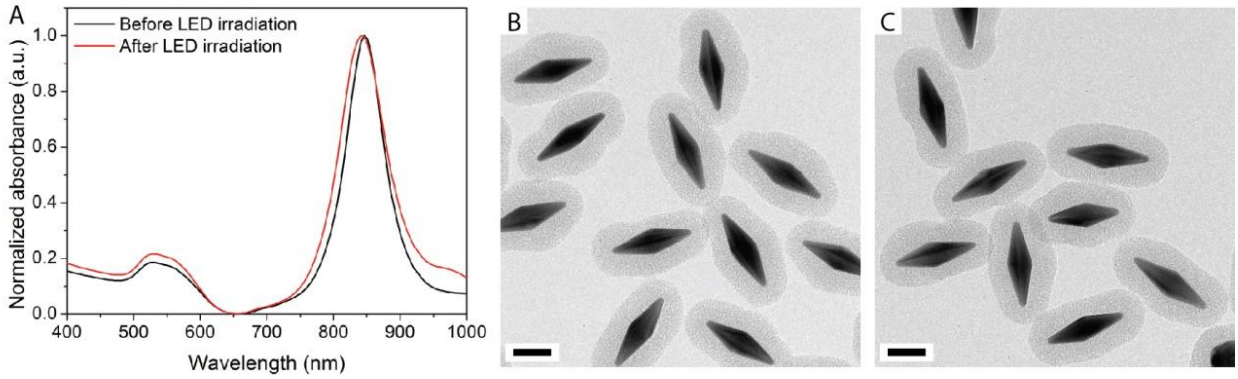

Figure 3.4 Thermal stability of PEG-Si-AuBPs A) Normalized absorbance of PEG-Si-AuBPs at 21.5 OD, before and after IR-LED irradiation for 120 thermocycles. TEM images of PEG-Si-AuBPs before (B) and after (C) IR-LED irradiation for 120 thermocycles between 72 °C and 95 °C. The PEG-Si-AuBPs showed high thermal stability when exposed to IR-LED. 1.5 A injection current was used. Scale bars are 50 nm.

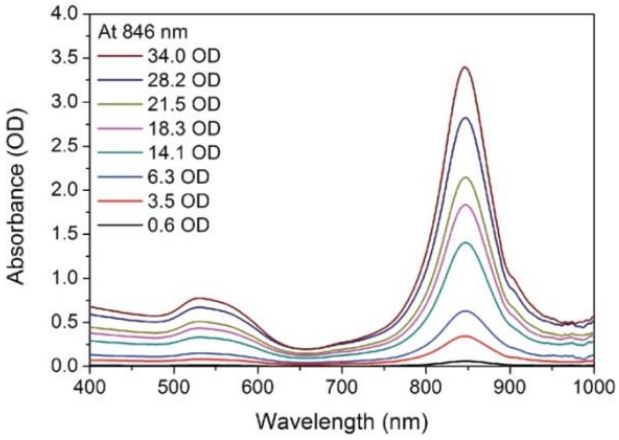

Figure 3.5 Optical density of PEG-Si-AuBPs UV-Vis spectra obtained from the different PEG-Si-AuBPs concentrations used in the PPT thermocycling experiments. A 10-fold dilution was used to measure the absorbance and subsequently calculate the optical density.

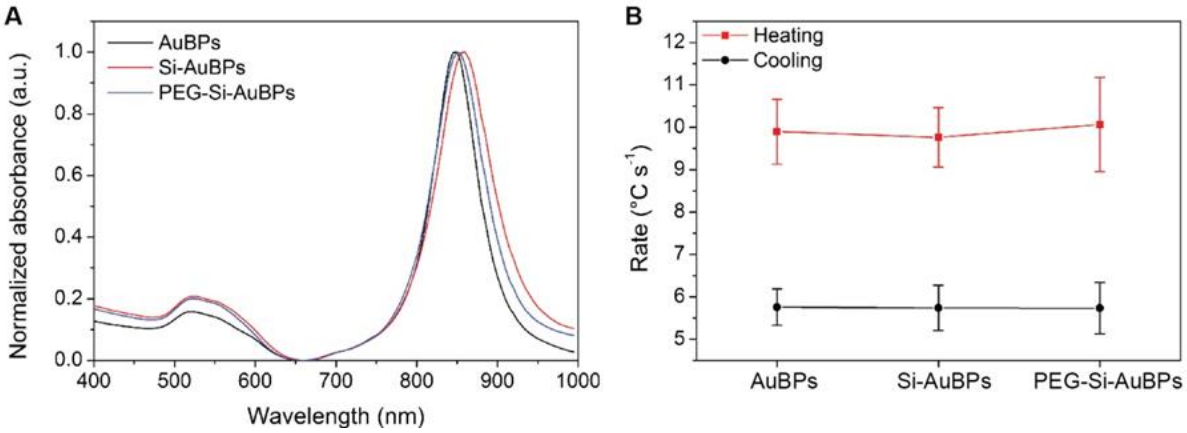

Figure 3.6 Optical and photothermal properties of AuBPs, Si-AuBPs, and PEG-Si-AuBPs A) UV-Vis spectra of AuBPs, Si-AuBPs and 5K PEG-Si-AuBPs. B) Heating and cooling ramp rate of AuBPs, Si-AuBPs, and 5K PEG-Si-AuBPs. Nanoparticles (18.3 OD at 850 nm) were measured to obtain heating and cooling rates. The heating and cooling ramp rates were calculated by dividing the temperature difference between 72 °C to 95 °C with the measured time interval between the two temperatures. 10 µL of nanoparticle solution and 1.5 A injection current (15.33 V) was used. Error bars indicate the standard deviation of the quintuplicate measurements.

The photothermal properties of the PEGylated and silica-coated AuBPs (PEG-Si-AuBPs) were systematically investigated using a home-built IR-LED device with a thermocouple inserted into a PCR tube to accurately measure and record the temperature of the bulk solution. We first demonstrated the thermocycling using different optical densities (ODs) of PEG-Si-AuBPs (Figure 3.5). There is a slight broadening and red-shift of the absorption peak after the silica coating, whereas the peak of the PEG-Si-AuBPs blue-shifts back to the original position but still exhibits a slight broadening compared to that of the AuBPs before the silica coating Figure 3.6A). These results are consistent with the previous observations in the literature. These reports suggest that the chief factor causing this phenomenon is the difference of the refractive indices between the different layers (Si and PEG) in reference to the solution media (water) [34-35]. However the heating and cooling rates remained consistent (Figure 3.6B). The representative temperature profiles (Figure 3.7A) show the rapid thermocycling (30 cycles) between 72 °C and

95 °C. There were no significant temperature changes in the absence of PEG-Si-AuBPs (Figure 3.7).

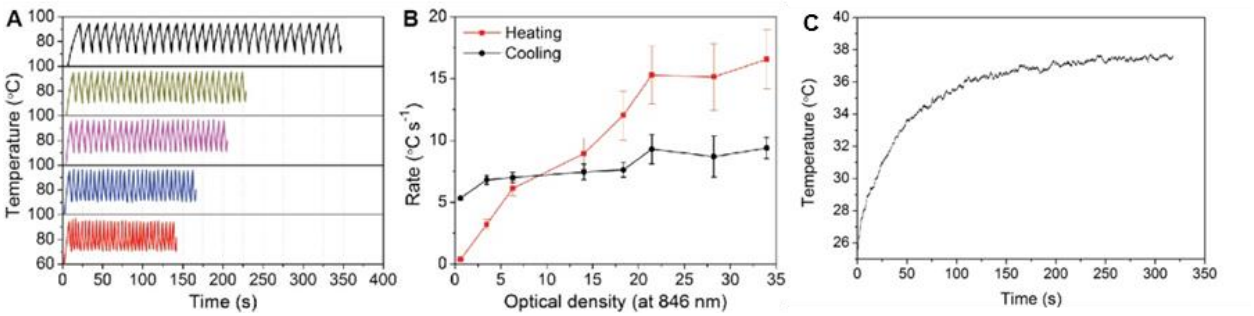

Figure 3.7 PPT thermocycling of PEG-Si-AuBPs A) Thermocycling temperature profiles at different PEG-Si-AuBPs concentrations of 30 thermocycles between 72 °C and 95 °C with fixed solution volume of 5 µL and varying optical densities of PEG-Si-AuBPs. From top to bottom: 3.5 OD, 6.3 OD, 14.1 OD, 18.3 OD and 21.5 OD. B) Heating and cooling ramp rates calculated from panel A. Error bars indicate the standard deviation of the quintuplicate measurements. C) Temperature profile for a typical PPT-qPCR reaction mixture without PEG-Si-AuBPs under constant IR-LED irradiation

The accuracy of the setting temperature was measured as 95.35 ± 0.73 °C for 95 °C and 71.57 ± 0.47 °C for 72 °C. The 30-cycle assay time for the 21.5 OD sample was measured at 141.8 ± 12.4 sec (Figure 3.7 and Figure 3.8A), corresponding to the remarkable heating and cooling ramp rates of 16.6 ± 2.4 °C s^{-1} and 9.4 ± 0.8 °C s^{-1}. As the OD was increased from 3.5 to 21.5 the system exhibited a decrease in the time necessary to achieve 30 cycles. As the optical density was increased above 21.5 OD, we observed no significant improvements to the heating rates (Figure 3.7B). It is reasonable to presume there is restricted depth for the photothermal heating efficiency considering that the light penetration will decrease with an increase of the nanoparticle concentration[36-37]. Various sample volumes and injection currents were also investigated and optimized (Figure 3.8). The results indicate that the heating rate increases with a decrease of solution volume to 5 µL and an increase of the injection current to 1.5 A.

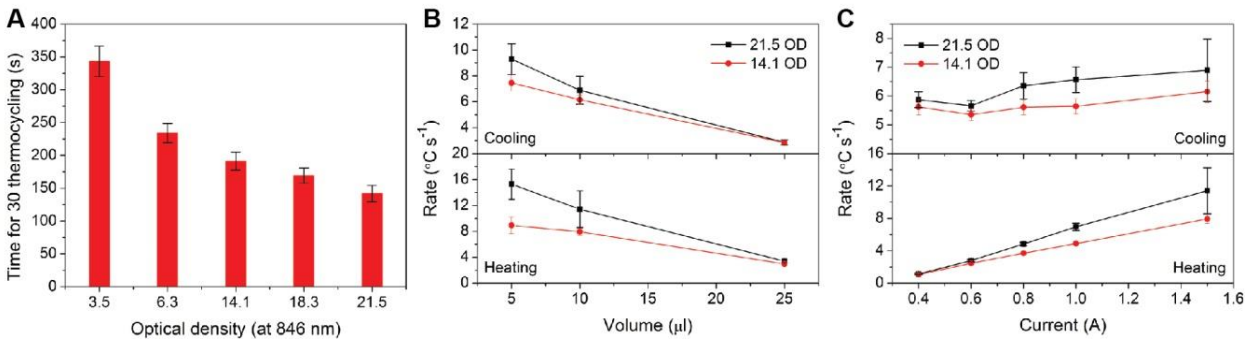

Figure 3.8 Analysis of PPT-thermocycling for different optical densities of PEG-Si-AuBPs A) Average total reaction times for 30 thermocycles with different PEG-Si-AuBPs concentrations. Averages and standard deviations calculated for quintuplicate measurements. B) PEG-Si-AuBPs optical densities of 14.1 and 21.5 ODs were measured to obtain heating and cooling rates depending on the reaction volumes. The heating and cooling ramp rates were calculated by dividing the temperature difference between 72 °C to 95 °C with the measured time interval between the two temperatures. C) PEG-Si-AuBPs optical densities of 14.1 and 21.5 ODs were measured to obtain heating and cooling rates depending on the injection currents. The voltages for different injection currents in panel C were measured as 12.48, 13.04, 13.57, 14.08, and 15.33 V for 0.4, 0.6, 0.8, 1.0, and 1.5 A, respectively. 1.5 A injection current was used in this Figure for plasmonic photothermal heating except in panel C. 15 µL of Chill-out™ liquid wax on top of the PEG-Si-AuBPs solution was added to prevent evaporation during the thermocycling except in panel B.

3.2.2 PPT-qPCR

Quantitative real-time PCR (qPCR) has been a benchmark technique across many disciplines due to the ability to monitor the amplification kinetics in real time to quantify nucleic acid products[38-39]. We, therefore, adapted our system to create a PPT-qPCR for the detection and amplification of trace nucleic acid samples. Because the fluorescent emission of organic dyes in proximity to metallic nanoparticle surfaces in colloidal suspension suffers from a significant quenching[32], we first optimized the fluorescent intensity by varying the concentration of the dye, the optical density of the PEG-Si-AuNPs and the length of the PEG units to increase the signal-to-noise ratio. The characteristic fluorescence spectrum of SG1 was measured in the PPT-qPCR mixtures with the PEG-Si-AuNPs (Figure 3.9A). While controlling the temperatures of the denaturation (95 °C, 0 s) and the annealing/extension (72 °C, 2 s) with the IR-LED (Figure 3.9B

and Figure 3.9C), the amplification was monitored in real-time by measuring the fluorescence produced by SG1 upon excitation from a blue-LED (Figure 3.10B and Figure 3.10C).

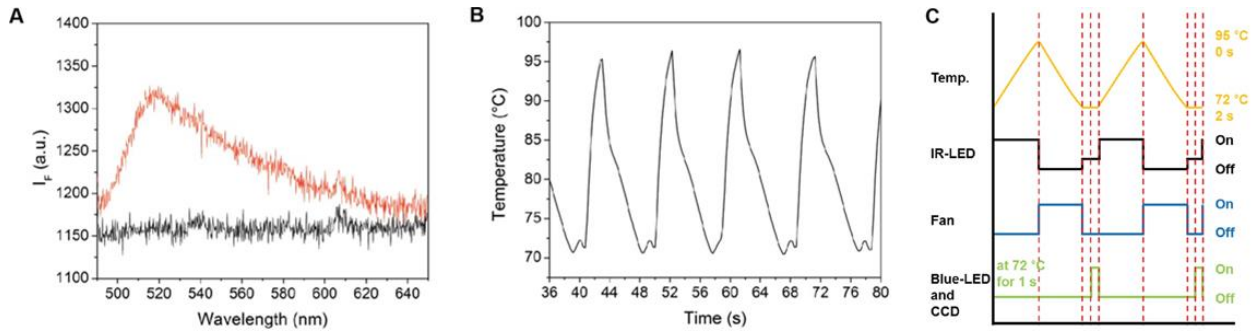

Figure 3.9 PPT-qPCR fluorescence, temperature, and real-time execution profiles A) Measured background (black) and fluorescent emission signal of the SG1 (×7) (red) after 35 thermocycles. B) Representative temperature profile for the PPT-qPCR with the denaturation step at 95 °C and the annealing/extension step at 72 °C. C) Schematic representation of the PPT-qPCR approach. Real-time execution profile performed by the photothermal LED device. To maintain the temperature at 72 °C for 2 s, low injection current (0.17 A) was used. The fluorescence from the accumulated products was excited during the annealing/extension stage and the emission was collected for 1 s at 520 nm with the blue-LED to monitor the real-time amplification.

We performed a series of experiments to optimize the SG1 concentrations with different PEG lengths and Si-AuNPs concentrations (Figure 3.10). Viral M13 amplicon, derived from the bacteriophage M13, was amplified with the PEG-Si-AuBPs and SG1 fluorescent dye (Figure 3.10). The intensities of the fluorescent signals produced within the plateau phase of each sample were averaged after the background subtractions and compared to determine the optimal reaction mixture (Figure 3.10). The results indicate that the fluorescence is proportional to the amount of SG1 and inversely proportional to the optical density of the PEG-Si-AuNPs (Figure 3.11). Considering that the fluorescence quenching property of noble metal nanoparticles is distance-dependent, it is reasonable that the fluorescence is higher when using the particles modified with 5K PEG than that with 2K PEG due to their larger hydrodynamic radius.

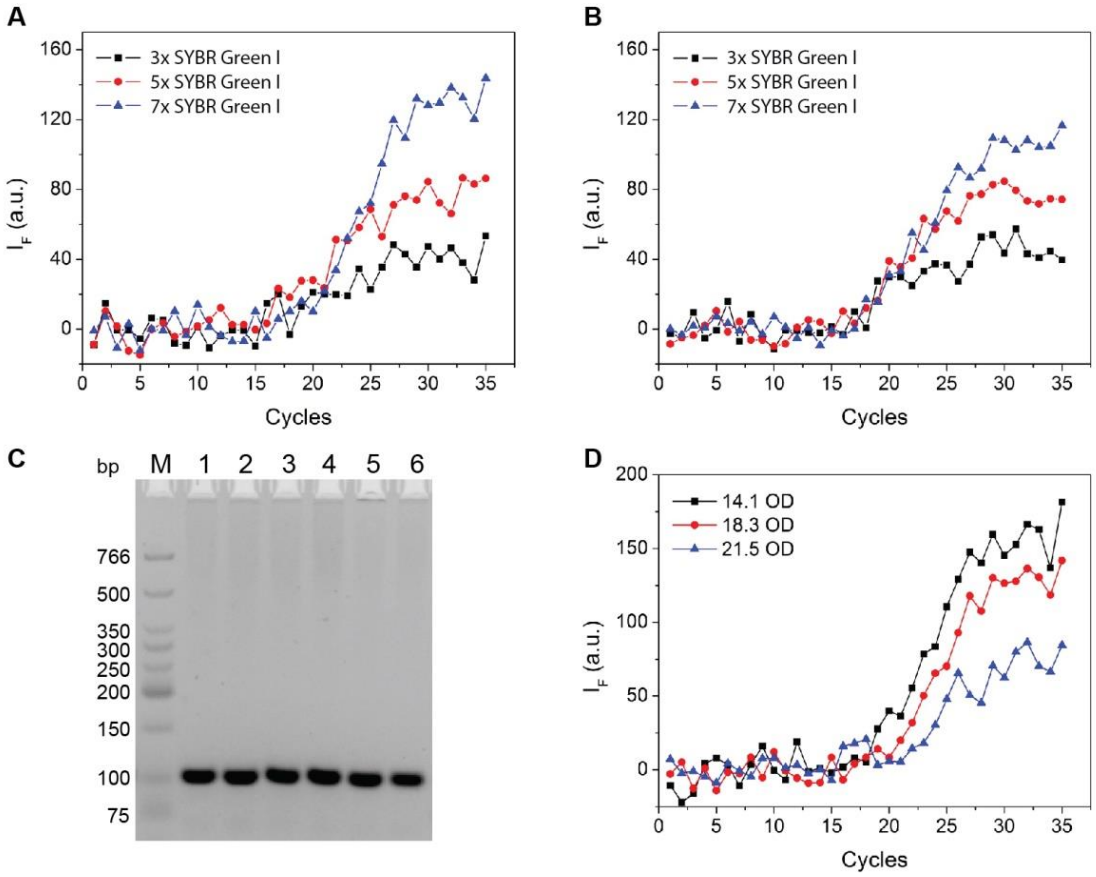

Figure 3.10 PPT-qPCR optimization: SG1 and PEG-Si-AuBPs concentrations and PEG lengths PPT-qPCR amplification curves of M13mp18 DNA template (1 ng μL^{-1}) were obtained to optimize the amount of SG1, PEG length, and nanoparticle concentration. A) Using Si-AuBPs modified with 5K PEG and different SG1 concentrations; B) Using Si-AuBPs modified with 2K PEG and different SG1 concentrations. Optical density of each PEG-Si-AuBPs solution was fixed to 18.3. C) 3% agarose gel electrophoresis of PPT-qPCR assay of panels A and B: lane M, low molecular weight DNA ladder; lane 1 to 3, 3× and 5× and 7× SG1 with 5K PEG-Si-AuBPs, respectively; lane 4 to 6, 3× and 5× and 7× SG1 with 2K PEG-Si-AuBPs, respectively. D) Amplification of M13mp18 DNA template (1 ng μL^{-1}) at different optical densities of 5K PEG-Si-AuBPs with fixed SG1 (×7) concentration. All the experiments were stopped after 35 thermocycles. The background signal was determined with the common approach that uses the fluorescence during early cycles, such as between cycles 5 and 15, which shows no significant signal or change before the exponential signal appears.

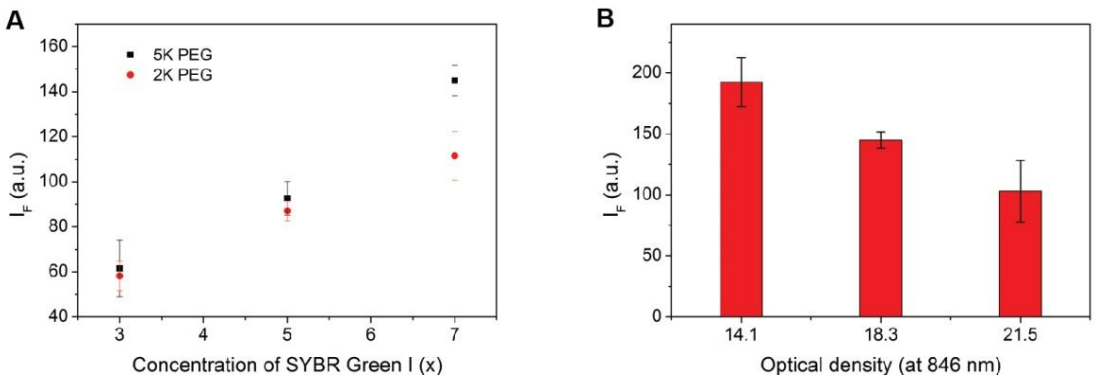

Figure 3.11 Optimization of fluorescent signal A) Comparison of the measured fluorescence after 35 thermocycles depending on the amount of SG1 with the fixed optical density of PEG-Si-AuBPs, 18.3 OD. Error bars indicate the standard deviation of the quintuplicate measurements. B) Comparison of the measured fluorescence after 35 thermocycles at different optical densities of PEG-Si-AuBPs (5K) with the fixed amount of the SG1 (7×). Error bars indicate the standard deviation of the quintuplicate measurements. To compare the intensities of the fluorescence in Figure 4.10, the intensities of the fluorescence signals produced within the plateau phase of each of the samples were averaged after the background subtractions, indicating the consumption of almost all of the existing dye in the solution.

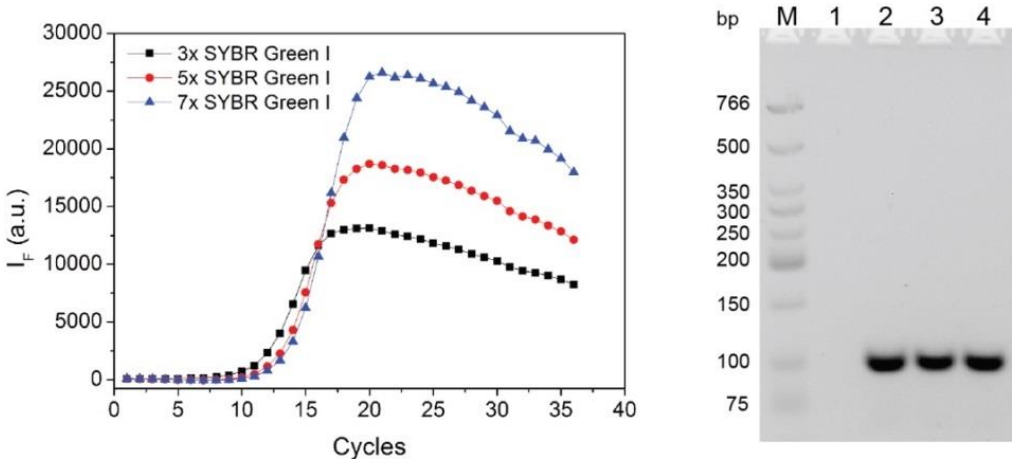

Figure 3.12 Inhibition by fluorescent dyes on PPT-qPCR Left: Amplification curves of M13mp18 DNA template (1 ng μL^{-1}) were obtained using conventional PCR machine without PEG-Si-AuBPs to observe inhibition of the amplification reaction depending on the amount of SG1 during 35 thermocycles (95 °C for 5 s, 72 °C for 5 s). Right: 3% agarose gel electrophoresis: lane M, low molecular weight DNA ladder; lane 1, negative control without M13mp18 DNA template; lane 2 to 4, 3× and 5× and 7× SG1, respectively.

It is known that the amplification reaction can be inhibited in the presence of large concentrations of SG1[39], however, there was no obvious inhibition of the amplification by SG1

at ×7 (Figure 3.12).Under optimized conditions, the amplification reactions consisting of PEG-Si-AuNPs (5K PEG, 18.3 OD) and serial dilutions of the M13mp18 amplicon in a final volume of 10 µL PCR mixture including SG1 (×7) and KAPA2G fast DNA polymerase were monitored by the PPT-qPCR system (Figure 3.13A).

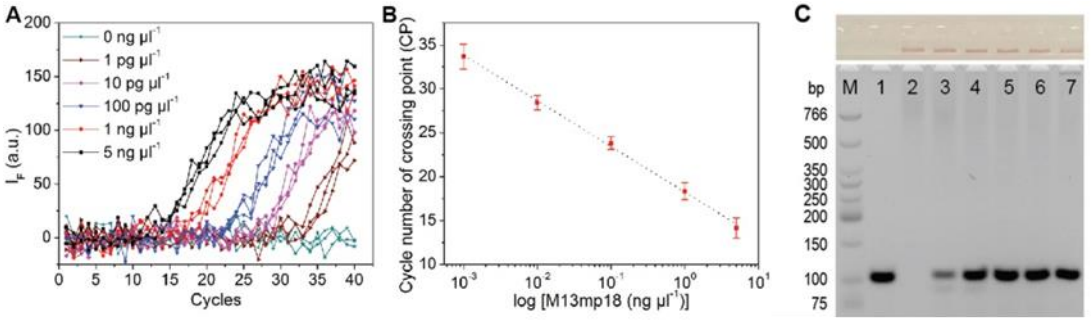

Figure 3.13 PPT-qPCR amplification of nucleic acid samples A) PPT-qPCR amplification curves corresponding to 100 base pairs DNA products obtained from different concentrations of M13mp18 DNA template. B) Crossing point values plotted against the logarithm of the M13mp18 DNA template concentrations. Error bars indicate standard deviation of triplicate measurements. C) 3% agarose gel electrophoresis image of the PPT-qPCR assay: lane M, low molecular weight DNA ladder; lane 1, positive control corresponding to M13mp18 DNA template, 1 ng μl^{-1}, amplified in the absence of PEG-Si-AuBPs using the CFX96 PCR system; lane 2, negative control performed in the presence of PEG-Si-AuBPs, and in the absence of the M13mp18 DNA template using PPT device, and shows no amplification product band; lanes 3 to 7, corresponding to 1 pg μl^{-1} to 5 ng μl^{-1} of M13mp18 DNA template amplified in the presence of PEG-Si-AuBPs using PPT device, and show 100 base pairs DNA product bands. Upper photograph of the gel shows the PEG-Si-AuBPs accumulated in the well after the electrophoretic process.

Triplicate measurements were recorded and the fluorescent emission at 520 nm was plotted as a function of cycle number. The results indicated that PPT-qPCR could finish 40 cycles within 7.5 minutes (Figure 3.13A and Figure 3.14A) and detect the target templates over a large dynamic range from 5 ng μL^{-1} to 1 pg μL^{-1}. Plotting the Crossing point values (Figure 3.13B and Figure 3.14B) against the logarithm of the M13mp18 concentrations (Figure 3.13B) resulted in a standard curve showing a consistent linear relationship with the correlation equation of CP = 17.98 – 5.30 log [M13mp18] (R^2 = 0.99643)[40-42]. CP is related to the cycle number at which the

fluorescence starts to increase drastically above the background signals for the quantification of the amplified product.

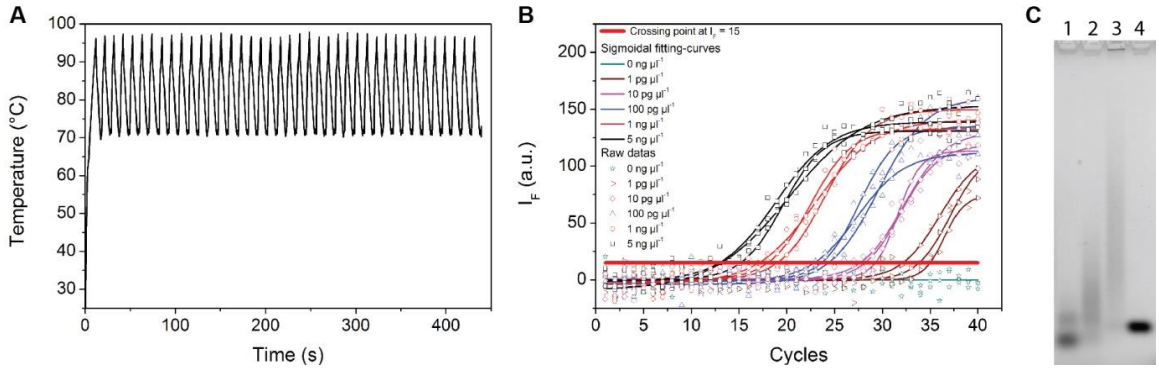

Figure 3.14 Temperature profile, sigmoidal fitting-curves, and gel electrophoresis analysis for PPT-qPCR A) Representative photothermal amplification temperature profile used in Figure 3A: 40 thermocycles, 95 °C (0 s) denaturation step and 72 °C (2 s) annealing/extension step. B) Four-parameter sigmoidal fitting-curves of the measured fluorescence used to determine the crossing point (CP) in Figure 4.14. C) 3% Agarose gel electrophoresis of PPT-qPCR results performed with 18.3 OD Si-AuBPs (without PEGylation) and M13mp18 DNA template (1 ng μL^{-1}): lane 1, with 0.5% BSA; lane 2, with 0.3% BSA; lane 3, 0.1% BSA; lane 4, positive control with 5K PEG-Si-AuBPs, and 0.5% BSA.

To compare the amplification reaction with the conventional instrumentation in terms of operating time and conditions, the reaction mixture without PEG-Si-AuBPs was tested with a commercial PCR instrument (Figure 3.15).

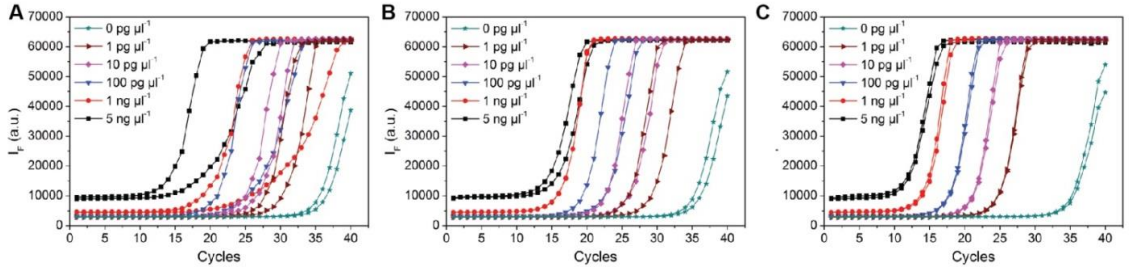

Figure 3.15 Real-time PCR amplification curves obtained from different concentrations of M13mp18 DNA template using conventional instrument (CFX96) without PEG-Si-AuBPs A) 40 thermocycles at 95 °C (1 s) and 72 °C (2 s). B) 40 thermocycles at 95 °C (5 s) and 72 °C (2 s). C) 40 thermocycles at 95 °C (10 s) and 72 °C (2 s). Because the minimum set-time of the CFX96 at each step (denaturation, annealing or extension) is 1 s, we used 1 s as a minimum set-time for denaturation step. Same reaction mixtures as used for Figure 3.14

The amplified products were further characterized by agarose gel electrophoresis (Figure 3.13C). The positive control showed a single band (100 base pairs) of amplified products using a commercial PCR protocol without the PEG-Si-AuNPs (95 °C for 5 s, 72 °C for 5 s, 40 cycles). The results indicate clear changes in band intensities that decrease as the template concentration decreases. We observed particle aggregation during the thermocycles without PEG-modification. The gel analysis shows that the amplified DNA products from the Si-AuBPs without PEG modification could aggregate during the thermocycling and could not be separated from the silica surface due to the non-specific interaction between DNA and the silica surface in the solution with high ionic strength[43]. Intriguingly, the PEG-Si-AuNPs did not pass through the agarose gel and instead remained in the loading well (Figure 3.12C and Figure 3.13C). This makes our PPT-qPCR method highly versatile because the amplified products can be used for further assays or applications without requiring additional purifications to remove the nanoparticles.

3.2.3 Isothermal NAAs

Isothermal NAAs have been shown to be powerful tools for detection and synthetic applications and the diversity of these methods mandates an instrument that can accommodate the various reaction conditions[6-7, 9]. Having shown the successful application of our PPT-method for thermocycling, we worked to extend the PPT system to isothermal NAAs. We adapted our system to perform isothermal bioassays, specifically rolling circle amplifications (RCA), which involves a polymerase infinitely extending a linear primer along a circular template (Figure 3.16)[44].

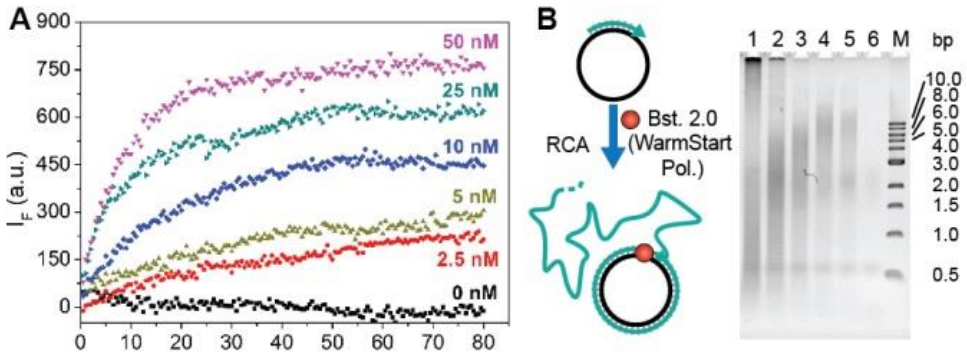

Figure 3.16 PPT-qRCA of nucleic acid samples A) PPT-qRCA curves corresponding to different concentrations of circular DNA template (0 to 50 nM). B) Schematic illustration of the isothermal RCA reaction. Gel analysis of PPT-qRCA assay. PPT-qRCA products obtained in panel A were analyzed by 2% agarose gel electrophoresis: lanes 1 to 5, 50 nM to 2.5 nM of amplified circular DNA templates show broad smears corresponding to different DNA product lengths; lane 6, negative control was measured using PPT device in the presence of PEG-Si-AuBPs and in the absence of circular DNA template, and shows no DNA product; lane M, 1kb DNA ladder.

We designed a circular template of 60 nucleotides and used a highly processive, strand-displacing DNA polymerase, *Bst* 2.0, with a fixed temperature of 55 °C (54.28 ± 0.72 °C, Figure 3.17A). The SYBR® Green II fluorescent dye bound to the accumulated products was excited with the blue-LED, and the emission was collected and monitored every 30 s for 80 min at 520 nm in real time and the intensities were compared to determine the degree of amplification (Figure 3.17B). The fluorescence of each sample before photothermal heating was measured for 30 s, and the average values were used as the background signals. The assay results showed a drastic increase of intensity as the template concentration increased (Figure 3.17C for the positive control). The 2% agarose gel image shows distinct changes in band intensity for the different initial template-concentrations using our PPT-qRCA method, further supporting the different amplification rates of the real-time results (Figure 3.16B). , and these were confirmed to be tandem repeat products Figure 3.18

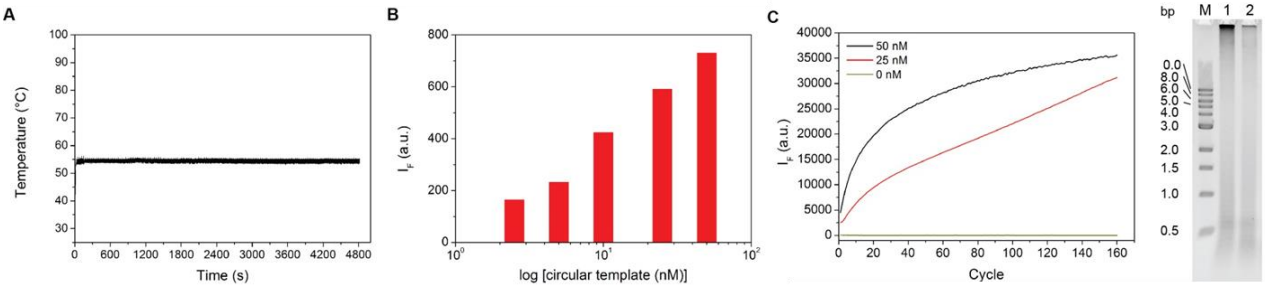

Figure 3.17 Temperature profile of PPT-qRCA and positive control with conventional qPCR machine A) Temperature profile of the isothermal RCA reaction with measured accuracy of 54.28 ± 0.72 °C. B) Fluorescent signals measured at 40 minutes of the RCA reaction in Figure 4A were plotted against the logarithm of circular template DNA concentrations to compare the degree of the amplification. C) Left: Isothermal RCA reaction in the absence of PEG-Si-AuBPs at the fixed temperature of 55 °C using CFX96 Touch™ real-time PCR detection system. The fluorescent signals were collected every 30 s for 160 cycles, which corresponds to 80 minutes. Right: Verification of the RCA reaction by 2% agarose gel electrophoresis: lane M, 1kb DNA ladder; lane 1, circular DNA template (50 nM); lane 2, circular DNA template (25 nM).

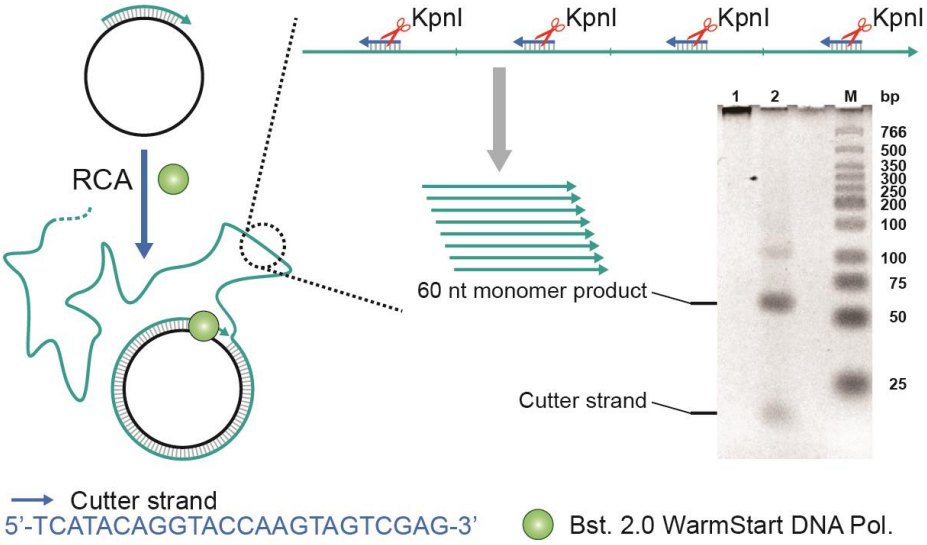

Figure 3.18 Agarose gel analysis of RCA product by PPT-qRCA using Bst 2.0 WarmStart® polymerase after KpnI digestion The RCA product containing tandem repeats complementary to the circular template, lane1, was digested by KpnI restriction enzyme and analyzed by 3% Agarose gel-electrophoresis. After digestion, the monomer product (60 nt) and cutter (24 nt) strands were detected confirming successful RCA amplification, lane 2; lane M, quick-load low molecular weight DNA ladder.

3.2.4 PPT digestion of a plasmid

To demonstrate the capabilities of the PPT method in a multi-enzyme procedure with different temperatures levels, we performed a restriction digestion of a DNA plasmid using different restriction endonucleases. We selected a pBR322 dsDNA plasmid[45], and using the EcoRI and SalI restriction enzymes that are active at 37 °C and inactivated at 65 °C, we tested the ability of PPT system to precisely control the temperature for precise enzyme activity (Figure 3.19A and Figure 3.20).

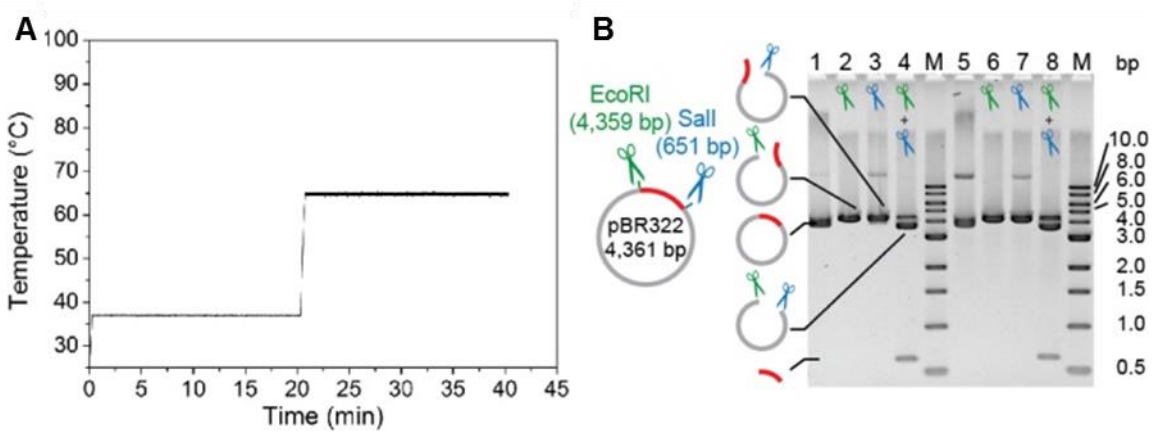

Figure 3.19 PPT-multi-enzyme digestion of nucleic acid samples A) Temperature profile of the PPT-multi-enzyme restriction digestion at 37 °C for 20 min (accuracy of 36.90 ± 0.16 °C) and 65 °C for 20 min (accuracy of 65.54 ± 0.51 °C) enzymes inactivation process. B) Scheme of the multi-enzyme restriction digestion assay. 2% gel agarose image of the digested products obtained by the CFX96 PCR system (lane 1 to 4) and by the PPT method (lane 5 to 8): lane 1 and 5, negative control with neither EcoRI nor SalI enzymes; lane 2 and 6, digestion with EcoRI only; lane 3 and 7, digestion with SalI only; lane 4 and 8, treating with both enzymes; lane M, 1kb DNA ladder.

The products were validated and compared by gel electrophoresis (Figure 3.19B), and show identical cleavage activities and band locations for the Peltier device and our PPT method, indicating no loss of digestion fidelity or enzyme activity. The negative control containing neither enzyme shows an intact circular pBR322 dsDNA band (lanes 1 and 5 in Figure 3.19B). Adding either restriction enzyme shows a band at a slightly higher location than the circular

pBR322 dsDNA band, indicating a cleavage at only one restriction site that results in a linear strand product (lanes 2 and 6 for EcoRI, lanes 3 and 7 for SalI in Figure 3.19B and Figure 3.21).

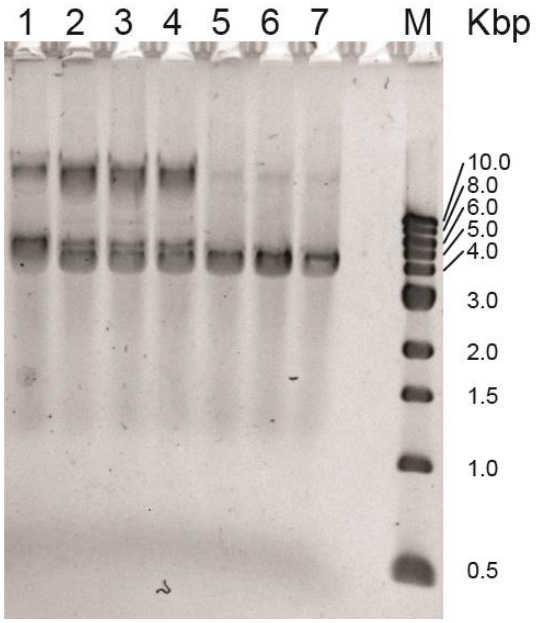

Figure 3.20 1% agarose gel analysis of pBR322 plasmid digested with *Nhe I* restriction enzyme under different temperatures Lane 1, pBR322 plasmid. Lanes 2-4, *Nhe I* digestion at 25 °C (room temperature) shows partial cleavage to the linear form. The incompleteness of the cleavage is due to enzyme having only about 25% activity at room temperature. Lanes 5-7, *Nhe I* digestion at optimal temperature of 37 °C shows complete cleavage to the linear form. Lane M, 1 kb DNA ladder. Lanes 2, 5, exhibit results obtained by IR-LED, the reaction mixtures with 0.5 OD PEG-Si-AuBPs (5K PEG) in 1% BSA were used while maintaining the same concentrations for the others reagents. Lanes 3, 6, are related to the results obtained with the CFX96 Touch™, the reaction mixtures with 0.5 OD PEG-Si-AuBPs (5K PEG) in 1% BSA were used while maintaining the same concentrations for the others reagents. Lanes 4, 7, show results obtained with the CFX96 Touch™, the reaction mixtures without nanoparticles were used while maintaining the same concentrations for the others reagents.

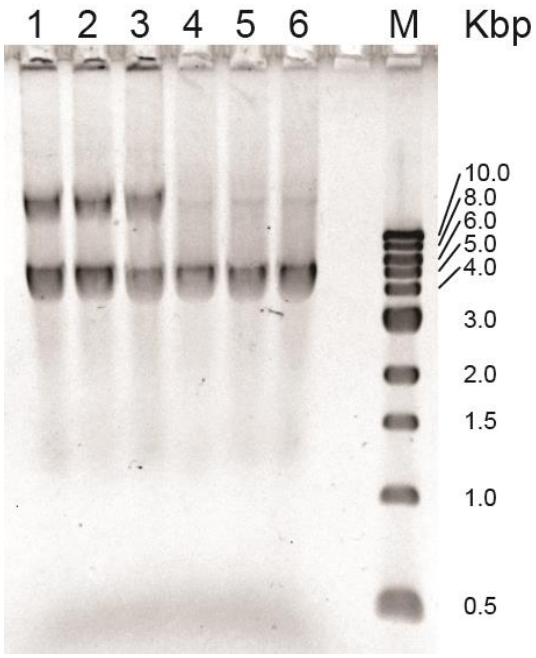

Figure 3.21 pBR322 plasmid analysis 1% Agarose gel analysis of pBR322 plasmid shows two bands: upper – nicked form (relaxed) and lower – supercoiled monomers, lanes 1-3. T5 exonuclease digests nicks of linear or circular dsDNA, while the enzyme does not digest supercoiled dsDNA as shown in lanes 4-6; Lane M, 1 kb DNA ladder. Lanes 1, 4, displays results obtained by IR-LED, the reaction mixtures with 0.5 OD PEG-Si-AuBPs (5K PEG) in 1% BSA were used while maintaining the same concentrations for the others reagents. Lanes 2, 5, are related to the results obtained with the CFX96 Touch™, the reaction mixtures with 0.5 OD PEG-Si-AuBPs (5K PEG) in 1% BSA were used while maintaining the same concentrations for the others reagents. Lanes 3, 6, show results obtained with the CFX96 Touch™, the reaction mixtures without nanoparticles were used while maintaining the same concentrations for the others reagents.

Treatment with both enzymes shows successful cleavage at both restriction sites and two distinct bands with different lengths (lanes 4 and 8 in Figure 3.19B). Similar band intensities from both conventional and PPT methods demonstrate successful separation of the cleaved products from the mixture including PEG-Si-AuBPs. This again implies the use of the digested products for further applications, such as DNA cloning, could be performed without additional treatments.

3.2.5 Conclusions

Our newly developed strategy has successfully demonstrated an ultrafast, low-energy, and real-time PCR by using monodisperse PEG-Si-AuBPs as plasmonic photothermal nano-reactors and an LED as the light source. More importantly, our PPT method is cost-effective (PEG-Si-AuBPs contribute < \$0.01/reaction) and ready-for-use with no need for making significant changes to the protocols of currently existing PCR assays and manufacturer PCR kits. We have achieved 30 cycles of temperature cycling (from 72 °C to 95 °C) in < 2.5 minutes. Our studies concerning the photothermal conversion efficiency, as well as the narrow and discrete absorption spectrum of our highly monodisperse AuBPs indicate that this approach is effective in providing precise temperature control. With regards to the photothermal quantitative real-time PCR, a target sequence can be quantitatively amplified and detected in real-time across a substantial dynamic range from 5 ng μL^{-1} to 1 pg μL^{-1}. Moreover, we have extended our PPT system to isothermal nucleic acid processes such as RCA and multi-enzyme restriction digestion that require fixed and constant temperatures for extended periods of time. The diversity of these temperatures and conditions are shown to be achievable and controllable using our PPT method. Furthermore, the yields achieved are comparable to traditional protocols, suggesting that our method does not compromise the fidelity or integrity of the assays. We believe that the PPT-qPCR method will allow exploitation of the highly developed and sophisticated field of nucleic acid amplification while eliminating the need for the bulky, time-consuming, and expensive instrumentation for greater applications across many research fields.

3.3 Experimental Section

3.3.1 Materials and instruments

All chemicals were purchased from commercial suppliers and used without further purification. Cetyltrimethylammonium bromide (CTAB, Bioxtra, ≥99.0%),

benzyldimethylhexadecylammonium chloride (BDAC, cationic detergent), citric acid trisodium salt dihydrate (≥99.5%, BioUltra, for molecular biology), hydrogen tetrachloroaurate trihydrate ($HAuCl_4 \bullet 3H_2O$), L-ascorbic Acid (Bioxtra, ≥98.0%), tetraethyl orthosilicate (TEOS, reagent grade, 98%), and methanol were purchased from Sigma-Aldrich. Silver nitrate ($AgNO_3$, ≥99.8%) and sodium borohydride ($NaBH_4$, ≥99%) were obtained from Fluka. Hydrochloric acid (HCl, 1 N) was purchased from Fisher scientific. Methoxy-poly(ethylene glycol)-silane (MW = 1,000; 2,000; and 5,000) were acquired from Laysan Bio. Nano-pure water (18.2 MΩ, Barnstead Nanopure, Thermo Scientific, MA, USA) was used in all experiments. The glass vials were purchased from Kimble Chase (4 and 20 mL, NJ, USA). All glassware was cleaned using freshly prepared aqua regia ($HCl:HNO_3$ in a 3:1 ratio by volume) followed by rinsing with copious amounts of water. RCT Basic (IKA, NC, US) was used for magnetic stirring. The formvar/carbon-coated copper grid (Ted Pella, Inc. Redding, CA, USA) and TEM (Tecnai G2 F30 Super Twin microscope, 300 kV and Tecnai G2 Spirit, 200 kV, FEI, OR, USA) were used for the TEM analysis. UV-Vis spectra were measured with UV-2401PC (Shimadzu, Kyoto, Japan) and absorption cuvettes (ultra-micro cell, volume = 50 μL, light path = 10 mm, Mullheim, Germany).

3.3.2 Synthesis of silica-coated gold bipyramids and PEGylation

The gold bipyramids were synthesized with seed-mediated growth and purified according to our reported procedure[26]. After the purification, the precipitation was redispersed and washed with 1 mL of 1 mM CTAB solution, and finally, the purified bipyramids were redispersed in 1.5 mL of 1 mM CTAB solution prior to the silica shell coating. For the synthesis of silica-coated bipyramids, 500 μL of bipyramid solution in 1 mM CTAB was mixed with 500 μL of deionized water in 4 mL vial. In this solution, 1.3 μL of 0.1 M NaOH was added to adjust the pH between

10 - 10.4 and then 8 µL of TEOS (20% v/v in methanol) was added at 30 °C, while quickly stirring for 1 min. After adding TEOS, the solution was gently stirred overnight at 50 rpm. It is worth noting that stirring is important for uniform coating of the silica shell. Faster stirring could result in irregular shape of the shell and tip-exposed structures (Figure 3.3B). The solution was centrifuged at 1,500 *g* for 15 min and washed with 1 mL of deionized water (repeated twice) and methanol (repeated twice), then redispersed in 950 µL of methanol. For the PEGylation, 50 µL of 10 mM methoxy-poly(ethylene glycol)-silane in methanol was added and vortexed for 2 h. Only PEG with molecular weights of 5,000 and 2,000 were used in the real-time assays because the PEG MW = 1,000 aggregates under the same assay conditions. Finally, the resulting solution was centrifuged at 1,500 *g* for 10 min and washed with 1 mL of methanol (repeated twice) and deionized water (repeated twice) and, then redispersed in deionized water. Sonication for a few seconds is needed between the washing steps. To determine the optical density of the nanoparticles, UV-Vis spectra were obtained after the PEGylation. Unless otherwise specified, PEG MW = 5,000 was used for all experiments.

3.3.3 Plasmonic photothermal cycles of PEG-Si-AuBPs by LED

Infrared-LED (850 nm peak wavelength, mounted on metal core PCB, 700 mA forward current, 12.4 V forward voltage, LZ4-40R608, LED Engine, CA, USA) was used for plasmonic heating of PEG-Si-AuBPs, controlled with source meter (Keithley-2636A, Tektronix, Inc., OR, USA). 20.0 mm focus spot top lens fiber coupling (10356, Carclo Optics, PA, USA) was used to focus the light on the samples. Blue-LED (5 mm, 480 nm peak wavelength, 3.2 V forward voltage, 20 mA forward current, 4.1 cd, C503B-BCN-CV0Z0461, CREE, Inc., NC, USA) and FITC excitation filter (center wavelength = 475 nm, band width = 35 nm, MF475-35, Thorlabs, Inc., NJ, USA) were used for excitation of SYBR® Green I and II, and spectrophotometer

(USB4000, Ocean Optics, Inc., FL, USA) and collimating lens (74-series, Ocean Optics, Inc., FL, USA) were used for collection of fluorescent emission signals for real-time measurements. The temperature was measured and recorded with USB-type thermocouple measurement device (USB-TC01, National Instruments, TX, USA) and type-k insulated thermocouple (5SC-TT-K-40-36, OMEGA Engineering, Inc. CT, USA). Thermal cycling with LED, source meter, fluorescence measurement, cooling fans, and temperature measurement were controlled with the LabVIEW program.

PEG-Si-AuBPs with maximum longitudinal peak wavelength of 846 nm in deionized water were used and 30 thermocycles were performed between 72 °C and 95 °C. 5 µL of nanoparticles with different optical densities and 12 µL Chill-out™ liquid wax, clear (CHO-1411, Bio-Rad Laboratories, Inc., CA, USA) were used to determine the cooling and heating rate depending on the optical density of the nanoparticles (Figure 3.7). 5, 10, and 25 µL of PEG-Si-AuBPs with optical densities 14.1 and 21.5 in water (12, 15, and 30 µL liquid wax, respectively) were used to determine the cooling and heating rate depending on the sample volume (Figure 3.8B). 10 µL of nanoparticles with optical densities of 14.1 and 21.5 (15 µL liquid wax) were used to determine the cooling and heating rate depending on the injected current (Figure 3.8C).

3.3.4 Preparation of reaction mixtures for PPT-qPCR

Double-stranded circular form of the M13mp18 RF I DNA was purchased from New England BioLabs, Inc. and used as a template for the PPT-qPCR experiments. Forward primer (5`-TCC TCA AAG CCT CTG TAG CCG TTG CT-3`, 100 µM) and reverse primer (5`-GCT TGC AGG GAG TTA AAG GCC GCT T-3`, 100 µM) purified by HPLC were purchased from Integrated DNA Technologies and used without further purification. Forward and reverse primers were designed to amplify 100-nucleotides from the M13mp18 DNA sequence. KAPA2G

fast DNA polymerase (5 U μL^{-1}), KAPA2G buffer A (5×) and KAPA dNTPs mix (10 mM each) were purchased from KAPA Biosystems. SYBR® Green I and II (10,000×) were purchased from Molecular Probes, Inc. Quick-Load® purple low molecular weight DNA ladder, Quick-Load® purple 1 kb DNA ladder and gel loading dye (Purple, 6×) were purchased from New England BioLabs, Inc. Transparent PCR tube (0.2 mL 8-tube PCR strips without caps, low profile, clear, TLS0801) and cap (0.2 mL flat PCR tube 8-cap strips, optical, ultraclear, TCS0803) were purchased from Bio-Rad Laboratories. The reaction mixtures in Figure 3.13 contain 2 μL of 5× KAPA2G buffer A (1×), 0.2 μL of 10 mM dNTPs (0.2 mM each), 0.5 μL of 10 μM forward primers (0.5 μM), 0.5 μL of 10 μM reverse primers (0.5 μM), 0.4 μL of 5 U μL^{-1} KAPA2G fast DNA polymerase (0.2 U μL^{-1}), 0.5 μL of 20 ng μL^{-1} M13mp18 DNA template (1 ng μL^{-1}), 0.5 μL of 140× SYBR® Green I (7×), 5 μL of 36.6 OD PEG-Si-AuBPs in 2 % BSA (18.3 OD, 1% BSA). The concentrations in the brackets denote the final concentrations in 10 μL reaction volume. 0.4 μL of water was added to adjust the reaction volume to 10 μL, and 15 μL of Chill-out™ liquid wax was added on top of the mixture in conventional PCR tube. In Figure 3.11A, 0.5 μL of 60, 100, and 140× SYBR® Green I (3, 5, and 7×) were used, maintaining other reagents the same as in Figure 3.10. In Figure 3.11B, 5 μL of 28.2, 36.6 and 43.0 OD PEG-Si-AuBPs in 2% BSA (14.1, 18.3, and 21.5 OD, 1% BSA) were used, maintaining other reagents the same as in Figure 3.10. In Figure 3.13A, 0.5 μL of 100, 20, 2, 0.2 and 0.02 ng μL^{-1} M13mp18 DNA template (5, 1, 0.1, 0.01, and 0.001 ng μL^{-1}) were used, maintaining other reagents the same as in Figure 3.8. The PPT-qPCR was performed with thermocycling between 95 °C (0 s, denaturation) and 72 °C (2 s, annealing/extension) for 40 cycles. The reaction was monitored by measuring the fluorescent emission signals at 520 nm in real-time during the annealing/extension at 72 °C with 1 s of acquisition time. For the positive control (lane 1 in Figure 3.13C), the reaction mixture

used in Figure 3.10 without nanoparticles was used, and the 40 thermocycles of temperatures 95 °C for 5 s and 72 °C for 5 s were controlled with CFX96 Touch™ real-time PCR detection system, Bio-Rad Laboratories Inc. After the amplification, the solution was mixed with 3 μL of 6× loading buffer and 5 μL of 0.5× tris/borate/EDTA buffer (TBE buffer), and 5 μL of mixture was loaded and analyzed by electrophoresis with 3% agarose gel.

3.3.5 Preparation of reaction mixtures for PPT-qRCA

Quick Ligation™ Kit, isothermal amplification buffer (10×) and *Bst* 2.0 WarmStart® DNA polymerase (8 U L^1) were purchased from New England BioLabs, Inc. Phosphorylated linear RCA Template (5'-/5Phos/CAA GTA GTC GAG ATC ATT AGG ACC ACA GCG AAC AAT TAA CAC GAC CAA TCA TAC AGG TAC-3') and RCA splint primer (5'-CTC GAC TAC TTG GTA CCT GTA TGA-3') were obtained from Integrated DNA Technologies. For the preparation of circular DNA template, 0.1 μM 5'-phosphorylated linear RCA template and 0.3 μM RCA splint primer, and 1 μL of Quick T4 DNA ligase were mixed in 1× quick ligation reaction buffer (20 μL final volume) at 25 °C for 10 min. After ligation, the solution was incubated at 65 °C for 10 min to inactivate the T4 DNA ligase and then used as a stock solution. In PPT-qRCA, Figure 3.16, the reaction mixture contains 1 μL of 10× isothermal buffer (1×), 0.5 μL of 10 mM dNTPs (0.5 mM), 0.5 μL of 140× SYBR® Green II (7×), 1 μL of 8 U μL^{-1} of *Bst* 2.0 WarmStart® DNA polymerase, 2 μL of 2.5 OD PEG-Si-AuBPs in 5% BSA (0.5 OD, 1% BSA). The concentrations in the brackets denote the final concentrations in 10 μL reaction volume. 5, 2.5, 1, 0.5, and 0.25 μL of template stock solution including circular DNA (0.3 μM) and primer (100 μM) were used. 0, 2.5, 4, 4.5, and 4.75 μL of 0.3 μM primer were added to adjust the concentration of primer to 0.1 μM in 10 μL final reaction volume. For the PPT-qRCA assay, the fixed temperature of 55 °C for the isothermal extension was controlled with the IR-

LED. The SYBR® Green II intercalating dye was excited with the blue-LED and the fluorescent emission signals were collected every 30 s for 80 min at 520 nm. The injection current was set to 0.45 A. After the amplification, the product solution was mixed with 3 μL of 6× loading buffer and 5 μL of 0.5× TBE buffer. Then, 5 μL of the mixture was loaded and analyzed by electrophoresis in a 2% agarose gel.

3.3.6 Preparation of reaction mixtures for PPT-multi-enzyme restriction digestion

CutSmart® buffer (10×), pBR322 vector (1 mg μL^{-1}), EcoRI-HF® (20,000 U μL^{-1}), and SalI-HF® (20,000 U μL^{-1}) were purchased from New England BioLabs, Inc. For the restriction digest in Figure 3.19, the reaction mixture in a total final volume of 25 μL contains 16 μL of water, 2.5 μL of 10× CutSmart® buffer (1×), 0.5 μL of 1 mg μL^{-1} pBR322 Vector (20 μg μL^{-1}), 0.5 μL of 20,000 U μL^{-1} EcoRI-HF® (400 U μL^{-1}), 0.5 μL 20,000 U μL^{-1} of SalI-HF® (400 U μL^{-1}), 5 μL of 2.5 OD PEG-Si-AuBPs (5K PEG) in 5% BSA (0.5 OD, 1% BSA). The concentrations in the brackets denote the final concentrations in a 25 μL reaction volume. For the positive control with the CFX96 Touch™, the reaction mixture without nanoparticles was used while maintaining the same concentrations for the others reagents. For the PPT-multi-enzyme restriction digestion, the constant temperature of 37 °C for the activation of enzymes and 65 °C for the inactivation were controlled with the IR-LED (Injection current of 0.15 A was applied at 37 °C and 0.5 A for 65 °C). After the amplification, the solution was mixed with 5 μL of 6× loading buffer, and 10 μL of mixture was loaded and analyzed by electrophoresis in a 2% agarose gel.

3.4 References

1. Mullis, K. B.; Faloona, F. A., [21] Specific synthesis of DNA in vitro via a polymerase-catalyzed chain reaction. In *Methods in Enzymology*, Academic Press: 1987; Vol. Volume 155, pp 335-350.

2. Sano, T.; Smith, C. L.; Cantor, C. R., Immuno-Pcr - Very Sensitive Antigen-Detection by Means of Specific Antibody-DNA Conjugates. *Science* **1992,** *258* (5079), 120-122.

3. Kubista, M.; Andrade, J. M.; Bengtsson, M.; Forootan, A.; Jonák, J.; Lind, K.; Sindelka, R.; Sjöback, R.; Sjögreen, B.; Strömbom, L.; Ståhlberg, A.; Zoric, N., The real-time polymerase chain reaction. *Molecular Aspects of Medicine* **2006,** *27* (2–3), 95-125.

4. Heid, C. A.; Stevens, J.; Livak, K. J.; Williams, P. M., Real time quantitative PCR. *Genome Res* **1996,** *6* (10), 986-94.

5. Li, H.; Huang, J.; Lv, J.; An, H.; Zhang, X.; Zhang, Z.; Fan, C.; Hu, J., Nanoparticle PCR: nanogold-assisted PCR with enhanced specificity. *Angew Chem Int Ed Engl* **2005,** *44* (32), 5100-3.

6. Walker, G. T.; Fraiser, M. S.; Schram, J. L.; Little, M. C.; Nadeau, J. G.; Malinowski, D. P., Strand displacement amplification--an isothermal, in vitro DNA amplification technique. *Nucleic Acids Research* **1992,** *20* (7), 1691-1696.

7. Nilsson, M.; Malmgren, H.; Samiotaki, M.; Kwiatkowski, M.; Chowdhary, B. P.; Landegren, U., Padlock probes: circularizing oligonucleotides for localized DNA detection. *Science* **1994,** *265* (5181), 2085-8.

8. Little, M. C.; Andrews, J.; Moore, R.; Bustos, S.; Jones, L.; Embres, C.; Durmowicz, G.; Harris, J.; Berger, D.; Yanson, K.; Rostkowski, C.; Yursis, D.; Price, J.; Fort, T.; Walters, A.; Collis, M.; Llorin, O.; Wood, J.; Failing, F.; O'Keefe, C.; Scrivens, B.; Pope, B.; Hansen, T.; Marino, K.; Williams, K.; et al., Strand displacement amplification and homogeneous real-time detection incorporated in a second-generation DNA probe system, BDProbeTecET. *Clin Chem* **1999,** *45* (6 Pt 1), 777-84.

9. Tian, L.; Weizmann, Y., Real-Time Detection of Telomerase Activity Using the Exponential Isothermal Amplification of Telomere Repeat Assay. *J. Am. Chem. Soc.* **2013,** *135* (5), 1661-1664.

10. Zhao, Y.; Chen, F.; Li, Q.; Wang, L.; Fan, C., Isothermal Amplification of Nucleic Acids. *Chem Rev* **2015,** *115* (22), 12491-545.

11. Nie, S. P.; Roth, R. B.; Stiles, J.; Mikhlina, A.; Lu, X. D.; Tang, Y. W.; Babady, N. E., Evaluation of Alere i Influenza A&B for Rapid Detection of Influenza Viruses A and B. *Journal of Clinical Microbiology* **2014,** *52* (9), 3339-3344.

12. Chin, C. D.; Linder, V.; Sia, S. K., Commercialization of microfluidic point-of-care diagnostic devices. *Lab Chip* **2012,** *12* (12), 2118-34.

13. Yan, L.; Zhou, J.; Zheng, Y.; Gamson, A. S.; Roembke, B. T.; Nakayama, S.; Sintim, H. O., Isothermal amplified detection of DNA and RNA. *Molecular BioSystems* **2014,** *10* (5), 970-1003.

14. Almassian, D. R.; Cockrell, L. M.; Nelson, W. M., Portable nucleic acid thermocyclers. *Chem Soc Rev* **2013,** *42* (22), 8769-98.

15. Zhang, Y.; Ozdemir, P., Microfluidic DNA amplification--a review. *Anal Chim Acta* **2009,** *638* (2), 115-25.

16. Farrar, J. S.; Wittwer, C. T., Extreme PCR: Efficient and Specific DNA Amplification in 15–60 Seconds. *Clinical Chemistry* **2014,** *61* (1), 145.

17. Son, J. H.; Hong, S.; Haack, A. J.; Gustafson, L.; Song, M.; Hoxha, O.; Lee, L. P., Rapid Optical Cavity PCR. *Advanced Healthcare Materials* **2016,** *5* (1), 167-174.

18. Roche, P. J. R.; Beitel, L. K.; Khan, R.; Lumbroso, R.; Najih, M.; Cheung, M. C. K.; Thiemann, J.; Veerasubramanian, V.; Trifiro, M.; Chodavarapu, V. P.; Kirk, A. G., Demonstration of a plasmonic thermocycler for the amplification of human androgen receptor DNA. *Analyst* **2012,** *137* (19), 4475-4481.

19. Li, Z.; Wang, P.; Tong, L.; Zhang, L., Gold nanorod-facilitated localized heating of droplets in microfluidic chips. *Optics Express* **2013,** *21* (1), 1281-1286.

20. Walsh, T.; Lee, J.; Park, K., Laser-assisted photothermal heating of a plasmonic nanoparticle-suspended droplet in a microchannel. *Analyst* **2015,** *140* (5), 1535-1542.

21. Son, J. H.; Cho, B.; Hong, S.; Lee, S. H.; Hoxha, O.; Haack, A. J.; Lee, L. P., Ultrafast photonic PCR. *Light Sci Appl* **2015,** *4*, e280.

22. Link, S.; El-Sayed, M. A., Shape and size dependence of radiative, non-radiative and photothermal properties of gold nanocrystals. *Int. Rev. Phys. Chem.* **2000,** *19* (3), 409-453.

23. Lee, J. H.; Cheglakov, Z.; Yi, J.; Cronin, T. M.; Gibson, K. J.; Tian, B.; Weizmann, Y., Plasmonic Photothermal Gold Bipyramid Nanoreactors for Ultrafast Real-Time Bioassays. *J Am Chem Soc* **2017,** *139* (24), 8054-8057.

24. Webb, J. A.; Bardhan, R., Emerging advances in nanomedicine with engineered gold nanostructures. *Nanoscale* **2014,** *6* (5), 2502-2530.

25. Chou, C.-H.; Chen, C.-D.; Wang, C. R. C., Highly Efficient, Wavelength-Tunable, Gold Nanoparticle Based Optothermal Nanoconvertors. *J. Phys. Chem. B* **2005,** *109* (22), 11135-11138.

26. Lee, J. H.; Gibson, K. J.; Chen, G.; Weizmann, Y., Bipyramid-templated synthesis of monodisperse anisotropic gold nanocrystals. *Nat Commun* **2015,** *6*, 7571.

27. Navarro, J. R.; Lerouge, F.; Micouin, G.; Cepraga, C.; Favier, A.; Charreyre, M. T.; Blanchard, N. P.; Lerme, J.; Chaput, F.; Focsan, M.; Kamada, K.; Baldeck, P. L.; Parola, S., Plasmonic bipyramids for fluorescence enhancement and protection against photobleaching. *Nanoscale* **2014,** *6* (10), 5138-45.

28. Wu, W.-C.; Tracy, J. B., Large-Scale Silica Overcoating of Gold Nanorods with Tunable Shell Thicknesses. *Chem. Mater.* **2015,** *27* (8), 2888-2894.

29. Chen, Y.-S.; Frey, W.; Kim, S.; Homan, K.; Kruizinga, P.; Sokolov, K.; Emelianov, S., Enhanced thermal stability of silica-coated gold nanorods for photoacoustic imaging and image-guided therapy. *Opt. Express* **2010,** *18* (9), 8867-8878.

30. Steinberg, G.; Stromsborg, K.; Thomas, L.; Barker, D.; Zhao, C., Strategies for covalent attachment of DNA to beads. *Biopolymers* **2004,** *73* (5), 597-605.

31. Hu, M.; Wang, X.; Hartland, G. V.; Salgueiriño-Maceira, V.; Liz-Marzán, L. M., Heat dissipation in gold–silica core-shell nanoparticles. *Chem. Phys. Lett.* **2003,** *372* (5–6), 767-772.

32. Schneider, G.; Decher, G.; Nerambourg, N.; Praho, R.; Werts, M. H. V.; Blanchard-Desce, M., Distance-Dependent Fluorescence Quenching on Gold Nanoparticles Ensheathed with Layer-by-Layer Assembled Polyelectrolytes. *Nano Lett.* **2006,** *6* (3), 530-536.

33. Mayilo, S.; Kloster, M. A.; Wunderlich, M.; Lutich, A.; Klar, T. A.; Nichtl, A.; Kürzinger, K.; Stefani, F. D.; Feldmann, J., Long-Range Fluorescence Quenching by Gold Nanoparticles in a Sandwich Immunoassay for Cardiac Troponin T. *Nano Lett.* **2009,** *9* (12), 4558-4563.

34. Wu, W. C.; Tracy, J. B., Large-Scale Silica Overcoating of Gold Nanorods with Tunable Shell Thicknesses. *Chem Mater* **2015,** *27* (8), 2888-2894.

35. Hu, X.; Gao, X., Multilayer coating of gold nanorods for combined stability and biocompatibility. *Physical chemistry chemical physics : PCCP* **2011,** *13* (21), 10028-10035.

36. Abadeer, N. S.; Murphy, C. J., Recent Progress in Cancer Thermal Therapy Using Gold Nanoparticles. *The Journal of Physical Chemistry C* **2016,** *120* (9), 4691-4716.

37. Abadeer, N. S.; Brennan, M. R.; Wilson, W. L.; Murphy, C. J., Distance and plasmon wavelength dependent fluorescence of molecules bound to silica-coated gold nanorods. *ACS Nano* **2014,** *8* (8), 8392-406.

38. Heid, C. A.; Stevens, J.; Livak, K. J.; Williams, P. M., Real time quantitative PCR. *Genome Research* **1996,** *6* (10), 986-994.

39. Gudnason, H.; Dufva, M.; Bang, D. D.; Wolff, A., Comparison of multiple DNA dyes for real-time PCR: effects of dye concentration and sequence composition on DNA amplification and melting temperature. *Nucleic Acids Res.* **2007,** *35* (19), e127-e127.

40. Bustin, S. A.; Benes, V.; Garson, J. A.; Hellemans, J.; Huggett, J.; Kubista, M.; Mueller, R.; Nolan, T.; Pfaffl, M. W.; Shipley, G. L.; Vandesompele, J.; Wittwer, C. T., The MIQE Guidelines: Minimum Information for Publication of Quantitative Real-Time PCR Experiments. *Clin. Chem.* **2009,** *55* (4), 611-622.

41. Rutledge, R. G., Sigmoidal curve-fitting redefines quantitative real-time PCR with the prospective of developing automated high-throughput applications. *Nucleic Acids Res.* **2004,** *32* (22), e178.

42. Liu, W.; Saint, D. A., Validation of a quantitative method for real time PCR kinetics. *Biochem. Biophys. Res. Commun.* **2002,** *294* (2), 347-353.

43. Melzak, K. A.; Sherwood, C. S.; Turner, R. F. B.; Haynes, C. A., Driving Forces for DNA Adsorption to Silica in Perchlorate Solutions. *J. Colloid Interface Sci.* **1996,** *181* (2), 635-644.

44. Zhao, Y.; Chen, F.; Li, Q.; Wang, L.; Fan, C., Isothermal Amplification of Nucleic Acids. *Chem. Rev.* **2015,** *115* (22), 12491-12545.

45. Balbás, P.; Soberón, X.; Merino, E.; Zurita, M.; Lomeli, H.; Valle, F.; Flores, N.; Bolivar, F., Plasmid vector pBR322 and its special-purpose derivatives — a review. *Gene* **1986,** *50* (1–3), 3-40.

Chapter 4 – Proton-powered plasmonic actuator

4.1 Introduction

Self-assembly of nanoparticles was first reported in 1996 and since then advances in nanoparticle synthesis regarding shape, monodispersity, and yield, as well as DNA structural design and synthesis have presented numerous opportunities in the field of programmable self-assembly through the integration of the metal nanoparticles with DNA ligands[1-13]. Unfortunately, most self-assemblies of metal nanoparticles result in large aggregates or agglomerations as few methods exist to limit the amount of or location of the surface functionalization, resulting in full surface coverage and uncontrollable continuation of self-assembly[14-16]. Recently, it has been shown that the use of very specific DNA assemblies can be used to control how the nanoparticles are functionalized or assembled[17-19]. However, these methods require stoichiometrically large amounts of DNA relative to the nanoparticles and discrete size-matching of the DNA structure with the particles, making these methods purely academic. There is still a need for methods of site-specific functionalization that can lead to discrete nanoparticle self-assembly.

The creation of devices on the nanoscale represents a vastly unexplored potential in the scientific community. These nanomachines lie within a size-scale between that of molecular and bulk material and results in greatly different properties than either. Machinery on this size-scale has the potential for sensing, drug delivery, cargo payload, and much more, all of which could be done inside of a cell interacting with proteins or organelles. Much like a modern-day factory, fully autonomous cells could be synthesized entirely out of nanoscale machinery. However, this future depends on the incorporation of multiple materials into responsive and functional devices. One of the first steps to take would be in the creation of DNA-nanoparticle hybrid

nanomachines. Nanoparticles and optical molecules have been incorporated into DNA nanomachines in the past, but the isotropic nanoparticles typically employed only serve to aid in visualization through microscopy[20-21]. The use of anisotropic nanoparticles and the utilization of their unique shapes is a hurdle in self-assembly that currently limits most nanomachines.

The use of DNA as a material in nanoparticle self-assembly allows for programmability and specificity unmatched by other ligands. In fact, DNA has at least seven advantageous features that make it a suitable candidate as a building block for nanotechnology[22-23]. (1) The well-defined double helix structure of DNA makes the design predictable with atomic precision. In solution, dsDNA normally exists in B-form, which is a right-handed helix with a diameter of 2.0 nm, 10.5 base pairs per full turn of helix, 3.4 Å per base pair rise (and therefore, one full turn of double helix is about 3.6 nm). (2) The specific Watson-Crick base pairing interactions (A=T and G≡C) provide invaluable tools for programmable and controllable designs. An N-base DNA strand has the diversity of 4^N different sequences and base pairings also provide the constructing tools of hairpin, sticky ends and junction structures. (3) The rigidity of dsDNA (with persistence lengths up to 50 nm) makes it an ideal building block for nanostructures. (4) The solid phase phosphoramidite-based synthesis of oligonucleotides makes the DNA easily and cheaply prepared and commercially available. Furthermore, various linkers, modified bases, fluorescent dyes and other molecules can be conveniently and readily incorporated to give the functionalized DNA. (5) The enzymatic and experimental tools developed by molecular biology can be directly used by DNA nanotechnology. Various enzymes (such as diverse restriction enzymes, nicking enzymes, ligases, exonucleases, polymerases, kinases, etc.) and the technology (for example gel electrophoresis and foot-printing) can be exploited for the construction, purification and validation of the structures. (6) A diverse library of DNA-binding molecules such as proteins,

intercalating dyes, and PNA have been developed and used for assisting DNA-base nanotechnology. (7) Certain sequences can form non-B-form structures such as left-handed Z-form double helix, triplex, G-quadruplex, *i*-motif and other sequences which have been selected to be folded into DNAzymes and aptamers. All of these structures greatly expand the spectrum and functionalization of DNA-based nanostructures, including the construction of synthetic DNA topologies[24-27]. Due to these unique properties of DNA, materials responsive to external stimuli can also be created[11, 13]. The use of stimuli-responsive materials is an important step in creating nanomachinery, and DNA-nanoparticle hybrid systems represent the most promising prospect for the future of nanomachinery[9, 28]. Therefore, it remains critical for advances to be made in creating discrete self-assemblies of nanoparticles, especially those involving stimuli-responsive materials.

This chapter will summarize a method to functionalize both isotropic and anisotropic gold nanoparticles in a site-specific manner with different DNA strands, each encoded with part of a triple helix moiety. The strands contain an additional complementary segment separate from the triple helix sequences that allows them to hybridize, effectively tethering two nanoparticles into discrete dimers regardless of pH. When the conditions of the solution are changed between acidic and basic, the triple helix closes and opens, respectively, which changes the interparticle distance, and elicits a plasmonic coupling, resulting in a shift of the UV-Vis-NIR absorbance peak. In the case of the gold nanosphere dimer, the plasmonic coupling shift results in a color change that is visible by eye. Because the nanoparticle-DNA hybrid building blocks are universal, both homodimers and heterodimers can be assembled from the nanospheres and nanorods. We demonstrate that the triple-helix response to pH is fast-acting and completely reversible for several cycles. This approach presents a method for creating universal building

blocks for nanoparticle self-assembly capable of creating discrete, novel, and interesting structures that allow for future study of nanoparticle-nanoparticle interactions and nanoparticle-DNA hybrid nanomachinery.

4.2 Results and Discussions

4.2.1 Particle encapsulation

Here we describe a method of partial polymer encapsulation and subsequent DNA functionalization to create discrete homo- and heterodimers from spherical gold nanoparticles and gold nanorods, which can then be used to create a stimuli-responsive material that elicits a distance-dependent optical response. The DNA strands include sequences necessary for a triple-helix motif that responds to solution pH, causing the structures to exhibit a shift in the UV-Vis-NIR absorption peak caused by the plasmonic coupling of the nanoparticles. The reversible and consistent shifts in the absorbance peak vary with the make-up of the dimer pair and reach a maximum peak-shift with the nanorod dimer of 80 to 90 nm with each pH shift. The synthetic approach to create these functionalized nanoparticles represents a universal approach to site-specific and anisotropic directionality in self-assembly. This hybrid DNA-nanoparticle system represents a promising early step in the development of stimuli-responsive nanomachinery.

The gold nanorods were synthesized with dimensions of 49 nm in length and 12 nm in width with an aspect ratio of ~4.1 (Figure 4.1A)[4]. The purchased gold nanospheres were measured as 22.1 nm in diameter. The gold nanoparticles and gold nanorods undergo minor spectral changes upon the partial encapsulation and again with the subsequent DNA functionalization (Figure 4.1B and Figure 4.2). These small shifts can be attributed to changes to the dielectric constant of the immediate surroundings by the ligands and polymer, and these are similar to other measured shifts of ligand exchanges[29-30].

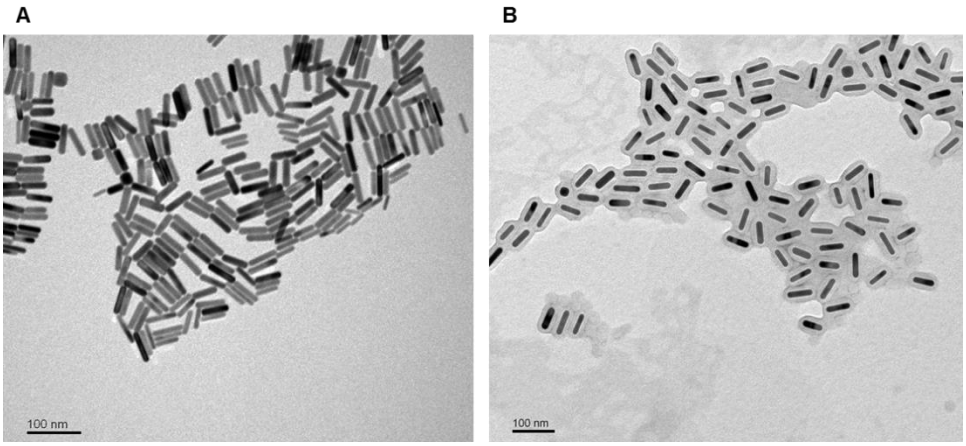

Figure 4.1 Bare AuNPs A) TEM image of the synthesized AuNPs with length: 48.6 ± 3.8 nm, width: 11.8 ± 1.3, and aspect ratio: 4.1 ±0.5 nm. B) TEM image of fully encapsulated AuNRs

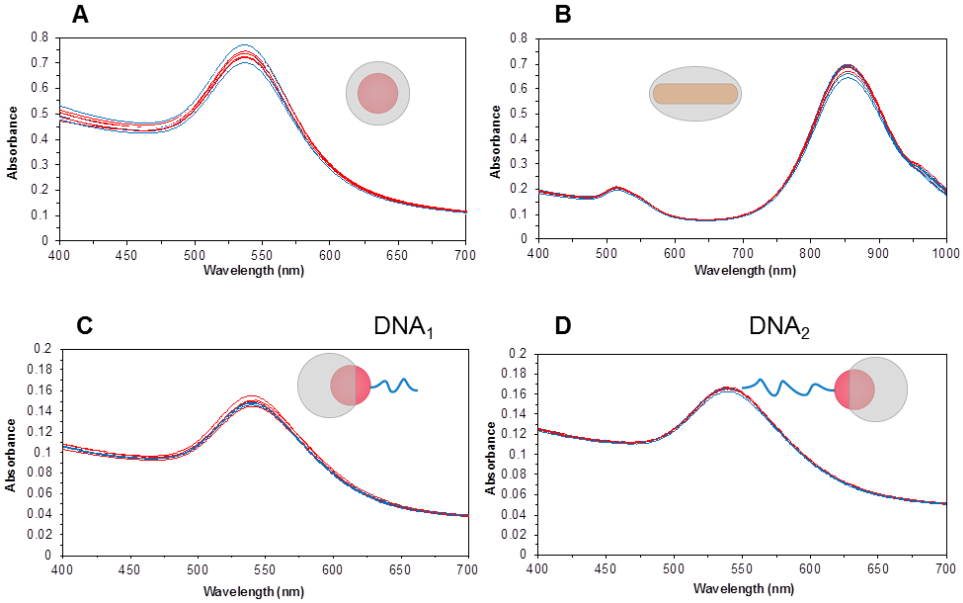

Figure 4.2 UV-Vis of the fully encapsulated and DNA-labeled partially encapsulated AuNPs A) Fully encapsulated AuNPs. B) Fully encapsulated AuNRs. C) Partially encapsulated AuNPs labeled with DNA strand (1). D) Partially encapsulated AuNPs labeled with DNA strand (2). For A and B, blue lines represent bare particles and red lines represent encapsulated particles. For C and D, blue lines represent partially encapsulated particles and red lines represent DNA-labeled particles

We optimized a method of partial polymer encapsulation of gold nanoparticles and nanorods to limit the amount of exposed area to small patch of surface. The eccentric encapsulation of gold nanoparticles (eNP) as well as encapsulation of nanorods with both ends exposed (2eNRs) have been previously reported[31-32]. The encapsulation of the nanoparticles was optimized to limit

the amount of area exposed so that hybridization with multiple nanoparticles could not occur, but enough surface area was still allowed so that there would be no steric hindrance of the triple helix folding from the polymer. Gold nanorods were eccentrically encapsulated so that only one end was exposed from the polymer shell (1eNR), through a method that demonstrated by our group recently for the first time[33]. This encapsulation ensures that any further surface modification can only occur at the tip of the nanorod and is limited to the exposed tip (Figure 4.3).

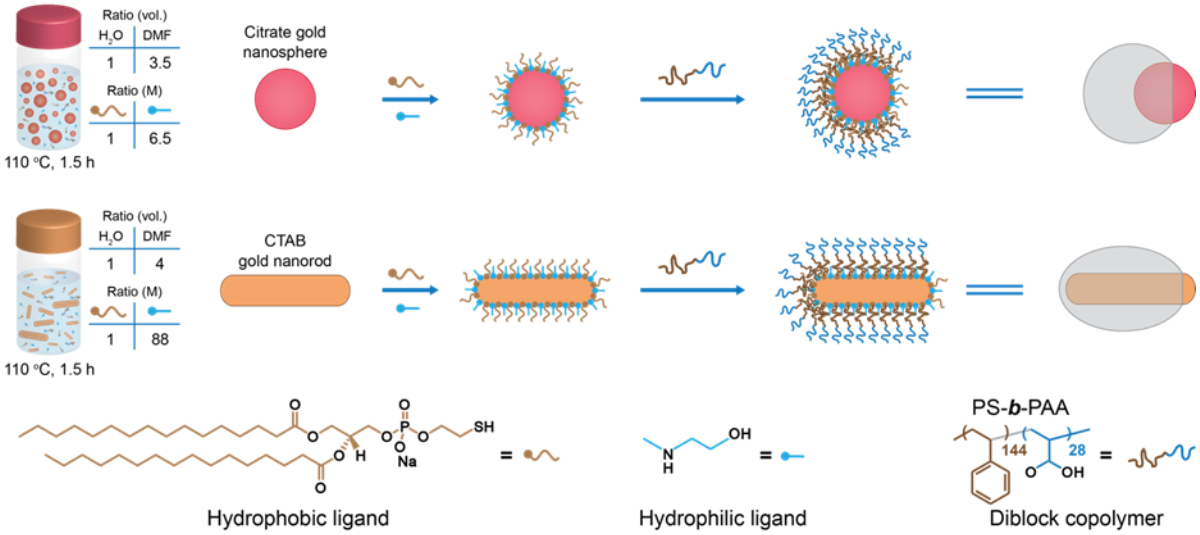

Figure 4.3 Schematic depicting the partial encapsulation of the AuNPs and AuNRs

Although the specifics of this process are beyond the scope of this work it can be summarized briefly as follows. The polymer encapsulation works by performing a ligand exchange with a specific ratio of a hydrophobic ligand (1,2-Dipalmitoyl-*sn*-glycero-3-phosphothioethanol, PSH) and a hydrophilic ligand (2-(methylamino)ethanol) in the presence of the block copolymer (Poly(styrene-b-acrylic acid), 15-b-1.6, PSPAA) in a DMF:H_2O solvent. When heated to 110 °C, a ligand exchange process occurs, coating the nanoparticle in a ratio of the two ligands. This ratio is tunable around the ratio of DMF:H_2O in the solution as well as the

ratio of the two ligands. The PSPAA micelles melt at such extreme temperatures, and then begin to reform around the nanoparticles, which are partially coated in hydrophobic ligands. The long hydrophobic polystyrene segments are directed toward the interior of the micelle, placing the hydrophilic poly-acrylic acid chains on the exterior. Because of the nature of the two ligands on the surface, only part of the nanoparticle is encapsulated in the polymer[33]. The particle size must be approximately equal to the size of the micelle for good coverage.

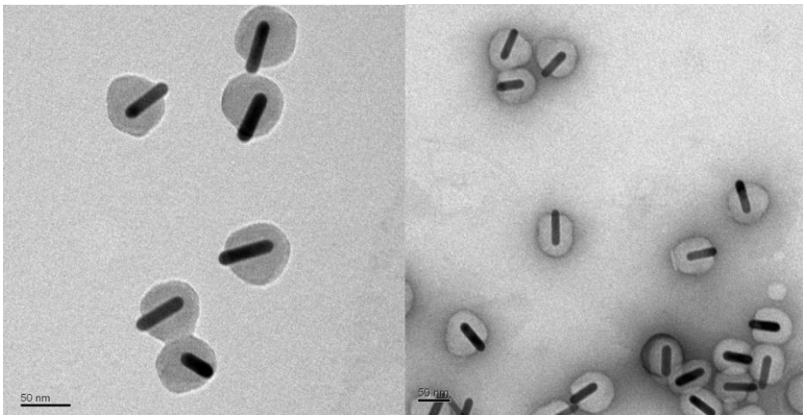

Figure 4.4 1-end exposed AuNRs Representative TEM images of the 1eNR building blocks. Scale bars = 50 nm.

4.2.2. Nanoparticle functionalized with triple helix DNA

Once the building blocks were obtained through partial encapsulation, further functionalization was performed using thiolated DNA strands. The DNA sequences were designed to include one entirely complementary segment that would remain hybridized throughout the assembly and pH-switching in addition to multiple segments from both strands that could form a triple helix at the proper pH. Since the DNA remains at least partially hybridized at all times, the particles will be permanently tethered to one another, allowing the triple helix portion of the DNA to rapidly respond to any changes in the solution pH. As seen in Figure 4.5, in neutral or basic conditions, the triple helix remains in the "open" conformation. In

this state, the particles remain far enough apart that very little or no plasmonic coupling occurs, and the absorbance spectrum most closely reflects the spectrum of the monomeric particle.

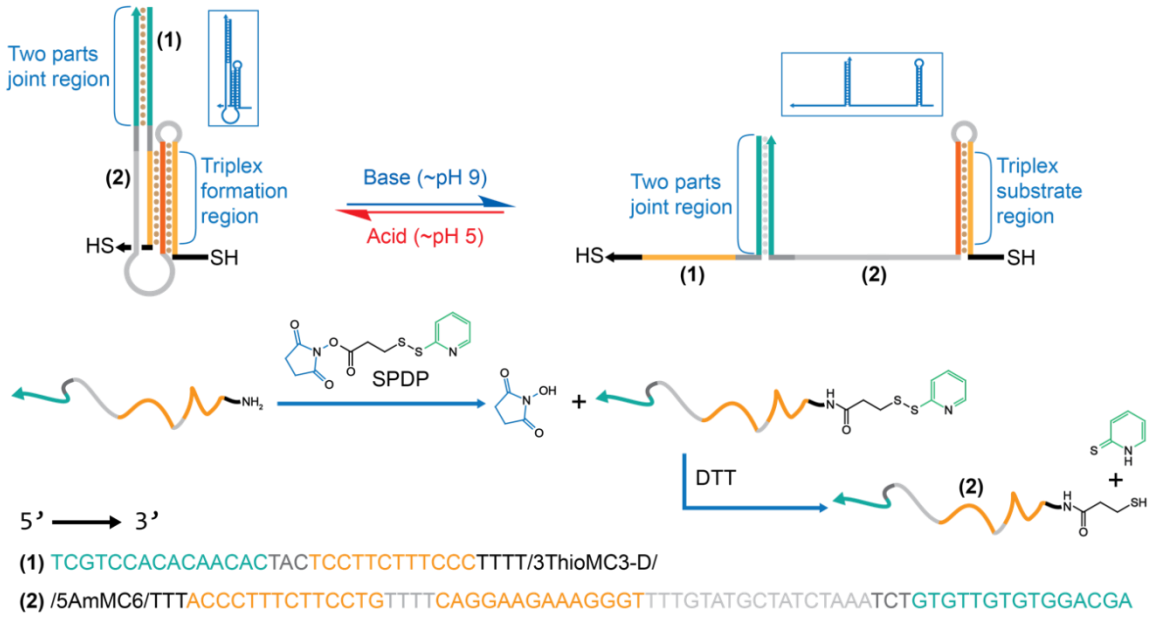

Figure 4.5 Scheme depicting the structure of the DNA triple helix and its reversible dsDNA state Under acidic conditions the triplex region will be in the "closed" position. Under basic conditions, only the normal dsDNA will be hybridized. DNA strand (1) will have a Thiol cap at its 3'-end. The DNA strand (2) will be labeled with 5'-amine cap and reacted with SPDP to yield the amide. DTT then reduces this compound to the thiol.

By lowering the pH of the solution to ~5, the protonation of N-3 position of the cytosines allows for Hoogsteen base pairing along the entirety of the triple helix sections, thus forming the "closed" conformation ( ). The additional T*A=T triplexes help stabilize the formation of the triplex. The ratio of these two sets of (C^+*G≡C and T*A=T) determines the pH range across which the sequence is responsive[11]. When the DNA is in the closed conformation, the particles are brought within range for plasmonic coupling to occur, causing a spectral shift of the relevant absorbance peak. These plasmonic peak shifts have been well studied and have become the basis for plasmonic rulers[34]. The pH range that the triple helix responds to is tunable through a wide range[11]. The pH range for our system was selected to respond close to neutral and biologically

relevant conditions. In addition, low pH was avoided because the exterior of the polymer shell is negatively charged, and acidic conditions could neutralize this shell and cause the nanoparticles to aggregate in solution. The polymer shell was shown to be stable at pH 4.5 and above (Figure 4.7A), meaning the nanoparticle shells will be stable at the pH range that was selected.

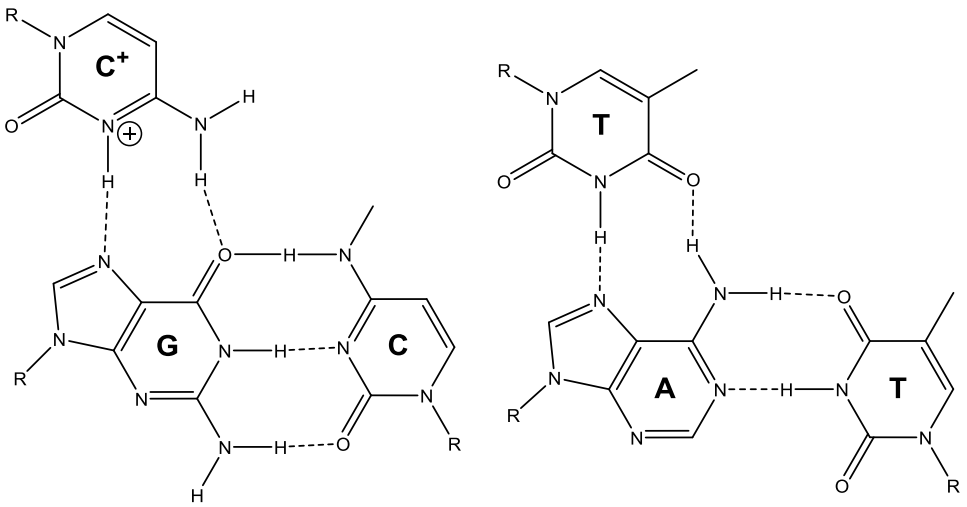

Figure 4.6 Hoogsteen Triple Helix Interactions Left: C^{+}*G≡C is the pH-responsive triplex formation. Right: T*A=T triplex does not require protonation.

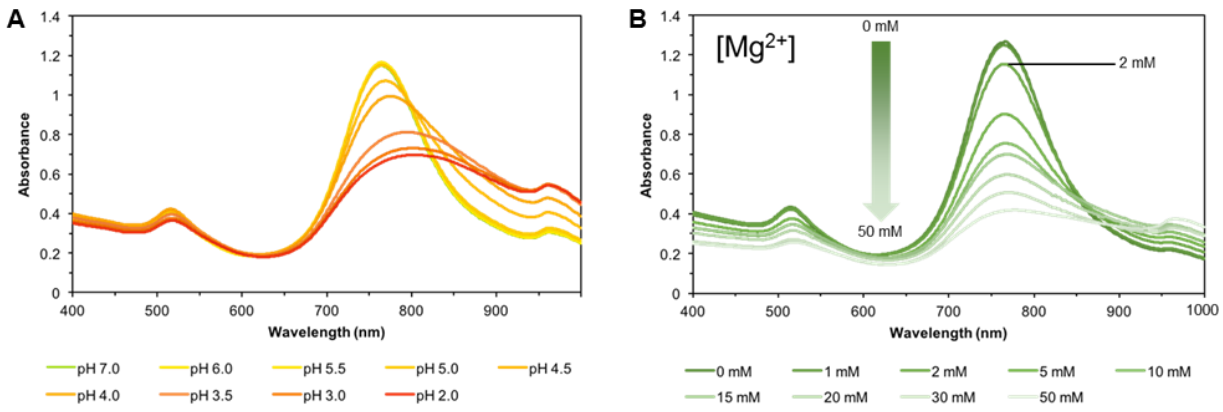

Figure 4.7 Stability of fully encapsulated AuNRs A) UV-Vis analysis in solutions at different pHs. B) UV-Vis analysis in solutions of different concentrations of $[Mg^{2+}]$.

A modified salt aging procedure was performed to load the DNA onto the exposed surfaces of the gold nanoparticles[35]. Because a large excess of DNA relative to particle is used in addition to the salt aging, equilibrium drives the ligand exchange process to favor the thiolated DNA

strands occupying the surface[33]. The nanoparticles were purified from the excess DNA and salt by repeated centrifugation. Hybridization of the surface DNA was performed by heating the solution to 45 °C for 15 min followed by cooling at a rate of 1 °C min^{-1}. The buffer was chosen to include a high concentration of NaCl to stabilize the compact packing of the folded triple helix DNA[16]. Mg^{2+} was found to cause irreversible aggregation of the poly-anionic polymer shells (Figure 4.7) and was therefore not used in the buffer.

4.2.3 Nanoparticle dimerization and pH-induced switching

Once the DNA is hybridized, discrete dimers of the nanoparticles are easily accessible, as seen in Figure 4.8**.** Due to the simplicity and design of the building blocks, eNP-eNP and 1eNR-1eNR homodimers, as well as eNP-1eNR heterodimers can be assembled with the universal materials.

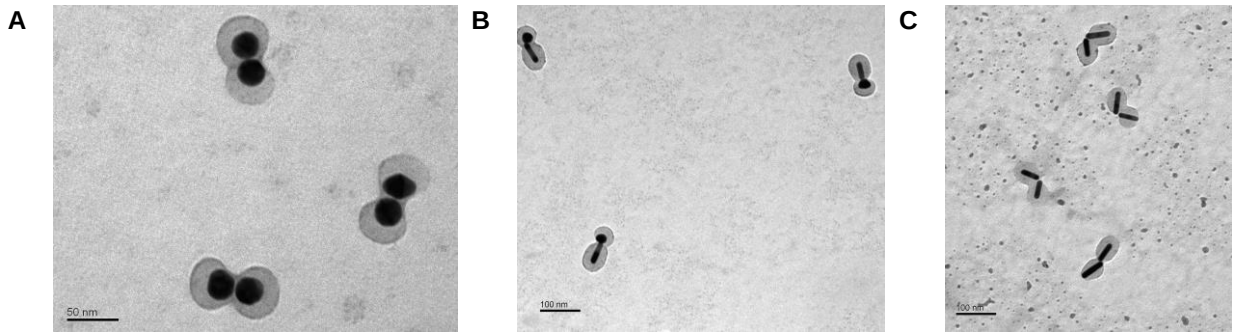

Figure 4.8 Representative TEM images of the nanoparticle dimers A) eNP-eNP homodimers. B) 1eNR-1eNR homodimers C) eNP-1eNR heterodimers (Scale bar is 50 nm for A and 100 nm for B and C)

With the nanoparticle dimers functionalized with the triplex-capable DNA, pH switching experiments were performed and measured by UV-Vis-NIR spectroscopy to observe the induced plasmonic coupling caused by the change in the inter-particle distance. In acidic conditions, the triplex folds, bringing the nanoparticles close together and inducing the plasmonic coupling. In

basic conditions, the triplex unfolds allowing the DNA to open back up. The distance between the nanoparticles when the DNA is in the open conformation is on the order of the nanoparticle diameter, large enough to minimize any plasmonic coupling and causing the UV-Vis-NIR absorbance peak to closely resemble that of the nanoparticle monomers.

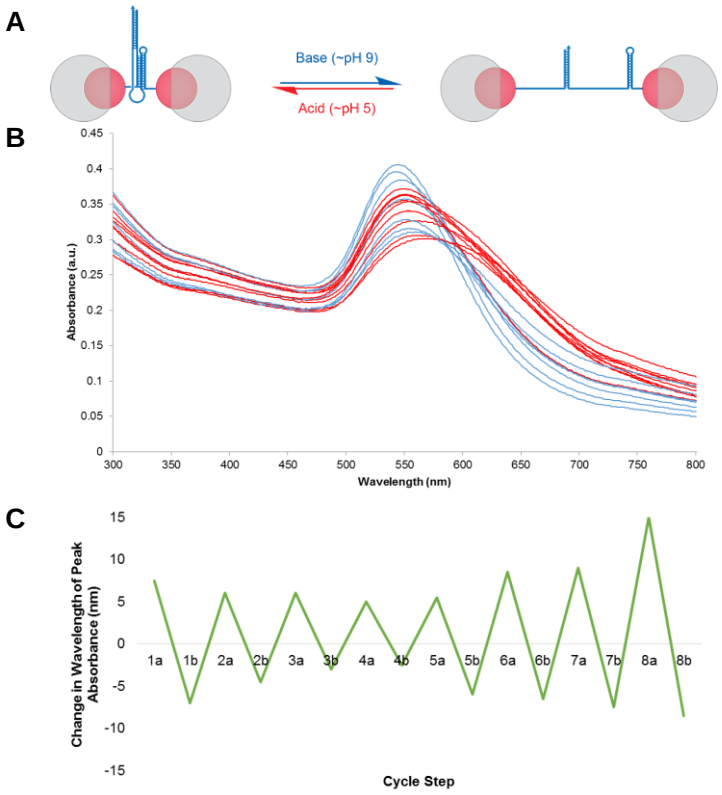

Figure 4.9 eNS-eNS Homodimer A) Schematic illustration of eNS-eNS homodimer actuator. B) UV-Vis of actuator in cycling environments. Blue represents pH = 9; Red pH = 5. C) Graph of the peak absorbance from the UV-Vis data of the actuator as it proceeds through the different cycle steps. The number represents the cycle round; A represents pH = 5; B represents pH = 9.

The gold nanosphere dimers (Figure 4.9**)** demonstrate reversible and consistent responses to changes in pH. The dimers are assembled and show to have an initial absorbance peak at 542 nm, which in neutral pH has the DNA in the open conformation. Addition of acid to the solution results in consistent shifts of the absorbance peak of three to four nanometers as well as increased absorbance as exemplified by the broadening on the red side of the absorbance peak.

The changes in the absorbance peak, although small, result in a visible color change. The closed conformation present in acidic presents as a red-purple color while the open conformation in basic conditions is a pink color, similar to the bare gold nanoparticles (Figure 4.10**)**

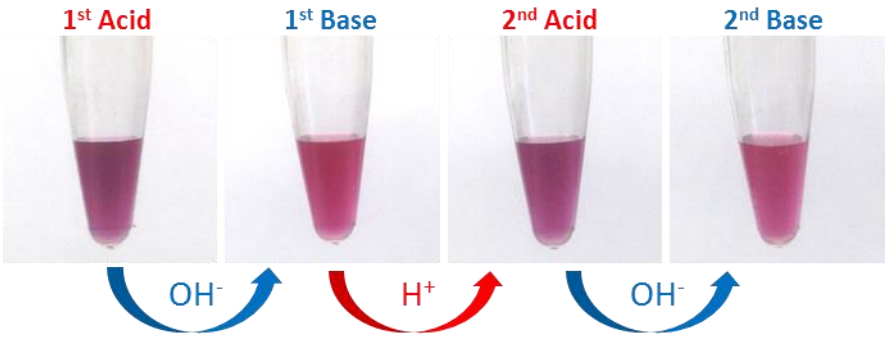

Figure 4.10 Photographs of solution containing AuNP dimers cycling through acidic and basic conditions

The sphere-rod heterodimers (Figure 4.11**)** show a difference in the peak shift in both size and location in the absorbance spectrum. Because the gold sphere is localized to the tip of the gold nanorod, the plasmonic coupling shifts the longitudinal peak of the rod. The initial longitudinal absorbance peak is located at 837 nm, and the pH switches show consistent peak shifts between eight and ten nanometers (Figure 4.11C), over double the shift observed in the sphere dimers. The absorbance peak corresponding to both the gold spheres and transverse peak of the nanorods exhibits little change resulting from the pH switches, and in fact continues to be located around 542nm, which is consistent with the previous result. The majority of light waves passing through the nanosphere are unaffected by the proximity of the nanorod. Only light waves passing through both the nanosphere and the long axis of the nanorod are affected by the plasmonic coupling.

The gold nanorod homodimers (Figure 4.12**)** exhibit the most dramatic shifts in absorbance peak. The initial longitudinal absorbance peak is located at 854 nm, which shifts to 941 nm upon

addition of acid the first time. Reversible pH switches result in peak shifts of 70 to 90 nm consistently (Figure 4.12). Again, only the light waves traveling through the longitudinal axis of the nanorod are affected by the proximity of the other nanorod, and thus the only absorbance shifts occur in that region of the spectrum. No observable shift occurs in the transverse peak of the spectrum, further confirming that all nanorods are linked by the tips and not through the sides.

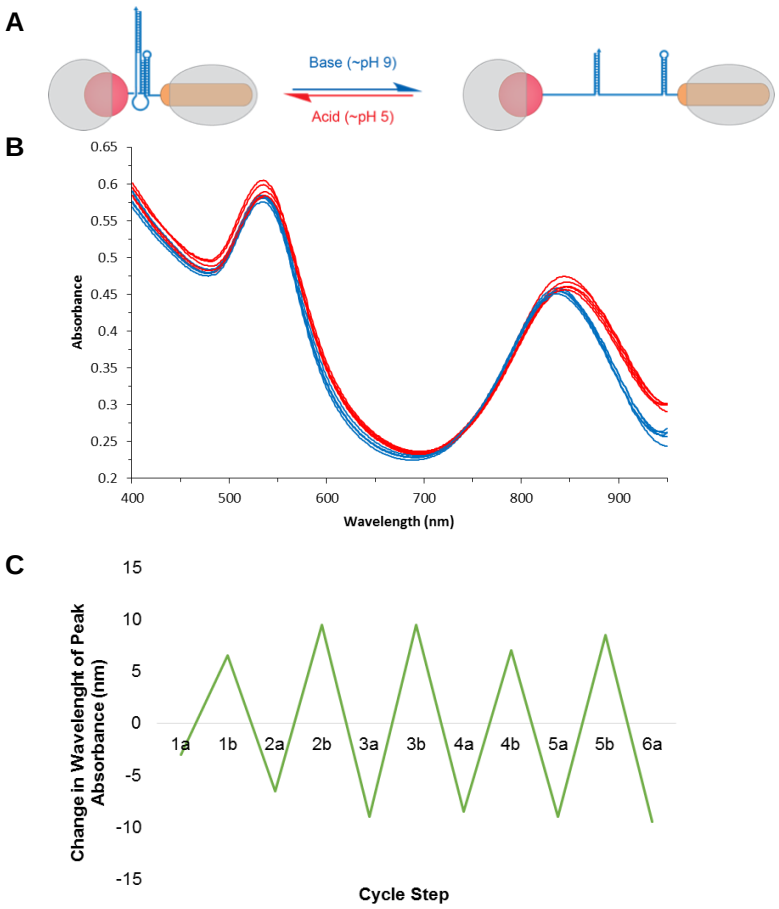

Figure 4.11 eNS-eNR heterodimer A) Schematic illustration of eNS-eNR heterodimer actuator. B) UV-Vis of actuator in cycling environments. Blue represents pH = 9; Red pH = 5. C) Graph of the peak absorbance from the UV-Vis data of the actuator as it proceeds through the different cycle steps. The number represents the cycle round; A represents pH = 5; B represents pH = 9.

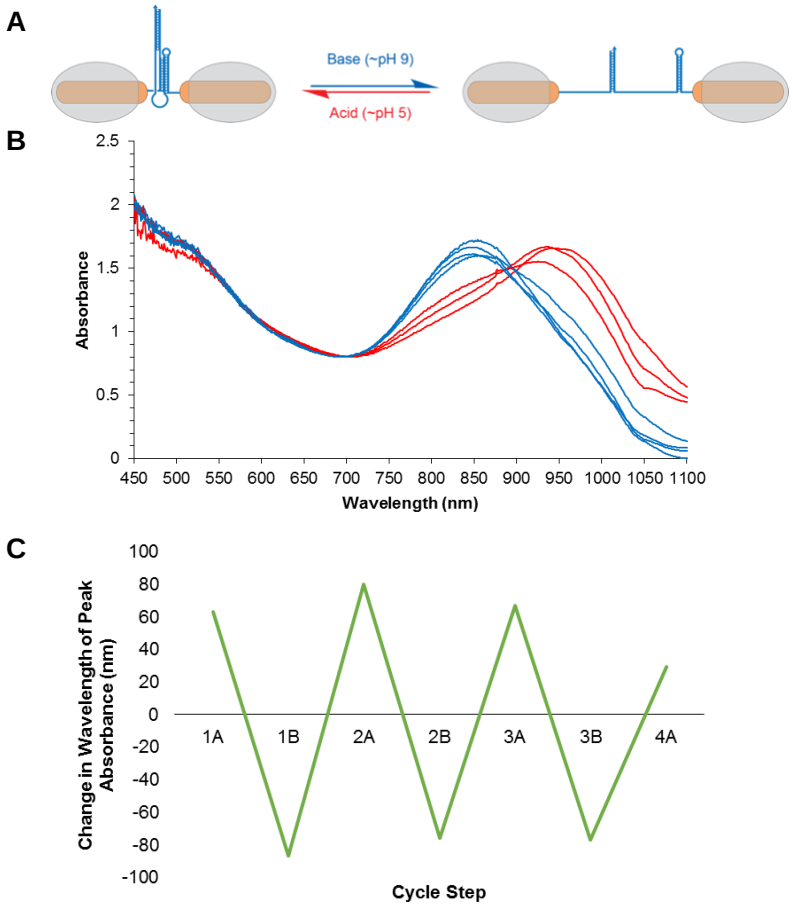

Figure 4.12 eNR-eNR homodimer actuator A) Schematic illustration of eNR-eNR homodimer actuator. B) UV-Vis of actuator in cycling environments. Blue represents pH = 9; Red pH = 5. C) Graph of the peak absorbance from the UV-Vis data of the actuator as it proceeds through the different cycle steps. The number represents the cycle round; A represents pH = 5; B represents pH = 9.

The rate of the triple helix switching was also measured using UV-Vis-NIR absorbance with the eNR homodimer. The absorbance values at the two longitudinal peak wavelengths were measured at 5 second intervals following the addition of either acid or base (Figure 4.13). The absorbance of one peak acts inversely to the absorbance of the other. The rate of the base-to-acid switch was found to be noticeably faster than the acid-to-base switch, 61 seconds compared to 103 seconds for the latter (Figure 4.13). This discrepancy has been observed with other triple

helix systems, however our nanoparticle-DNA hybrid system shows a considerably slower rate than the DNA alone[13].

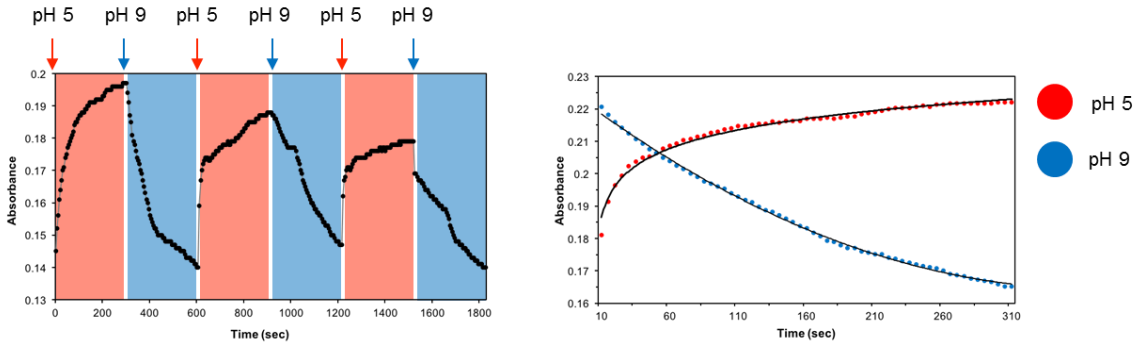

Figure 4.13 Rates of Interconversion between closed and open states Left: Real-time UV-Vis data measuring absorbance after addition of acid or base. Plotted rate kinetics of the conversion from open to closed (red) and closed to open (blue).

We believe this can attributed to the payload of the nanoparticles tethered to the ends of the DNA. Rather than simply waiting for the Brownian motion of the DNA strands to move close enough to form the triple helix, the nanoparticles have to move close enough together to allow the DNA strands to be in proximity to then form the correct conformation, which can take a couple orders of magnitude longer in this case[13]. However, it should be noted that the rate of the triple-helix DNA-nanoparticle hybrid system is still much faster than hybrid systems employing other DNA motifs, such as the i-motif[36].

4.3 Conclusions

We have demonstrated a new synthetic strategy for the creation of discrete nanomachine dimers, including the localization of spherical gold nanoparticles and gold nanorods to the tip of another gold nanorod. This was accomplished by a partial encapsulation process using a diblock copolymer in the presence of both a hydrophobic and a hydrophilic ligand. The exposed surfaces remaining on the partially encapsulated nanoparticles were then functionalized with DNA

sequences coded with a pH-responsive triple-helix moiety. With the nanoparticle homo- and heterodimers, the optical response to the plasmonic coupling, as controlled by the solution pH, was measured with UV-Vis-NIR spectroscopy. Highly reversible and consistent peak shifts were observed in the sphere dimers, the rod dimers, and the sphere-rod heterodimer with the largest peak shifts of 80-90 nm being present in the nanorod homodimer. The partial encapsulation method enabling site-specific functionalization and discrete self-assembly will allow future studies of nanoparticle interactions, including field enhancement effects and plasmonic coupling between different noble metals and quantum dots.

4.3 Experimental Section

4.3.1 Materials and Instruments

All chemicals were purchased from commercial suppliers and used without further purification. Benzyldimethylhexadecylammonium chloride (BDAC, cationic detergent), cetyl-trimethylammonium bromide (CTAB, Bioxtra, ≥99.0%), citric acid trisodium salt dehydrate (≥99.5%, BioUltra, for molecular biology), ethanol (200 proof, ACS reagent, ≥99.5%), hydrogen tetrachloroaurate thrihydrate ($HAuCl_4 \bullet 3H_2O$, ≥99.9%), L-ascorbic acid (Bioxtra, ≥98.0%), sodium chloride (NaCl, Bioxtra, ≥99.5%), sodium dibasic phosphate (Na_2HPO_4, Bioxtra, ≥99.0%), sodium dodecyl sulfate (SDS, Bioxtra, ≥99.0%), sodium monobasic phosphate monohydrate ($NaH_2PO_4 \bullet H_2O$, Bioxtra, ≥99.5%) were purchased from Sigma-Aldrich. Silver nitrate ($AgNO_3$, ≥99.8%) and sodium borohydride ($NaBH_4$, ≥99%) were purchased from Fluka. Hydrochloric acid (HCl, 1N) and sodium hydroxide (NaOH, pellets, ≥97.0%) were purchased from Fisher Scientific. 30 nm unconjugated gold nanoparticles were purchased from Ted Pella (CA, USA). N,N-Dimethylformamide (DMF, ≥99.8%) was purchased from Macron Fine

Chemicals. DL-1,4-Dithiothreitol (DTT, ≥99%) and 2-(methylamino)ethanol (≥99.0%) was purchased from Acros. 1,2-Dipalmitoyl-*sn*-glycero-3-phosphothioethanol (PSH, powder, ≥99.0%) was purchased from Avanti Polar Lipids. Succinimidyl 3-(2-pyridyldithio)propionate (SPDP) was purchased from ThermoFisher Scientific. The polystyrene-polyacrylic acid block copolymers were purchased from Polymer Source. All DNA sequences were purchased through Integrated DNA Technologies (IA, USA). Nap-5 DNA purification columns were purchased from GE Healthcare Life Sciences. MWCO 3 kDa was obtained from Pall Corporation. 50× Tris/Acetic Acid/EDTA buffer was purchased from Bio-Rad. Nano-pure water (18.2 MΩ, Barnstead Nanopure, Thermo Scientific, MA, USA) was used in all experiments. All glassware was cleaned before use using freshly prepared aqua regia (HCl:HNO_3 in a 3:1 ratio by volume) followed by rinsing with copious amounts of water.

UV-Vis-NIR spectra were obtained through either a Synergy H4 microplate reader (Biotek, VT, USA) or a Cary 5000 UV-Vis-NIR spectrophotometer (Agilent, CA, USA). Formvar/carbon-coated copper grids (Ted Pella, Inc., CA, USA) and *holey carbon grid for cryo-EM*. Tecnai G2 Spirit (FEI, OR, USA) was used to obtain all TEM images.

4.3.2 Synthesis of gold nanorods

The gold nanorods were synthesized according to previous literature reports[4]. Briefly, gold seeds were prepared with 5 mL of 100 mM CTAB, 127 μL of 10 mM $HAuCl_4$, and 300 μL of 10 mM $NaBH_4$. The solution was stirred gently for 10 mins and then allowed to sit at 30 °C for 1 h. Then, to a 20 mL scintillation vial was added 9.8 mL of 100 mM CTAB, 10 μL of freshly prepared 100 mM $AgNO_3$, 508 μL of 10 mM $HAuCl_4$, 55 μL of freshly prepared 100 mM ascorbic acid, and 12 μL of the seed solution. The solution was mixed gently and then stored at

30 °C overnight. The resulting brown solution was centrifuged twice at 10,000*g* for 15 mins and washed with 1 mM CTAB. The resulting gold nanorods were characterized by UV-Vis-NIR spectroscopy and TEM.

4.3.3 Encapsulation of gold nanorods

To encapsulate gold nanorods, a stock solution of OD~8 was used. To a 4 mL glass vial, 670 μL of DMF, 80 μL of 8 mg mL^{-1} PSPAA dissolved in DMF, 75 μL of AuNR solution, 100 μl of nanopure H_2O, 7 μL of 1.0 M 2-(methylamino)ethanol in H_2O, and 50 μL of 2 mg mL^{-1} solution of PSH dissolved in ethanol were added sequentially. The DMF/H_2O ratio used is 4.0:1, and the hydrophilic/hydrophobic ligand ratio used is 95:1. The reagents were added dropwise with a pipet at a rate of one drop every 2-3 seconds. The contents of the vial were vortexed while adding. The vial was sealed with Teflon tape to prevent any leaks during heating. The contents of the vial were then heated in an oil bath at 110 °C for 90 min. The resulting solution was then removed from the heat and allowed to cool to room temperature. The solution was then centrifuged twice at 9,000 *g* for 10 min and rinsed with 0.01% SDS, pH = 9 buffer.

4.3.4 Encapsulation of gold nanoparticles

To encapsulate gold nanoparticles, a purchased stock solution of 30 nm gold nanoparticles was used. To a 4 mL glass vial, 670 μL DMF, 80 μL of 8 mg mL^{-1} PSPAA dissolved in DMF, 210 μL of gold nanoparticles in H_2O, 4.5 μL of 0.1 M 2-(methylamino)ethanol in H_2O, and 50 μL of 2 mg mL^{-1} solution of PSH dissolved in ethanol were added sequentially. The reagents were added at a rate of a drop every couple of seconds and the contents of the vial were vortexed while adding. The vial was sealed with Teflon tape to prevent any leaks during heating. The contents of the vial were heated at 110 °C for 90 min. The resulting solution was then removed

from the oil bath and allowed to cool to room temperature. The solution was then centrifuged twice at 10,000 *g* for 15 min and rinsed with 0.01% SDS, pH = 9 buffer.

4.3.5 Synthesis of thiolated DNA

To a 600 μL tube, 50 μL of DMF, 0.312 mg of SPDP was added to form a 20 mM stock solution. 30 μL of a 100 μM stock solution of the DNA(1) was added 15 μL 20 mM SPDP solution. The solution was left to sit at room temperature for 30 mins. The thiolated DNA was then purified with a centrifugal filter tube (3kDa MWCO) and centrifuged at 5000 *g* for 12 minutes and rinsed with disulfide cleavage buffer, pH = 8. This was repeated two more times. Newly-thiolated DNA (1) was then immediately used in the subsequent steps.

4.3.6 Reduction of the thiolated DNA

The DNA was purchased with a terminal disulfide modification or was prepared as above. To 30 μL of a 100 μM stock solution of the DNA was added 30 μL of a freshly prepared 100 mM solution of DTT in nanopure H_2O. The solution was wrapped in foil and gently shaken at room temperature for 1 h. The reduced DNA was then purified in a NAP5 column with the fractions collected in a 96-well plate. The absorbance measured at 260 nm was used to determine the fractions containing the DNA.

4.3.7 Functionalization of the nanoparticles with thiolated DNA

To a concentrated solution of the partially encapsulated gold nanoparticles was added an amount of the reduced thiolated DNA in an amount where the DNA:nanoparticle ratio was roughly 400:1. The solution was gently shaken at room temperature for 2 h. After 2 h, a modified salt-aging procedure was used to ensure efficient and complete packing of the DNA onto the exposed surface[35]. An amount of 400 mM NaCl, 0.01% SDS, pH = 9 buffer was added to the

solution. Six additions were performed, each separated by 15 min, to raise the concentration of NaCl in solution to about 200 mM total. After the final addition, the solution was left to shake at room temperature overnight. To remove the excess DNA, the solution was centrifuged 5 times at 9,000 *g* for 10 min and washed with 0.01% SDS, pH = 9 buffer.

4.3.8 Self-assembly of the DNA-functionalized nanoparticles

UV-Vis was used to determine the relative concentrations of each NP-DNA solution. An equal molar amount of each solution was mixed in a centrifuge tube. An equal volume of 600 mM NaCl, 0.2× TAE buffer was added to the sample to give a final concentration of 300 mM NaCl, 0.1× TAE with a pH around 8. The sample was heated to 45 °C for min and then cooled by 1 °C min^{-1} until the temperature reached 15 °C to allow complete hybridization. pH switching was performed by adding 0.1 M amounts of HCl and NaOH to reach pH = 5 for the closed state and pH = 9 for the open state.

4.4 References

1. Alivisatos, A. P.; Johnsson, K. P.; Peng, X.; Wilson, T. E.; Loweth, C. J.; Bruchez Jr, M. P.; Schultz, P. G., Organization of'nanocrystal molecules' using DNA. *Nature* **1996,** *382* (6592), 609-611.

2. Mirkin, C. A.; Letsinger, R. L.; Mucic, R. C.; Storhoff, J. J., A DNA-based method for rationally assembling nanoparticles into macroscopic materials. *Nature* **1996,** *382* (6592), 607-609.

3. Jana, N. R.; Gearheart, L.; Murphy, C. J., Wet Chemical Synthesis of High Aspect Ratio Cylindrical Gold Nanorods. *The Journal of Physical Chemistry B* **2001,** *105* (19), 4065-4067.

4. Nikoobakht, B.; El-Sayed, M. A., Preparation and Growth Mechanism of Gold Nanorods (NRs) Using Seed-Mediated Growth Method. *Chemistry of Materials* **2003,** *15* (10), 1957-1962.

5. Sau, T. K.; Murphy, C. J., Room Temperature, High-Yield Synthesis of Multiple Shapes of Gold Nanoparticles in Aqueous Solution. *Journal of the American Chemical Society* **2004,** *126* (28), 8648-8649.

6. Liu, M.; Guyot-Sionnest, P., Mechanism of silver (I)-assisted growth of gold nanorods and bipyramids. *The Journal of Physical Chemistry B* **2005,** *109* (47), 22192-22200.

7. Scarabelli, L.; Coronado-Puchau, M.; Giner-Casares, J. J.; Langer, J.; Liz-Marzán, L. M., Monodisperse Gold Nanotriangles: Size Control, Large-Scale Self-Assembly, and Performance in Surface-Enhanced Raman Scattering. *ACS Nano* **2014,** *8* (6), 5833-5842.

8. Lee, J.-H.; Gibson, K. J.; Chen, G.; Weizmann, Y., Bipyramid-templated synthesis of monodisperse anisotropic gold nanocrystals. *Nature communications* **2015,** *6*.

9. Seeman, N. C., DNA in a material world. *Nature* **2003,** *421* (6921), 427-431.

10. Rothemund, P. W. K., Folding DNA to create nanoscale shapes and patterns. *Nature* **2006,** *440* (7082), 297-302.

11. Idili, A.; Vallée-Bélisle, A.; Ricci, F., Programmable pH-Triggered DNA Nanoswitches. *Journal of the American Chemical Society* **2014,** *136* (16), 5836-5839.

12. Liu, D.; Chen, G.; Akhter, U.; Cronin, T. M.; Weizmann, Y., Creating complex molecular topologies by configuring DNA four-way junctions. *Nat Chem* **2016,** *8* (10), 907-914.

13. Iacovelli, F.; Idili, A.; Benincasa, A.; Mariottini, D.; Ottaviani, A.; Falconi, M.; Ricci, F.; Desideri, A., Simulative and Experimental Characterization of a pH-Dependent Clamp-like DNA Triple-Helix Nanoswitch. *Journal of the American Chemical Society* **2017,** *139* (15), 5321-5329.

14. Li, Z.; Mirkin, C. A., G-quartet-induced nanoparticle assembly. *Journal of the American Chemical Society* **2005,** *127* (33), 11568-11569.

15. Auyeung, E.; Li, T. I.; Senesi, A. J.; Schmucker, A. L.; Pals, B. C.; de La Cruz, M. O.; Mirkin, C. A., DNA-mediated nanoparticle crystallization into Wulff polyhedra. *Nature* **2014,** *505* (7481), 73-77.

16. Chen, Y.; Mao, C., pH-Induced Reversible Expansion/Contraction of Gold Nanoparticle Aggregates. *Small* **2008,** *4* (12), 2191-2194.

17. Li, Y.; Liu, Z.; Yu, G.; Jiang, W.; Mao, C., Self-Assembly of Molecule-like Nanoparticle Clusters Directed by DNA Nanocages. *Journal of the American Chemical Society* **2015,** *137* (13), 4320-4323.

18. Shen, C.; Lan, X.; Lu, X.; Meyer, T. A.; Ni, W.; Ke, Y.; Wang, Q., Site-Specific Surface Functionalization of Gold Nanorods Using DNA Origami Clamps. *Journal of the American Chemical Society* **2016,** *138* (6), 1764-1767.

19. Pal, S.; Deng, Z.; Ding, B.; Yan, H.; Liu, Y., DNA-Origami-Directed Self-Assembly of Discrete Silver-Nanoparticle Architectures. *Angewandte Chemie International Edition* **2010,** *122* (15), 2760-2764.

20. Shimron, S.; Cecconello, A.; Lu, C.-H.; Willner, I., Metal nanoparticle-functionalized DNA tweezers: from mechanically programmed nanostructures to switchable fluorescence properties. *Nano letters* **2013,** *13* (8), 3791-3795.

21. Wang, Z.-G.; Elbaz, J.; Willner, I., DNA machines: bipedal walker and stepper. *Nano letters* **2010,** *11* (1), 304-309.

22. Seeman, N. C., DNA NANOTECHNOLOGY: Novel DNA Constructions. *Annual Review of Biophysics and Biomolecular Structure* **1998,** *27* (1), 225-248.

23. Seeman, N. C., Nanomaterials Based on DNA. *Annual review of biochemistry* **2010,** *79*, 65-87.

24. Seeman, N. C.; Chen, J.; Du, S. M.; Mueller, J. E.; Zhang, Y.; FU, T. J.; Wang, Y.; Wang, H.; Zhang, S., Synthetic DNA knots and catenanes. *ChemInform* **1994,** *25* (9).

25. Mao, C.; Sun, W.; Seeman, N. C., Assembly of Borromean rings from DNA. *Nature* **1997,** *386* (6621), 137-8.

26. Chichak, K. S.; Cantrill, S. J.; Pease, A. R.; Chiu, S.-H.; Cave, G. W.; Atwood, J. L.; Stoddart, J. F., Molecular borromean rings. *Science* **2004,** *304* (5675), 1308-1312.

27. Liu, D.; Chen, G.; Akhter, U.; Cronin, T. M.; Weizmann, Y., Creating complex molecular topologies by configuring DNA four-way junctions. *Nat Chem* **2016,** *8* (10), 907-14.

28. Bath, J.; Turberfield, A. J., DNA nanomachines. *Nature Nanotechnology* **2007,** *2*, 275.

29. Malachosky, E. W.; Guyot-Sionnest, P., Gold Bipyramid Nanoparticle Dimers. *The Journal of Physical Chemistry C* **2014,** *118* (12), 6405-6412.

30. Gole, A.; Murphy, C. J., Azide-derivatized gold nanorods: functional materials for "click" chemistry. *Langmuir* **2008,** *24* (1), 266-272.

31. Chen, T.; Wang, H.; Chen, G.; Wang, Y.; Feng, Y.; Teo, W. S.; Wu, T.; Chen, H., Hotspot-Induced Transformation of Surface-Enhanced Raman Scattering Fingerprints. *ACS Nano* **2010,** *4* (6), 3087-3094.

32. Chen, T.; Yang, M.; Wang, X.; Tan, L. H.; Chen, H., Controlled Assembly of Eccentrically Encapsulated Gold Nanoparticles. *Journal of the American Chemical Society* **2008,** *130* (36), 11858-11859.

33. Chen, G.; Gibson, K. J.; Liu, D.; Rees, H. C.; Lee, J. H.; Xia, W.; Lin, R.; Xin, H. L.; Gang, O.; Weizmann, Y., Site-specific surface encoding of nanoparticles for programmable self-assembly. *Under Revision - Nature Materials* **2018**.

34. Sönnichsen, C.; Reinhard, B. M.; Liphardt, J.; Alivisatos, A. P., A molecular ruler based on plasmon coupling of single gold and silver nanoparticles. *Nature biotechnology* **2005,** *23* (6), 741-745.

35. Hurst, S. J.; Lytton-Jean, A. K.; Mirkin, C. A., Maximizing DNA loading on a range of gold nanoparticle sizes. *Analytical chemistry* **2006,** *78* (24), 8313-8318.

36. Wang, W.; Liu, H.; Liu, D.; Xu, Y.; Yang; Zhou, D., Use of the Interparticle i-Motif for the Controlled Assembly of Gold Nanoparticles. *Langmuir* **2007,** *23* (24), 11956-11959.

Chapter 5 – Conclusions

In summary, we have developed solutions to provide improved performance of nucleic acid amplifications, and have demonstrated that the variety of properties exhibit by gold nanoparticles can be tuned and modulated to serve isothermal and thermocycling protocols. Additionally by relying on the plasmonic properties specifically, we were able to form discrete dimers and have them function as pH-responsive nanomachines through the use of the dsDNA to triplexDNA interconversion. The use of metallic nanoparticles offers creative solutions by exploiting their properties which are orthogonal to those typically found in the biological materials. We have specifically used high surface-to-volume charge density, plasmonics, or their photothermal behavior of various gold nanoparticles but there is a wide array of shapes and materials that can still be explored.

5.1 Future of nucleic acid amplifications

Nucleic acid amplifications have become so commonplace in the research landscape that they are now even commercially available for at-home analysis of dog breeds[1]. It is easy to get lost in the glamour of "DNA testing" presented in movies and television, but the significance and power of these assays should not be overlooked. Focusing attention back to PCR, since it is the most commonly used nucleic acid amplification, there are a few points I would like to address. The commercial biotechnology area has saturated the market with enzymes that have been strategically evolved to provide polymerization rates several orders of magnitude faster than their wild type counterparts. However, there has been a plateau of this development, and therefore, with the achievement of rapid heating and cooling, such as the method presented above, it appears we are approaching the lower limit of assay duration. Therefore, further experimentation down this research path would almost certainly fall victim to the law of diminishing return. This

should be looked at as a new opportunity to expand our thinking beyond marginal optimizations and create solutions to better address the other technical limitations associated with bioanalytical techniques. Particularly, there are issues with sample preparation, reagent stability, and the general costs both financial and energetic for reagents and devices. This might no longer be a problem for chemists and biologists to solve in the lab, but one that might require additional input from end-point users and engineers.

The isothermal nucleic acid amplification field is a large example of the alternative type of exploration, in that these methods involve strategies distinct from PCR to achieve their amplification. As mentioned above, they have niche uses now, but creative solutions are constantly being reported, such as the new "SHERLOCK" method which involves CRISPR, a recombinase, and polymerase to provide sensitive hand-warmed amplifications[2]. It is this type of interplay that should be explore further. Mixing elements of materials, biology, and chemistry together will yield much more promising results in the future.

5.2 Future projects

This is the final section of my thesis and thus I would like to it to serve as a brief perspective to some of the future points I think would be worth exploring. The fields of nucleic acid amplification and nanomaterials are practically limitless in their potential applications, therefore I will focus this presentation to some future aspects which I believe to be logical extensions from the research provided in the previous chapters. Hopefully these ideas will inspire future students to continue this research trajectory.

5.2.1 PPT methods for other biological assays

The photothermal plasmonic particles provide an interesting material to use for other applications which have been plagued by issues similar to those found in the nucleic acid amplifications such as long assay duration and expensive instrumentation. Additionally there are many biological and medical targets that are not nucleic acids, such as proteins, drugs, chemical compounds, and the strict design of traditional PCR makes these more difficult to analyze. By applying this strategy and these particles to other biologically relevant assays, similarly impressive results might be achievable. In particular, the enzyme-linked immunosorbent assay (ELSIA) has had variable success at detecting low-abundance antigens and does not yet reach the sensitivity traditionally associated with PCR[3].The antibody recognition system employed by the ELISA has already been accommodated to NAAs via the immunoPCR system[4-5].

The power of the immunoPCR (iPCR) technique is it combines the diversity of detection to multiple kinds of molecules while retaining the excellent sensitivity and associated with PCR. By replacing the antibody-enzyme complex used in ELISA, for example, with an antibody-DNA conjugate, a resulting quantification can typically lead to 10- to 1000-fold increases in the limit of detection[4]. By exploiting the capabilities of iPCR and combining them with our photothermal system we can create the PPT-qiPCR. The photothermal particles will be able to provide the appropriate thermocycling and that the various reagents will remain active to attain exquisite sensitivity for the detection, using DNA-antibody conjugates to act as the nucleic acid templates for real-time PCR with our photothermal system. Furthermore, by tethering the DNA template directly to the detection antibody, we can shorten sample preparation time and drastically reduce the risk of carry-over contaminations. DNA can be synthesized with various functional groups at the 5’ or 3’ end include azides, amines, and thiols, among many others. These can be bio-conjugated to the antibody, eliminating several molecular recognition steps. This will not only

succeed at the rapid and real-time detection through protein-antibody recognition, but also lay a foundation for the assessment of biomedical samples relating to any diseases which are identifiable by non-nucleic biomarkers. All these achievements should be a stimulus to continue the research on photothermal effect and its application in life sciences and technology.

5.2.2. Expansion of the plasmonic actuator

The success of the plasmonic actuator should lay the foundation for the expansion of the discrete assembly protocol to include other arrangements and other nanoparticles such has gold-bipyramids, quantum dots, or fluorescent tags. This system will allow for further studies of nanoparticle interactions with other nanoparticles, quantum dots or fluorescent dyes. Because the ability to construct large quantities of nanoparticle dimers in high purity and high yield has remained elusive, there have been limited studies into the interactions of individual nanoparticles. It would be worthwhile to provide a means to discretely investigate the phenomena associated with nanoparticles, such as plasmonic coupling and electromagnetic field enhancement, by exploiting the simplicity and adaptability of our self-assembly method. As described above, the labeling of the particles is completely modular, as it relates to the sequence of the synthetic DNA. Therefore more intricate designs can be designed including other functional sequences such as aptamers or topologically significant or chiral structures[6-7]. Additionally, the diversity of structures is not restricted to DNA, and could be expanded to include the wide array of structural motifs found in RNA.

Pushing this farther and applying these systems to probe biological environments is also a promising research direction. It has been well-studied that noble metal nanoparticles can enter into cells through a variety of mechanisms, and that the size of the nanoparticles or structures greatly influences whether uptake occurs and in what manner[8-9]. These nanomechanical systems

lie within the same size-realm as others reported, giving credence to the belief that they will enter the cell. Once inside the cell, optical microscopy can be used to study the trafficking of discrete nanomachines, while the unique absorbance peaks of the nanomachines will provide real-time information of the pH. For example, we can track the evolution of vesicle pH, like the ones often used in uptake mechanisms, as it changes spatiotemporally[10]. In addition, it has now been well-studied that the pH within cancer cells is lower than in healthy cells, likely to due to the higher metabolic rate of cancer cells[11]. Therefore, our nanomachines could differentiate between healthy and cancer cells by just measuring the absorbance peak location, a common feature on these microscopes. Therefore, it will allow us to do rapid screening of cells to determine whether cancer cells are present as well as other real-time trafficking studies. In addition, the trafficking mechanism within the cell could likely change based on the size and shape of the nanoparticle structures, also providing previously unobtainable information. It is clear that nanotechnology and nanoparticles will allow us to solve many important problems from different disciplines of science. I humbly hope that this thesis will serve to inspire others to follow this exciting research.

5.3 References

1. Parker, H. G.; Kim, L. V.; Sutter, N. B.; Carlson, S.; Lorentzen, T. D.; Malek, T. B.; Johnson, G. S.; DeFrance, H. B.; Ostrander, E. A.; Kruglyak, L., Genetic Structure of the Purebred Domestic Dog. *Science* **2004,** *304*, 1160-1164.

2. Gootenberg, J. S.; Abudayyeh, O. O.; Lee, J. W.; Essletzbichler, P.; Dy, A. J.; Joung, J.; Verdine, V.; Donghia, N.; Daringer, N. M.; Freije, C. A.; Myhrvold, C.; Bhattacharyya, R. P.; Livny, J.; Regev, A.; Koonin, E. V.; Hung, D. T.; Sabeti, P. C.; Collins, J. J.; Zhang, F., Nucleic acid detection with CRISPR-Cas13a/C2c2. *Science* **2017**.

3. Zhang, S.; Garcia-D'Angeli, A.; Brennan, J. P.; Huo, Q., Predicting detection limits of enzyme-linked immunosorbent assay (ELISA) and bioanalytical techniques in general. *Analyst* **2014,** *139* (2), 439-445.

4. Niemeyer, C. M.; Adler, M.; Wacker, R., Immuno-PCR: high sensitivity detection of proteins by nucleic acid amplification. *Trends in Biotechnology* **2005,** *23* (4), 208-216.

5. Sano, T.; Smith, C. L.; Cantor, C. R., Immuno-Pcr - Very Sensitive Antigen-Detection by Means of Specific Antibody-DNA Conjugates. *Science* **1992,** *258* (5079), 120-122.

6. Seeman, N. C., Nanomaterials Based on DNA. *Annual review of biochemistry* **2010,** *79*, 65-87.

7. Liu, D.; Chen, G.; Akhter, U.; Cronin, T. M.; Weizmann, Y., Creating complex molecular topologies by configuring DNA four-way junctions. *Nat Chem* **2016,** *8* (10), 907-14.

8. Dreaden, E. C.; Alkilany, A. M.; Huang, X.; Murphy, C. J.; El-Sayed, M. A., The golden age: gold nanoparticles for biomedicine. *Chemical Society Reviews* **2012,** *41* (7), 2740-2779.

9. Huang, K.; Ma, H.; Liu, J.; Huo, S.; Kumar, A.; Wei, T.; Zhang, X.; Jin, S.; Gan, Y.; Wang, P. C., Size-dependent localization and penetration of ultrasmall gold nanoparticles in cancer cells, multicellular spheroids, and tumors in vivo. *ACS nano* **2012,** *6* (5), 4483-4493.

10. Huotari, J.; Helenius, A., Endosome maturation. *The EMBO Journal* **2011,** *30* (17), 3481-3500.

11. Tannock, I. F.; Rotin, D., Acid pH in tumors and its potential for therapeutic exploitation. *Cancer research* **1989,** *49* (16), 4373-4384.